Shedding Light on Post-Copulatory Sexual Selection

Tania Mendonca

A thesis submitted in partial fulfilment of the requirements for the degree of Doctor of Philosophy

The University Of Sheffield.

Faculty of Science
Department of Animal and Plant Sciences

January 2018

Contents

Abstract

Fertilisation requires one sperm. The selection of the 'winning' sperm out of the millions inseminated into the female is not determined by a simple lottery, but rather a complex set of interactions between sperm and the female reproductive tract. These post-mating interactions, collectively termed post-copulatory sexual selection (PCSS), are influenced by many factors from biochemical to behavioural, making PCSS dynamic, complicated, and challenging to study.

In some taxa, including birds, sperm take a surprising diversion in their long journey between copulation and conception. Females of many species can store sperm for extended periods of time in specialised storage sites within their reproductive tracts. Such storage can give females the opportunity to bias fertility outcomes through PCSS mechanisms. However, these processes occur deep within the female body, making them particularly difficult to document.

A critical step towards understanding these mechanisms involves visualising them in real time, inside female tissue, under physiological conditions that are as close to natural as possible. Such visualisation is not trivial – especially in birds – due to the challenges of imaging through thick, muscular tissue.

In this thesis, I demonstrate the optimisation of selective plane illumination microscopy (SPIM) and the development of imaging protocols, including sample preparation and cell labelling for this novel application. SPIM is a light sheet fluorescence microscopy technique,

which allowed me to optical section live oviduct tissue to reveal the three-dimensional structure of sperm storage tubules (SSTs) in zebra finch [*Taeniopygia guttata*] females. This imaging technique, in combination with electron microscopy, also allowed me to make volumetric observations of zebra finch sperm mid-piece structure. These studies have helped us understand the adaptive significance of these structures, as well as the functioning of SSTs and the possible sperm-female interactions that occur inside them.

Acknowledgements

The research presented in this thesis was part of a multi-disciplinary bio-imaging initiative 'Imagine: Imaging Life', and my studentship was funded by 2022 Futures at the University of Sheffield.

I owe my deepest gratitude to my primary supervisor, Dr. Nicola Hemmings, for the tremendous support and guidance throughout my PhD. Our meetings have always been stimulating and have invariably left me feeling uplifted and excited about my research. I am also thankful to my secondary supervisor, Dr. Ashley Cadby, for giving me the opportunity to build my own microscope. Ashley has taught me a great deal about optics, programming and having faith in my own abilities. Thanks also to Prof. Simon Jones for his supervision and support.

I am grateful to Prof. Tim Birkhead for always making himself and his wealth of knowledge available to me, and for treating me as one of his own students. The continued encouragement, and rigorous and detailed feedback, from both Tim and Nicola, has helped me enormously towards improving my writing and presentation skills.

Dr. Wolfgang Forstmeier and Prof. Bart Kempenraers at the Max Planck Institute for Ornithology in Seewiesen hosted me and made their study populations available for this research. Their help was instrumental in the success of one of the studies detailed in this thesis. I must also thank Dr. Andrew Narracott for his guidance on the image analysis.

This work was made possible because of the dedicated service of staff at the Animal House, especially Phil and Lynsey, and Paul and Jonathan at the Physics workshop. Irene and Andy at APS have been wonderfully helpful and always made the time to help me find spare instruments and/or consumables.

A massive thanks to Jamie and Emily from the Birkhead lab, and the wonderful undergraduate student volunteers over the years: Jack, Eve and Gerrard for being so willing and enthusiastic to help when needed. Much of the work in this thesis would not have been possible without the extra sets of hands.

The last four years have been thoroughly enjoyable thanks to the wonderful friendship of the members (past and present) of the Birkhead lab and the Cadby lab. I am grateful to Tim's post-docs over the years, Alex and Clair, for all the stimulating discussions, guidance on the little details of research life, and statistics advice. A special thank you to Amy from the Cadby lab for making all those long days in the dark, overheated microscopy lab a fun experience!

I am indebted to my parents for always encouraging me to pursue my interests. Finally, I must thank my partner Will for being my sounding board and support through all the highs and lows of pursuing a doctorate.

Abbreviations

2D	Two-dimensional
3D	Three-dimensional
ALH	Lateral head amplitude
ATP	Adenosine triphosphate
BCF	Beat cross frequency
BP	Band pass
CatSpers	Cation channels of sperm
CFC	Cryptic female choice
CI	Confidence interval
CLSM	Confocal laser scanning microscopy
CV	Coefficient of variation
Di10	4-Di-10-ASP
DiA	4-Di-16-ASP
DIC	Differential interference contrast
diSPIM	Dual-view inverted selective plane illumination
DMEM/F12	Dulbecco's Modified Eagle Medium: Nutrient Mixture F-12
DNA	Deoxyribonucleic acid
DPSSL	Diode-pumped solid-state laser
DSLM	Digitally scanned light sheet microscopy
EM	Electron microscopy
Fiji	Fiji is just ImageJ
FOV	Field of view
FP	Fluorescent protein
FWHM	Full width at half maximum
GFP	Green fluorescent protein
GLMM	Generalised linear mixed model
LP	Long pass
LS-RESOLFT	Light sheet reversible saturable/switchable optical linear (fluorescence) transitions
LSFM	Light sheet fluorescence microscopy
MIP	Maximum intensity projection
NA	Numerical aperture
ND filter	Neutral density filter
OSM	Optical sectioning microscopy
OXPHOS	Oxidative phosphorylation

PBS	Phosphate buffered saline
PC1	Principal component 1
PCA	Principal component analysis
PCIe	Peripheral component interconnect express
PCSS	Post-copulatory sexual selection
PSF	Point spread function
R18	Octadecyl Rhodamine Chloride B
RFP	Red fluorescent protein
RI	Refractive index
RNA	Ribonucleic acid
ROI	Region of interest
rpm	Revolutions per minute
SCA	Sperm Class Analyzer
sCMOS	Scientific complementary metal-oxide-semiconductor
SD	Standard deviation
SEM	Scanning electron microscopy
SG	Seminal glomeruli [plural; glomerus - singular]
SHL	Straight helix length
SIM	Structured illumination microscopy
SNR	Signal to noise ratio
SPIM	Selective plane illumination microscopy
SR-SIM	Super-resolution structured illumination microscopy
SST	Sperm storage tubule
STED	Stimulated emission depletion microscopy
STORM	Stochastic optical reconstruction microscopy
TEM	Transmission electron microscopy
TTL	Transistor-transistor logic
UVJ	Utero-vaginal junction
VAP	Average path velocity
VCL	Curvilinear velocity
VI	LabView virtual instrument
VSL	Straight line velocity
WD	Working distance

Units

X	times
cm	centimetres
mm	millimetres
μm	micrometres
nm	nanometres
°	degrees
°C	degrees Celsius
hrs	hours
mins	minutes
s	seconds
ms	milliseconds
mL	millilitres
μL	microlitres
mM	millimolar
μM	micromolar
pH	Hydrogen ion concentration
λ_{ex}	Excitation wavelength
λ_{em}	Emission wavelength
pxls	pixels
a.u.	Airy units
J	Joules
mW	milliwatts
keV	kilo electron volt

Chapter 1.

Post-copulatory sexual selection through a microscope lens

1.1. Introduction

Post-copulatory sexual selection (PCSS)

Charles Darwin (1871) defined sexual selection as the selection of heritable traits that confer a reproductive advantage to sexually reproducing individuals. Darwin's theory, however, focussed on pre-mating events – competition between (usually) males of the same species for access to mates, termed 'intrasexual selection', and the choosing of mates by (usually) females, termed 'intersexual selection'. About a century later, evidence began to accumulate that promiscuity among females across taxa was far more prevalent than previously thought [e.g. birds (Birkhead and Møller, 1995), mammals (Hanken and Sherman, 1981; Tegelström *et al.*, 1991; Amos *et al.*, 1993), reptiles (Uller and Olsson, 2008), fishes (Avise *et al.*, 2002) and insects (Gromko *et al.*, 1984; Moritz *et al.*, 1995; Crozier and Fjerdingstad, 2001)], creating the conditions for these sexual selection events to continue after copulation, as (1) competition between sperm from different males for the fertilisation of ova (sperm competition; Parker, 1970, 1984, 1998), and (2) non-random

biasing of paternity by female processes (cryptic female choice; Thornhill, 1983; Eberhard, 1996; Pitnick and Brown, 2000).

Both these modes of post-copulatory sexual selection encompass behavioural processes during and shortly after copulation, and physiological processes in the period after copulation up until fertilisation. To influence the outcome of post-copulatory sexual selection males can increase the frequency of copulations (Crowe *et al.*, 2009), and/or volume (Parker, 1998; Hosken *et al.*, 2001) or quality of ejaculates [e.g. improved morphology or swimming velocity] (Snook, 2005); use specially adapted genitalia to physically displace sperm from competing males within the female's reproductive tract during copulation (Waage, 1979); and/or plug the female's reproductive tract or guard females post mating (Barker, 1994). Females may influence paternity by controlling the timing and order of copulation with competing males (Xu and Wang, 2010; Firman *et al.*, 2017) as well as differentially ejecting sperm from her reproductive tract (Pizzari and Birkhead, 2000).

Post mating physiological events involve sperm-sperm interactions wherein sperm from a male can physically displace or influence the motility of sperm from competing males, and/or position themselves strategically in the female reproductive tract to gain a competitive advantage (Birkhead and Møller, 1998; Snook, 2005; Fitzpatrick and Lüpold, 2014). The female reproductive tract (in internal fertilisers) and oviductal (in internal fertilisers) or ovarian fluid (in external fertilisers) can interact with sperm to mediate fertilisation outcomes through processes such as differential sperm storage (Hellriegel and Bernasconi, 2000; Hemmings and Birkhead, 2017), the influencing of sperm swimming velocity (Urbach *et al.*, 2005; Rosengrave *et al.*, 2008, 2016) and/or the initiation of immune responses towards incompatible sperm (Ziegler *et al.*, 2005; Løvlie *et al.*, 2013). While some behavioural aspects of female choice are easily detectable, the physiological aspects of both

sperm competition and cryptic female choice are likely to interact and influence each other, and these interactions are hidden inside the reproductive tract of internal fertilisers. This makes it technically difficult to study the independent effects of sperm competition and cryptic female choice on fertility success and the evolution of reproductive traits in isolation (Birkhead, 1998; Eberhard, 2000). Much of what we do know about post-copulatory sexual selection has come from the study of the widespread diversity in the form and function of sperm (Pitnick *et al.*, 2009a; Fitzpatrick and Lüpold, 2014; Rowe *et al.*, 2015), and male (Hosken and Stockley, 2004; Ramm *et al.*, 2005) and female (Pitnick *et al.*, 1999, 2009b; Hosken and Stockley, 2004) genitalia. From the beginning, developments in microscopy and imaging technology have been key to facilitating this work.

Snapshots of dynamic phenomena

The origins of our understanding of fertilisation itself are closely linked with the development of microscopy. Antoni van Leeuwenhoek, a pioneer of optical microscopy, made the first detailed observations on sperm and linked them to fertility (Leeuwenhoek, 1678, 1989). As microscope technology progressed, so did our understanding of sperm form and function [see (Birkhead and Montgomerie, 2009) for a historical timeline].

The first modern microscopes were optical microscopes – using wavelengths of light from the visible spectrum to produce magnified images of specimens. Leeuwenhoek's own microscopes were single lens optical microscopes (Zuylen, 1981). Although optical microscopes aided the study of sperm structural components and morphological diversity, these microscopes were limited in their resolving power (see Box 1). It was only after the advent of electron microscopy that the fine structure and internal organisation of sperm became known, thanks to pioneers

such as Björn Afzelius – who discovered the dynein arms in sea urchin sperm flagella (Afzelius, 1959). The recent development of super-resolution optical fluorescence microscopy – optical microscopy techniques that image beyond the resolution limit – has enabled the localisation of sperm proteins [e.g. CatSpers using STORM (Chung *et al.*, 2014), acrosome membrane proteins CD46 and β1 integrin using STED and SIM (Frolikova *et al.*, 2016)].

Box 1

The resolution limit of an instrument is the minimum resolvable distance between two discrete points (Hecht, 2002). This can be described by the Rayleigh criterion,

$$\delta = \frac{0.61\lambda_{ex}}{\mathrm{NA}} \quad (1)$$

where δ is the resolution limit, λ_{ex} represents the wavelength of illumination used and NA is the numerical aperture of the objective lens.

For an ideal optical microscope using a high NA objective and short wavelength (blue) illumination, the resolution limit is ~200 nm. This is sensitive enough to be able to image gross structural features of sperm and female storage organs in most taxa (see Figure 1 for an example with the zebra finch model). However, this is not sufficient for detecting certain sub-cellular features – e.g. the 24 nm periodicity of dynein arms in the starling [*Sturnus vulgaris*] flagellum (Vernon and Woolley, 1999).

The wavelength of an electron at 100 keV is calculated to be 0.004 nm (Williams and Carter, 1996) which is much smaller than the wavelengths in the visible range [390 nm – 700 nm], allowing electron microscopes to work at much higher resolutions than possible with optical microscopes.

Super-resolution optical microscopy techniques can achieve resolutions beyond the resolution limit by exploiting the non-linear response of fluorescent molecules (fluorophores) [e.g. STED (Hell and Wichmann, 1994)] or stimulating such a response to excitation [e.g. STORM (Rust *et al.*, 2006)], or by using structured illumination [e.g. SIM (Gustafsson, 2000)].

Female components involved in post-copulatory processes include the reproductive tract itself, ova, oviductal fluid, and biomolecules such as ions and hormones. These components lie on, and function within, a very wide spatial scale [see Figure 1 for an example from zebra finches].

Studies into the female reproductive anatomy have largely employed histology and wide-field optical imaging techniques. Histological studies of the female reproductive tract helped reveal the existence of sperm storage organs [e.g. birds (Van Drimmelen, 1946; Bobr *et al.*, 1964; Bakst and Bird, 1987; Birkhead, 1987), snakes (Fox, 1956), insects (Siva-Jothy, 1987)]. These storage organs are a potential site for mechanisms of cryptic female choice (i.e. 'sperm selection') to take place, given that sperm can stay in intimate contact with female tissue in these storage sites for prolonged periods – from a few days to months, depending on species (Birkhead and Møller, 1993). Evidence from studies that have extracted sperm from storage organs and imaged them, suggests that acceptance into storage can be selective (e.g. based on sperm morphology: Hellriegel and Bernasconi, 2000; Hemmings and Birkhead, 2017). Once inside the storage organs, transmission electron microscopy (TEM) images have shown that sperm can be embedded in the storage organ epithelium (Daly and Golding, 1977; Racey, 1979; Giusti and Selmi, 1985; Longo *et al.*, 1998), or in close contact with cilia/microvilli (Bakst and Bauchan, 2015; Chen *et al.*, 2015) in some species.

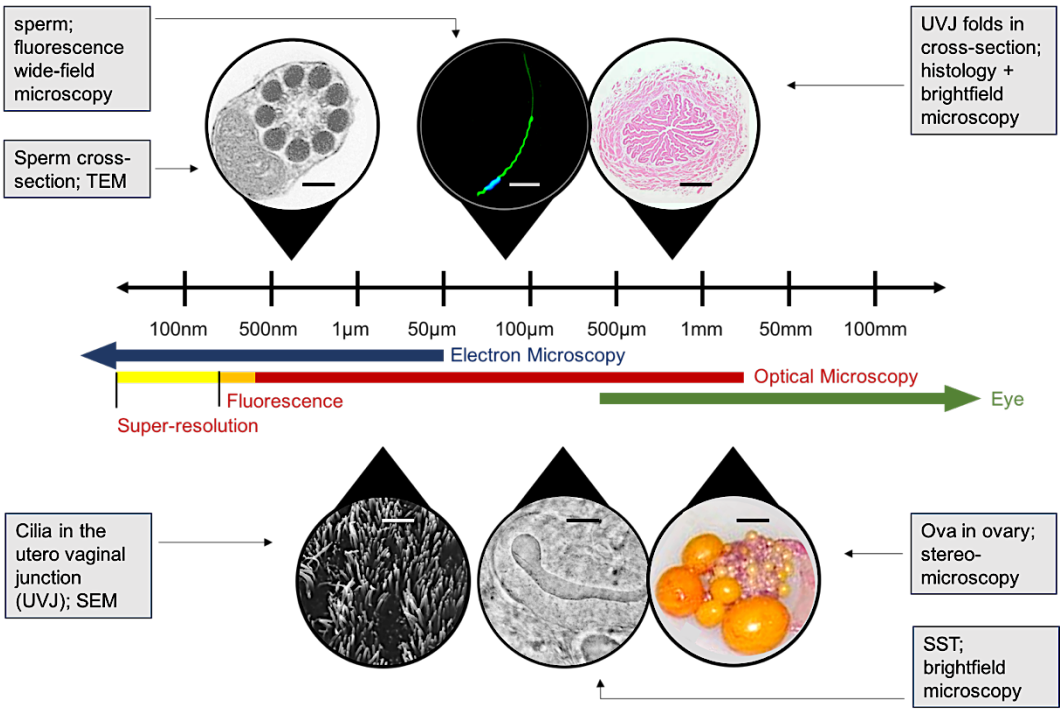

Figure 1: Post-copulatory sexual selection involves physiological structures and processes that occur over a wide spatial range. Images and values are for the zebra finch model: sperm - 0.6 μm across [TEM; scale bar – 100 nm] and 70 μm long [fluorescence; scale bar – 10 μm]; cilia in the utero vaginal junction (UVJ) [SEM; scale bar – 5 μm] - 1-10 μm long; SSTs - 100-200 μm long [bright field; scale bar – 20 μm]; UVJ folds <1mm across but just about visible with the naked eye [histology; scale bar – 2 mm]; mature ova - 10-15 mm long [stereomicroscopy; scale bar – 5 mm] and can easily be seen with the naked eye.

The structure of female sperm storage organs is often complex and in some species, there are multiple different types of storage organ within a female [e.g. insects (Pitnick *et al.*, 1999; Nakahara and Tsubaki, 2007)]. Much of what we know about these structures comes from histology and squash preparations of thin sections of tissue. Electron microscopy techniques such as scanning electron microscopy (SEM) and transmission electron microscopy (TEM) have revealed the ultrastructure of these organs (Burke *et al.*, 1972; Schuppin *et al.*, 1984; Chiba and Nakamura, 2001; Fritz and Turner, 2002). These imaging approaches present two-dimensional views of what are essentially complex, three-dimensional structures. Very little is known about the

three-dimensional shape or functional changes in these structures. Mattei *et al.* (2015) were able to show that seminal proteins can bring about contractions and other movements of the female tract to aid sperm storage and transport. They achieved this using three dimensional micro-CT imaging of Drosophila [*Drosophila melanogaster*] females flash frozen and fixed at varying stages after copulation. Each female provided an individual snapshot, and combining these data revealed temporal changes in the reproductive tract. Micro-CT uses X-ray excitation, which can image through large, thick tissue. However, this method required females to be fixed and dehydrated before imaging, precluding the study of functional changes and sperm-female interactions in real time (Mattei *et al.*, 2015).

Fluorescence microscopy

Visualising functional changes in female tissue and sperm behaviour in real time, inside the female reproductive tract, is essential for understanding the mechanisms of post-copulatory sexual selection. Live imaging of sperm in female tracts has been achieved using fluorescence microscopy techniques in Drosophila (Manier *et al.*, 2010; Köttgen *et al.*, 2011), flatworms (Marie-Orleach *et al.*, 2014, 2016), as well as in some vertebrates; sheep (Druart *et al.*, 2009) and mice (Chang and Suarez, 2012). Fluorescence microscopy allows for the selective labelling of cell components or biomolecules of interest, making it possible to study cell behaviour – e.g. sperm swimming backwards in the seminal receptacle in Drosophila (Köttgen *et al.*, 2011). In all previous studies [except (Druart *et al.*, 2009)], imaging has been possible only in relatively transparent sections of the oviducts. In ewes fluorescence endoscopy was employed to image sperm movement in the oviduct *ex vivo* (Druart *et al.*, 2009).

Live imaging of sperm in the female reproductive tract has not yet been possible in birds. The avian oviduct presents a greater challenge for imaging since producing calcified, cleidoic eggs necessitates a particularly long and muscular tract (Bakst *et al.*, 1994). The opaque, muscular tissue of the avian oviduct generates noise by refraction, reflection and diffraction of light during imaging (Conchello and Lichtman, 2005). This noise or 'scatter', obscures fluorescence signal from target tissue/cells/substances. The deeper the imaging plane within a specimen, the larger the distance for light to travel through, and therefore the more scatter generated. Increased scatter with deeper imaging planes also reduces the intensity of the signal received. Additionally, when a whole specimen is illuminated, a conventional wide-field microscope will detect fluorescence outside the focal plane as out-of-focus fluorescence noise in addition to the signal from the focal plane. To counter these challenges, oviduct tissue has typically been physically trimmed and sectioned before imaging.

Box 2

Fluorescence

When a fluorescent molecule (fluorophore) receives a photon of light it can get elevated to a higher electronic state (Figure 2, S_1) from the ground state (Figure 2, S_0). The fluorophore then relaxes to the lowest vibrational level of S_1 – internal conversion, before emitting energy in the form of fluorescence to return to the ground state (Lakowicz, 2006a).

A fluorophore in the S_1 state may sometimes undergo a spin conversion to enter the triplet state (Figure 2, T_1) through intersystem crossing. From T_1 it can return to the ground state through non-radiative relaxation or 'phosphorescence'. Occasionally, a fluorophore may interact with another molecule while it is in the triplet state leading to irreversible loss of fluorescence called photobleaching (Lakowicz, 2006a). Fluorophores

in the excited states can also interact with molecular oxygen to release free radicals which can damage live cells resulting in phototoxicity (Dixit and Cyr, 2003).

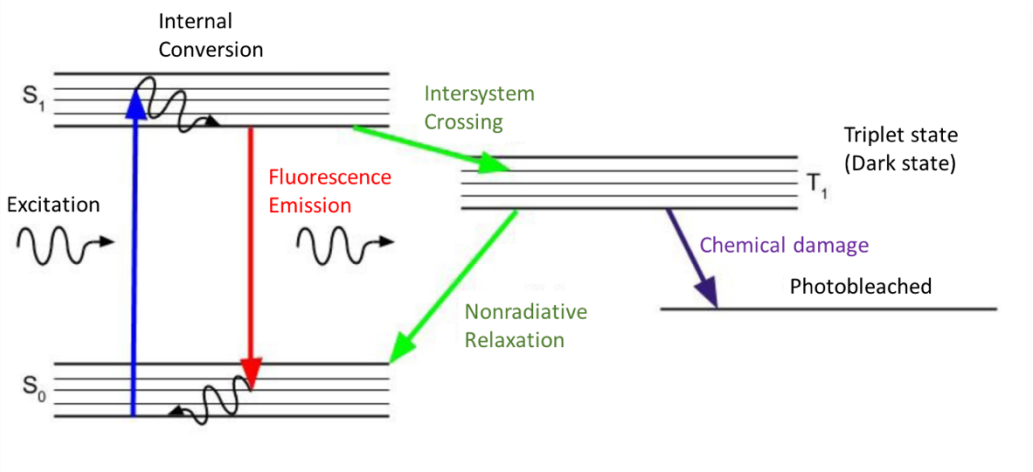

Figure 2: Jablonski diagram illustrating fluorescence. Electronic states: S_0 – ground, S_1 – excited, T_1 – triplet. The lines within each electronic state represent the vibrational energy levels.

Optical sectioning

Optical sectioning provides a powerful alternative to physical serial sectioning, allowing noise from thick specimens to be circumvented while leaving the specimen whole. This makes it an attractive technique for tracking functional changes in female tissue and sperm-female interactions in real time and in three dimensions. To achieve this, images are acquired at multiple focal planes through the thick specimen [e.g. oviduct]. In each imaging plane the contribution of out-of-focus and scattered light is removed to provide high contrast information – thin optical sections. These optical sections can be computationally stitched together to obtain the three-dimensional reconstructions of the original specimen (Agard, 1984).

Some commonly used optical sectioning techniques include optical sectioning microscopy (OSM – bright field, phase contrast or

fluorescence), differential interference contrast (DIC), confocal laser scanning microscopy (CLSM), structured illumination microscopy (SIM), multiphoton microscopy and light sheet fluorescence microscopy (LSFM) (Agard, 1984; Gustafsson, 2000; Huisken *et al.*, 2004; Larson, 2010). Bakst (1994) and King *et al.* (2002) successfully imaged fluorescently tagged domestic fowl [*Gallus domesticus*] and turkey [*Meleagris gallopavo*] sperm inside female sperm storage tubules (SSTs) in unfixed, thin sections using DIC microscopy. Of the different optical sectioning techniques, CLSM (Agard, 1984), multiphoton (Larson, 2010) and LSFM (Huisken *et al.*, 2004) are capable of imaging through thicker tissue sections than the other techniques. CLSM has been used to detect the presence of nerve endings and cytoskeletal elements (Freedman *et al.*, 2001), and for the localisation of lectins (Bakst and Bauchan, 2016), in SSTs in fixed UVJ tissue from turkeys and chicken respectively.

Live specimens have an added requirement - imaging must not impair tissue/cellular viability or function. High signal to noise ratios can be achieved by increasing the number of fluorophores or intensity of laser excitation, but this increases the phototoxicity experienced by the specimen (see Box 2). Laissue *et al.* (2017) have shown that exposure to even small amounts of blue light (18.5 – 23.1 J/cm2) for 4-5 mins was enough to significantly impede cell proliferation. LSFM is capable of imaging with high signal to noise ratios at high speeds through thick tissue with lower photobleaching and phototoxicity than CLSM, and multiphoton microscopy and has therefore been christened the 'smart and gentle microscope' (Scherf and Huisken, 2015). Additionally, LSFM microscopes typically use large sample chambers instead of microscope stage platforms (Greger *et al.*, 2007), which allows larger samples to remain intact and un-deformed, with space for experimental manipulation during imaging. In this thesis, I describe the adaptation of a variant of LSFM – selective plane illumination microscopy (SPIM) – for imaging avian sperm and sperm storage structures in oviductal tissue,

and its use for studying post-copulatory sexual selection in zebra finches (*Taeniopygia guttata*).

1.2. Thesis outline

The objective of this thesis has been to adapt and utilise a relatively new imaging technology – selective plane illumination microscopy (SPIM) – for imaging sperm and SSTs in order to answer key questions about sperm storage and post-copulatory sperm-female interactions.

Chapter 2 describes the self-built SPIM microscope used for this work, including its components, characterisation, programming and general function. As in this introductory chapter, microscopy theory is introduced in boxes interspersed through Chapter 2. In Chapter 3, I assess the performance of a range of organic fluorophores for studying zebra finch sperm form and function. Fluorophores can introduce confounding effects to cell behaviour experiments so the effect of these fluorophores on sperm structure, swimming velocity and on sperm-female interactions was tested. Chapter 4 describes the three-dimensional structure and organisation of the zebra finch sperm mid-piece. This study used SPIM in combination with TEM microscopy to explore how mid-piece length relates to mitochondrial volume, internal organisation and energetics. Chapter 5 describes the use of SPIM to understand sperm storage mechanisms by analysing the three-dimensional structure of SSTs and drawing conclusions about their functional behaviour. Chapters 4 and 5 both include substantial methods development which has been included as a sub-section at the beginning of the methods in each chapter. Finally, in Chapter 6, I summarise my findings and highlight future research directions.

Chapter 2.

SPIM Design and Assembly

2.1. Introduction

Linking sperm form to their function inside the three-dimensional environment of the female tract is an important step forward for understanding post-copulatory sexual selection. However, due to limitations with imaging technologies, previous studies have mostly studied sperm and the female reproductive tract using standard light microscopy techniques and histological sectioning, providing information in two dimensions only [sperm (Immler and Birkhead, 2007; Fitzpatrick and Baer, 2011; Tourmente *et al.*, 2011; Bennison *et al.*, 2015); female sperm storage sites (Shugart, 1988; Birkhead and Møller, 1992; Pitnick *et al.*, 1999)]. Physical sectioning also removes the opportunity to visualise physiological processes in real-time. Recent developments in imaging technology such as selective plane illumination microscopy (SPIM) provide a powerful alternative – the ability for live imaging of large tissues samples (Sena *et al.*, 2011; Ahrens *et al.*, 2013; Pampaloni *et al.*, 2013) and whole organisms (Keller and Stelzer, 2008; Ichikawa *et al.*, 2013; Schmid *et al.*, 2013) at sub-cellular resolution using optical sectioning.

SPIM uses a thin sheet-like projection of light to optically section fluorescently labelled samples. This light sheet illumination results in excitation of fluorescently labelled molecules (fluorophores) present in the thin section illuminated by the light sheet. The fluorescence emitted by these fluorophores is collected by a separate objective lens (Figure 1)

placed orthogonally to the illumination objective lens. The focal planes of the two objective lenses (illumination and detection) are made to intersect, resulting in the optical sectioning of the sample at the intersection of these focal planes. This orthogonal arrangement of objective lenses is a hallmark of this microscopy technique. Serial sectioning can be achieved either by moving the sample through the light sheet (Huisken *et al.*, 2004; Pitrone *et al.*, 2013), or moving the light sheet itself across a stationary sample [e.g. diSPIM (Wu *et al.*, 2013)]. The non-destructive nature of this microscopy technique eliminates the risk of loss of material or sample deformation between the serial sections, as is often the case in physical sectioning techniques such as histology.

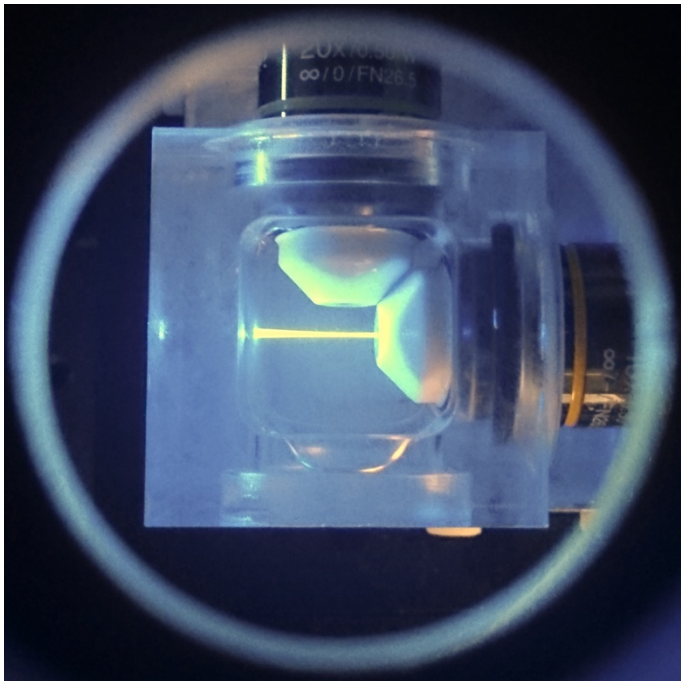

Figure 1: The light sheet is projected by an illumination objective and fluorescence emission is collected by a separate detection objective. Both objective lenses dip into a large sample chamber.

The uncoupling of the objective lenses results in a more efficient use of fluorophores – they are excited and detected only when needed – leading to lower levels of light induced damage (phototoxicity) and bleaching of fluorophores (photobleaching) as compared to other fluorescent

techniques such as confocal microscopy and two-photon microscopy (Reynaud *et al.*, 2008) [also see (Larson, 2010) for an introduction to multiphoton imaging]. Additionally, the use of a large sample chamber (Figure 1) precludes the need for mounting samples as squash preparations on slides or coverslips, allowing for the imaging of large, un-deformed samples that is not possible with most other imaging techniques.

Adjusting the thickness of the light sheet to match the depth of focus on the detection objective allows high contrast images to be acquired without using a pinhole to reject out-of-focus fluorescence (Greger *et al.*, 2007). Wide-field detection in SPIM (Greger *et al.*, 2007; Pitrone *et al.*, 2013) allows the system to capture signal, one frame at a time, removing some of the limitations to acquisition speed associated with systems that detect signal from single points [e.g. regular confocal microscopy] or lines [e.g. confocal line scanning microscopy] at a time (Pawley, 1995). Fast recording of high contrast two-dimensional information has made it possible to perform multidimensional time-lapse studies of dynamic events in large living samples, such as embryogenesis and development [e.g. Drosophila *Drosophila melanogaster* (Huisken *et al.*, 2004), zebrafish *Danio rerio* (Keller *et al.*, 2008a; Keller, 2013), volvox *Volvox globator* (Höhn *et al.*, 2015) and mouse *Mus sp*. (Ichikawa *et al.*, 2014)]; regeneration in zebrafish (Pinto-Teixeira *et al.*, 2013); microtubule behaviour in Xenopus frog *Xenopus laevis* oocytes (Keller *et al.*, 2008b); whole brain neuronal signalling [e.g. zebrafish (Ahrens *et al.*, 2013); Drosophila (Lemon *et al.*, 2015)] among others.

Light sheet fluorescence microscopy techniques such as SPIM are highly adaptable. This has led to the development of numerous avatars of the technique, each developed to enhance a different imaging parameter. Of these, SPIM and digitally scanned light sheet microscopy (DSLM) (Keller and Stelzer, 2008) are the most widely used. SPIM uses static light sheets produced using a cylindrical lens (Huisken *et al.*, 2004; Greger *et al.*, 2007; Pitrone *et al.*, 2013), while DSLM systems produce light sheets by

digitally scanning laser illumination at high speeds (Keller and Stelzer, 2008; Ichikawa *et al.*, 2014). Digitally scanned light sheets can be made to be thinner than is possible with static light sheets (Gao, 2015) and manipulated to have different beam profiles – Bessel (Fahrbach and Rohrbach, 2010; Fahrbach *et al.*, 2013a; Gao *et al.*, 2014a) or Airy (Vettenburg *et al.*, 2014), instead of a regular Gaussian profile (Keller and Stelzer, 2008). Bessel light sheets can penetrate deeper into thick tissue samples with a lower loss of signal as compared to Gaussian light sheets (Fahrbach and Rohrbach, 2010), while Airy light sheets can have a larger field of view (Vettenburg *et al.*, 2014). However, light sheets produced using a cylindrical lens require lower peak intensities and show lower levels of phototoxicity and photobleaching, and are easier to produce as compared to scanned light sheets (Gao *et al.*, 2014a), making them more favourable for long term imaging experiments. Similarly, light sheets can be manipulated to achieve two-photon excitation for larger depth penetration into thick tissue (Fahrbach *et al.*, 2013a; Mahou *et al.*, 2014), but this is at the cost of increased phototoxicity (Gao *et al.*, 2012). Other developments have involved the production of light sheets as projected patterns for higher resolution imaging [e.g. lattice light-sheet microscopy (Chen *et al.*, 2014)); Bessel plane SR-SIM (Gao *et al.*, 2012); LS-RESOLFT (Hoyer *et al.*, 2016)], or adaptive optics to correct for light scatter from tissue (Bourgenot *et al.*, 2012; Fahrbach *et al.*, 2013b). Implementing these modifications is not trivial and requires expensive, specialised equipment. Ultimately, SPIM in its native configuration has the capacity to track individual cells through space and time, with a high signal to noise ratio, low phototoxicity, and low photobleaching (Ritter *et al.*, 2008, 2010), making it a suitable technique for tracking and studying cellular interactions involved in post-copulatory sexual selection. Its capacity for live imaging of large tissue samples at sub-cellular resolution also makes SPIM suitable for imaging sperm storage sites and other structures in avian oviducts to understand the contributions of cryptic female choice to post-copulatory sexual selection.

Although the first version of a light sheet microscope was published over a century ago (Siedentopf and Zsigmondy, 1903), developments in light sheet microscopy only accelerated since Huisken *et al.* (2004) published their version, SPIM and used it to optically section Medaka embryos. The relatively recent development of SPIM is likely why this imaging technology has not previously been used for studying post-copulatory processes. In this chapter I describe the assembly, characterisation and operation of a custom-built SPIM system for studying structures and mechanisms involved in post-copulatory sexual selection in zebra finches [*Taeniopygia guttata*].

2.2. Microscope set up

A custom-built selective plane illumination microscope was constructed and maintained at the University of Sheffield. The microscope hardware and optical components were based on OpenSPIM (an open source microscopy platform; Pitrone *et al.*, 2013), but modified to include alternative lasers, sample positioning system and magnification at 28X. The microscope components can be categorised by function into illumination optics, detection optics, sample positioning assembly and automation control.

Illumination optics

Lasers emitting at 473 nm (30 mW, DPSSL with driver), 532 nm (10 mW, Thorlabs, Inc.) and 644 nm (110 mW, Vortran Laser Technology, Inc.) were used as illumination sources. Each of these formed a laser light sheet at the sample, allowing for up to three colour channels for imaging.

The laser beams were combined using dielectric mirrors (Thorlabs, Inc.; Figure 2 - **M1**, **M2**, **M3**, **M4**, **M5**, **M6**) and dichroic mirrors (Thorlabs, Inc.; Figure 2 - **DC1**, **DC2**). Passing each laser line through two mirrors each allowed for laser alignment using four degrees of freedom (X,Y, pitch

and yaw) before co-alignment using the dichroic mirrors. The lasers were co-aligned before the introduction of further optical components. This allowed for co-focussing of the colour channels with minimal chromatic aberrations. Continuously variable neutral density filter wheels (Thorlabs, Inc.; Figure 2 – **ND1**, **ND2**) were used to manually control the intensity of the red (644 nm) and blue (473 nm) laser lines without affecting the wavelength of the transmitted illumination. The intensity of the green (532 nm) laser could be controlled through a laser diode driver (Thorlabs, Inc.).

The combined beams were directed by a set of mirrors (Figure 2 – **M1-M8**, **DC1**, **DC2**) to the back of a beam expanding telescope (Thorlabs, Inc.; Figure 2 - **T1**; 8X). The telescope increased the width of the illumination beam to increase the fill at the back focal plane of the cylindrical lens (Thorlabs, Inc.; Figure 2 - **Cy**). This enabled the formation of a thin light sheet with a reduced beam waist [Saleh and Teich (1991) and see Box 1].

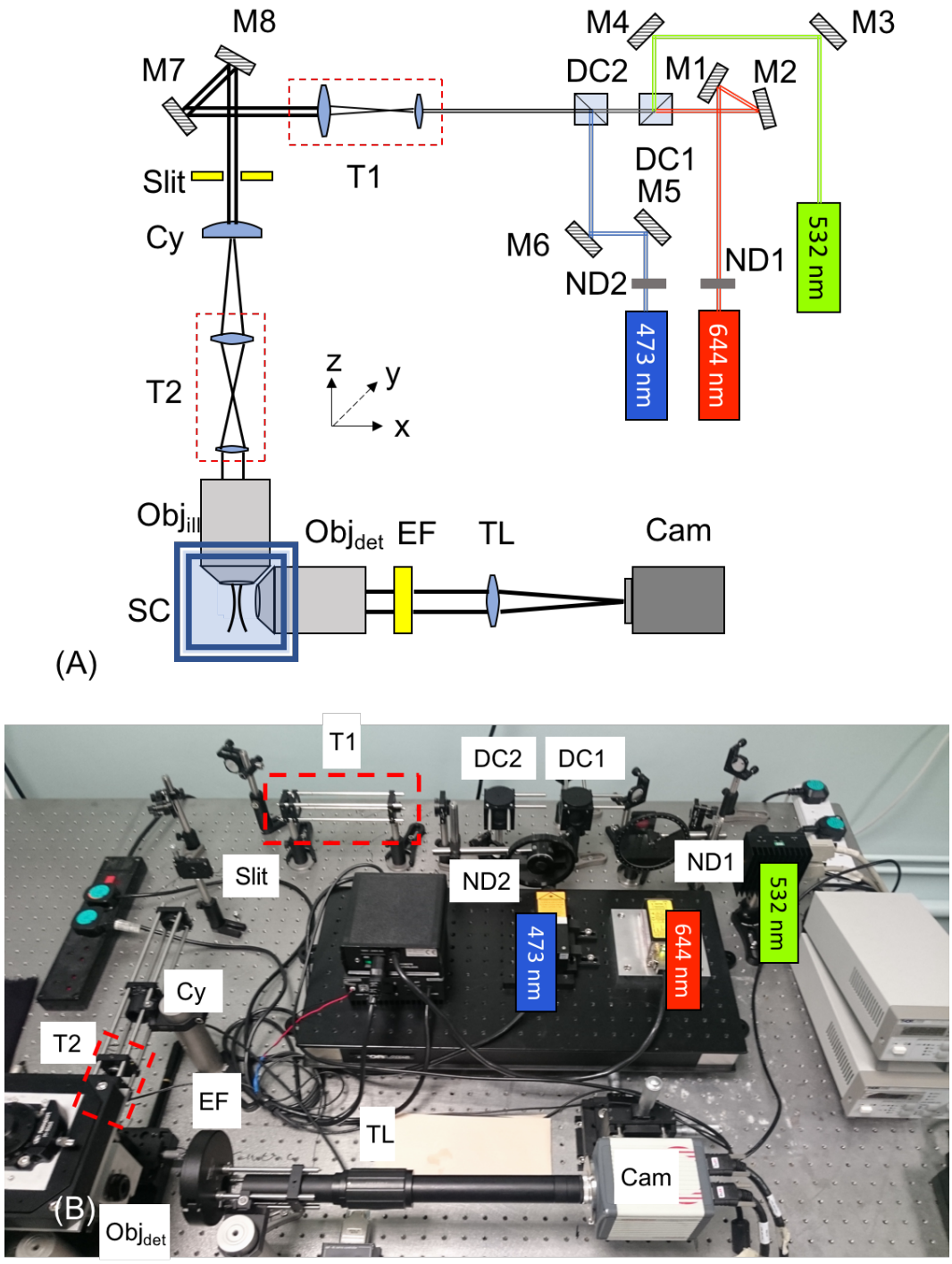

Figure 2: (A) Schematic diagram of SPIM illumination and detection optics. (B) Photograph of the SPIM set up at the University of Sheffield. Components include: lasers – 473 nm, 532 nm, 644 nm; ND filter wheels – ND1, ND2; mirrors – M1-M8; dichroic mirrors – DC1, DC2; beam expanding telescopes – T1, T2; cylindrical lens – Cy; Slit; Objectives – Obj_{ill}, Obj_{det}; sample chamber – SC; fluorescence emission filter – EF; tube lens – TL and sCMOS camera – Cam.

In our microscope set up, the light sheet was produced using a cylindrical lens (Figure 2 – **Cy**; f = 50 mm). Cylindrical lenses possess rotational symmetry along a single axis. This results in the cylindrical lens conferring asymmetry to the laser beam and transforming it by expanding or focusing along one axis only. The transformed beam is the laser light sheet.

A mechanical slit (Thorlabs, Inc.; Figure 2 - **Slit**) was introduced in the beam path before the cylindrical lens. This enabled further control of the light sheet beam waist (and therefore, light sheet thickness) by controlling the width of the beam incident on the cylindrical lens (see Box 1).

Box 1

The beam waist 'ω' of the light sheet is the minimum beam radius at its focal plane, and is inversely related to the radius of the incoming laser beam (Figure 3). The beam waist can be described using the following equation (Saleh and Teich, 1991),

$$\omega = \frac{\lambda_{ex} f}{\pi n r} \qquad (1)$$

Here, **ω** is the beam waist of the light sheet, λ_{ex} is the excitation wavelength, **f** is the combined focal length of the optical assembly consisting of the cylindrical lens, illumination objective lens and the second telescope (Figure 2 - **T2**), **n** is the refractive index of the imaging medium, and **r** is the radius of the laser beam incident on the cylindrical lens. By increasing the width of the illumination beam, the beam waist of the light sheet can be made optimally thin (Figure 3).

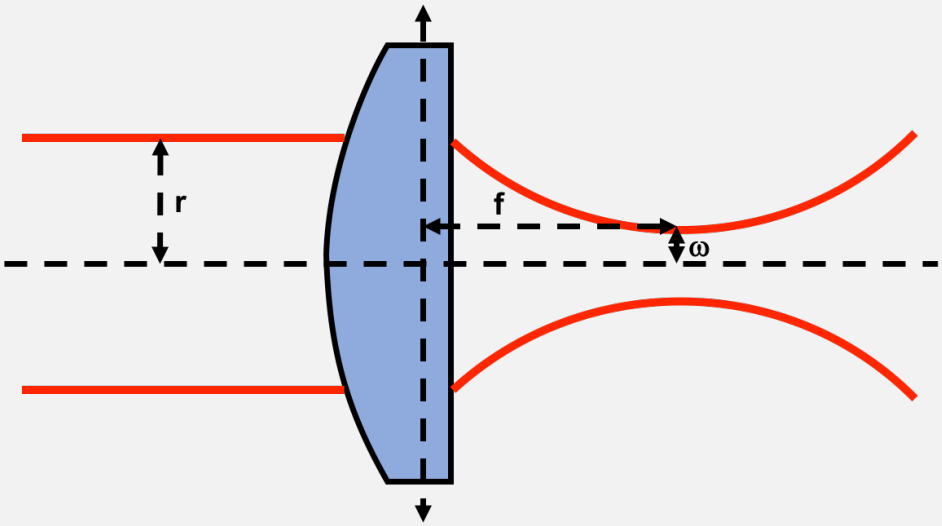

Figure 3: The light sheet beam waist 'ω' is inversely related to the radius 'r' of the incident beam and directly related to the focal length 'f' of the lens [image adapted from Santi *et al.* (2009) supplementary materials].

The light sheet was projected by a water immersion objective lens (10X, NA 0.3, WD 3.5 mm, Olympus; Figure 2 - **Obj**$_{im}$) on to the sample. Using an objective lens allows for higher numerical aperture (NA) than would be possible with just a cylindrical lens, resulting in thinner light sheets (see Box 2). Thin light sheets from high NA objectives confer better axial resolution to the system (Gao *et al.*, 2014a; Gao, 2015) but show a larger beam divergence resulting in a smaller optimal field of view (FOV) for imaging [(Siegman, 1986; Gao *et al.*, 2014b) and see Box 2]. To navigate this trade-off, objective lenses should be chosen to match the application. For imaging sperm selection mechanisms, a relatively large field of view is desirable [to permit imaging of larger female structures such as SSTs, which are 100-200 μm in length] and so a low NA illumination objective (NA 0.3) was chosen for the microscope.

Another telescope (Figure 2 - **T2**; 2X) was introduced between the cylindrical lens and the objective to help focus the light sheet in the focal plane of the detection objective.

Box 2

Numerical aperture of a lens can be described in terms of its focal length (Hecht, 2002),

$$NA = \frac{nD}{2f} \quad (2)$$

Here, **D** is the diameter of the lens. However, when the incident beam diameter is less than the diameter of the lens, the NA is dependent on the beam diameter instead (Hecht, 2002). The beam waist 'ω' of the light sheet can therefore be said to be inversely related to the NA of the lens from equations (1) and (2)

$$\omega = \frac{\lambda_{ex}}{\pi NA_{ill}} \quad (3)$$

Here the $\mathbf{NA_{ill}}$ is the numerical aperture of the illumination objective.

The distance from the focal point over which the focussed light sheet remains nearly collimated before it begins to diverge again (when it reaches a thickness of $\sqrt{2}\omega$) is called the Rayleigh range (χ) (Siegman, 1986)

$$\chi = \frac{\pi\omega^2}{\lambda_{ex}} \quad (4)$$

Twice the Rayleigh range defines the range where the beam divergence of the light sheet is negligible and presents the imaging region with the best axial resolution [(Siegman, 1986) and Figure 4].

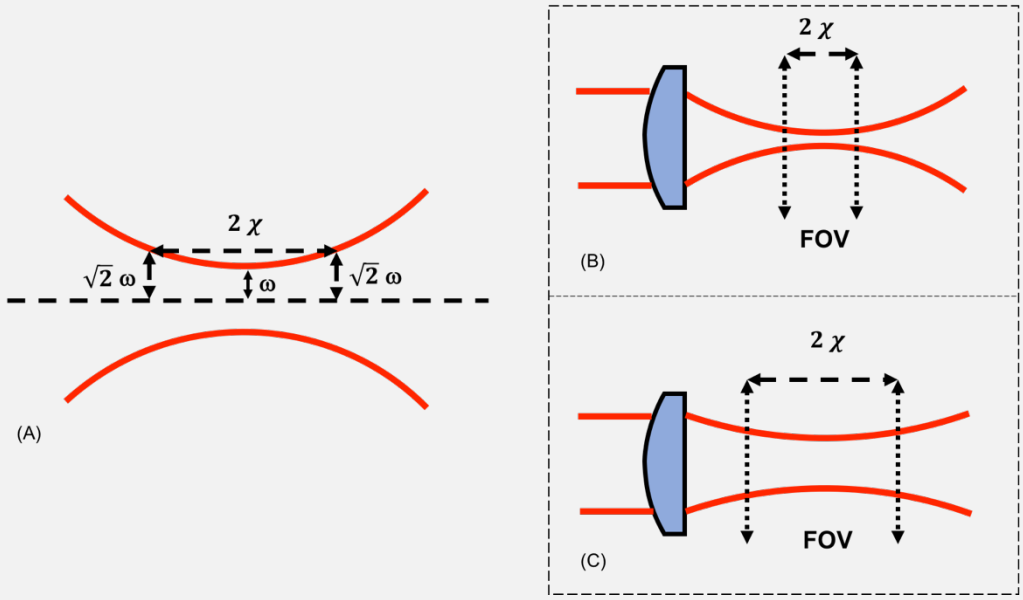

Figure 4: The Rayleigh range determines the field of view (FOV) of the system [adapted from (Siegman, 1986)]. (A) schematic of light sheet showing Rayleigh range. (B) high NA lens producing thin light sheet with small Rayleigh range. (C) low NA lens producing thicker light sheet with longer Rayleigh range. [(B) and (C) adapted from (Gao *et al.*, 2014b)].

Detection optics

The fluorescence signal emitted from the sample was detected by a second water immersion objective lens (20X, NA 0.5, WD 3.5 mm, Olympus; Figure 2 - **Obj**$_{det}$). Water immersion objectives have the benefit of dipping directly into the medium with the tissue samples. This allows for larger numerical apertures than is possible with an air interface due to the higher refractive index exhibited by water ($NA = n \cdot \sin\theta$), and removes the risk of spherical aberrations arising from having the signal pass through media of varying refractive indices (Hecht, 2002). Both the illumination and detection objectives are chosen to have large working distances (3.5 mm for both) to accommodate large tissue samples.

Fluorescence emission filters [Semrock, Inc.; Figure 2 – **EF**: 520 nm long pass (LP), 565 nm (24) BP, 680 nm LP] ensured that only the desired fluorescence signal passed through to a tube lens (Thorlabs, Inc.; Figure

2 – **TL**; f = 250 mm) positioned behind the detection objective. The image forming beams leaving the detection objective propagate as nearly parallel beams focussing at infinity. These beams were brought into focus by the tube lens and the image is formed on the sensor of a sCMOS camera (Orca Flash 4.0 V2 C11440-22CU Hamamatsu Photonics; Figure 2 – **Cam**).

The magnification of the system was calculated as follows,

$$M_s = \frac{f_t}{f_{det}} \quad (5)$$

$\mathbf{M}_s$ is the magnification of the system, $\mathbf{f}_t$ is the focal length of the tube lens and $\mathbf{f}_{det}$ is the focal length of the detection objective. Using a tube lens with a focal length of 250 mm and a detection objective with a focal length of 9 mm, the magnification was

$$M_s = 250/9 = 27.77778 \text{ X}$$

At full frame, the camera sensor size was 2048 X 2048 pxls with a pixel size of 6.5 μm. This put the pixel ratio of the system at,

$$1\text{pxl} = 0.234\ \mu\text{m}$$

So, the field of view (FOV) as captured by the camera sensor was 479.232 x 479.232 μm.

Experimental characterisation of light sheet thickness

The mirror at 45º method (Pitrone *et al.*, 2013) was used to simultaneously enable focusing and characterisation of the light sheet. For this, a small mirror (Figure 5 - **M**) was attached to a 1 mL syringe (Figure 5 - **Sy**) for ease of handling. This was lowered into the sample chamber using the

sample positioning assembly and positioned at a 45° angle between the illumination (Figure 5 - **Obj_{ill}**) and detection objectives (Figure 5 - **Obj_{det}**) using the rotation stage. The fluorescence emission filter was removed from the detection pathway. This set up made it possible to image the light sheet beam waist at the imaging plane.

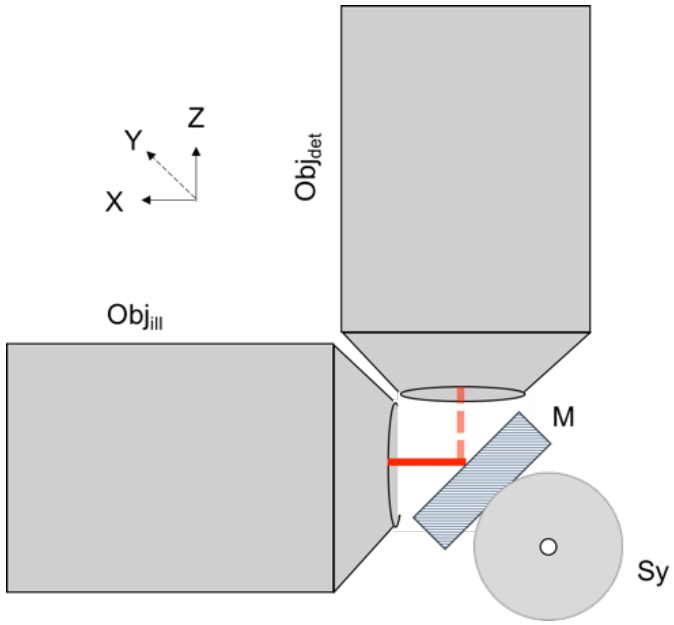

Figure 5: Experimental characterisation of light sheet in the SPIM set up. The mirror 'M' is placed at a 45° angle between the illumination objective 'Obj_{ill}' and detection objective 'Obj_{det}'. The mirror is attached to a 1 mm syringe to facilitate handling.

The mirror was translated along the X-axis and the light sheet was imaged at multiple X positions. The full width at half maximum (FWHM) of the light sheet beam waists was measured at each X position. As the name suggests, FWHM represents the width of the Gaussian intensity profile of the light sheet image measured at half the maximum intensity. The light sheet beam waist is thinnest at its focal plane and so the focus of each of the two objective lenses was adjusted to ensure that the light sheet was thinnest (in focus) in the focal plane of the detection objective. The cylindrical lens was adjusted to ensure that the long axis of the light sheet was perfectly in line with the focal plane of detection. The FWHM of the light sheet beam waist at its focal plane gave the thickness of the

light sheet (Figure 6). Light sheet width is a function of the wavelength of illumination [equation (3) in Box 2 and (Siegman, 1986)]. However, the green light sheet (λ_{ex} = 532 nm) in our microscope was thinner than the blue light sheet (λ_{ex} = 473 nm) [Table 1]. This discrepancy might be attributed to chromatic corrections built into the objective lenses by the manufacturers – the Olympus lenses used in our microscope are 'semi-apochromats'- corrected for chromatic and spherical aberrations.

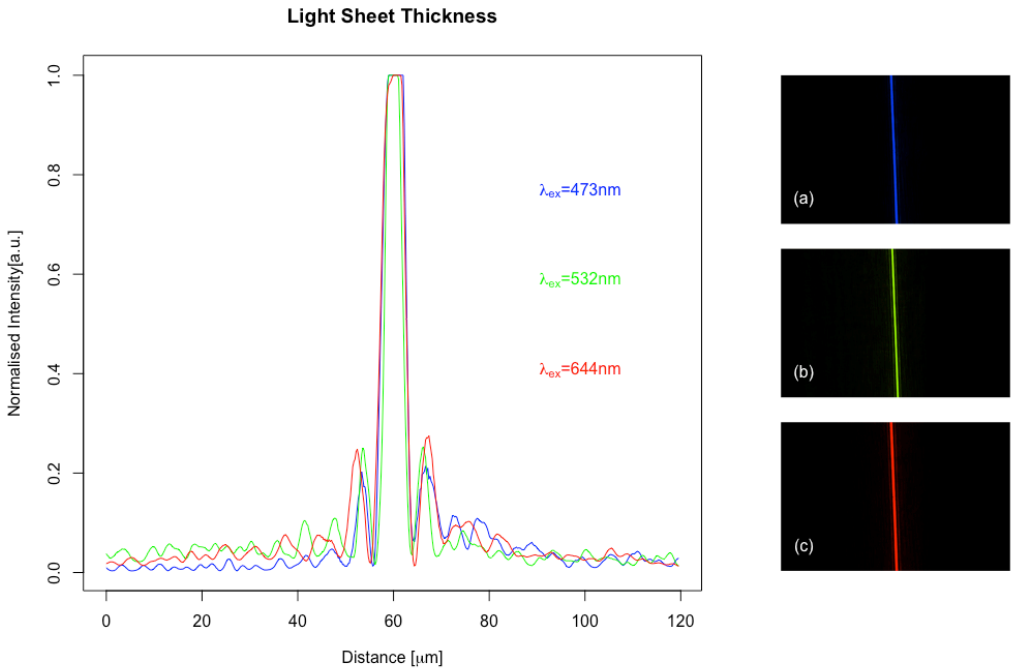

Figure 6: (a) Blue (λ_{ex} = 473 nm), (b) Green (λ_{ex} = 532 nm) and (c) Red (λ_{ex} = 644 nm) light sheets imaged using a mirror placed at 45° between the illumination and detection objectives. The intensity profiles of the three light sheets are overlaid above. The thickness of each light sheet is calculated by taking the FWHM of the respective intensity profile.

Table 1: Light sheet thickness for the three colour channels

	λ_{ex} = 473 nm	**λ_{ex} = 532 nm**	**λ_{ex} = 644 nm**
FWHM	4.060 μm	3.714 μm	4.300 μm

Resolution of the SPIM microscope

The resolution limit of an imaging system – the smallest distance resolvable between two discrete spots – is dictated by the wavelength of illumination and the numerical aperture (NA) of the optical system (Hecht, 2002). Conventional SPIM systems cannot break this resolution limit. The lateral resolution of the SPIM could be calculated using Rayleigh's criterion [Hecht (2002), and Power and Huisken (2017) - supplementary materials],

$$\delta_{lat} = \frac{0.61\lambda_{em}}{NA_{det}} \tag{6}$$

Where $\boldsymbol{\delta_{lat}}$ is the resolution limit in the lateral plane, $\boldsymbol{\lambda_{em}}$ is the wavelength detected and $\mathbf{NA_{det}}$ is the Numerical Aperture of the detection objective.

The axial resolution of the SPIM microscope could be described as a function of the light sheet thickness and the axial resolution of the detection optics (Gao, 2015).

$$\delta_{ax} = \left(\frac{1}{\omega} + \frac{n(1-\cos\theta_{det})}{\lambda_{em}}\right)^{-1} \tag{7}$$

The FWHM of the light sheet could be expressed in terms of the beam waist 'ω' (Pitrone *et al.*, 2013),

$$FWHM = \omega \cdot \ln(2) = \omega \cdot 0.693 \tag{8}$$

and

$$\frac{\lambda_{em}}{n(1-\cos\theta_{det})} \tag{9}$$

is the axial resolution of the detection objective where $\boldsymbol{\theta_{det}}$ is the half-angle of light collection in the imaging buffer. The thinner the light sheet and the better the detection optics, the better the axial resolution of the system. For the purposes of this thesis, the resolution of the microscope needed to be sufficiently sensitive to resolve individual zebra finch sperm [~3 μm radius and ~55 μm long (Birkhead *et al.*, 2005)].

Experimental characterisation of resolution from the point spread function (PSF)

In practice, the resolution of the system can be experimentally characterised by measuring the size of its point spread function (PSF) using sub-resolution fluorescent beads (Ritter *et al.*, 2008; Pitrone *et al.*, 2013). To determine the PSF of the microscope, fluorescent microspheres with a 200 nm diameter ($\lambda_{ex}/\lambda_{em}$= 540/560 nm, 2% solids, Invitrogen™) were used as point sources. The microspheres were diluted 1:100 in distilled water and then suspended in molten low melting point agarose (Sigma Aldrich) at a further dilution of 1:500. The agarose mixture is drawn into 300 μL syringes and left to set. The resulting agarose block was imaged in the SPIM by pushing out some of the agarose block with a plunger, such that it was still suspended from the syringe but could be imaged without a plastic interface. Laser excitation was at 532 nm and a 565 nm (24) BP fluorescence emission filter (Semrock, Inc.) was used and Z-stacks - a series of images at consecutive Z step positions - were acquired near the outer edge of the agarose block.

Ten microspheres were randomly selected from the image Z-stacks. For each microsphere, the intensity profile was recorded in the XY, YZ and XZ planes giving three sets of intensity measurements for each; two lateral (XY, XZ) and one axial (YZ). The intensity data from the lateral measurements and the axial measurements were collated separately. A Gaussian curve was fitted to each combined data set and the FWHM was

taken for each Gaussian curve fit to give the lateral and axial PSFs of the microscope (Figure 7).

The FWHM of the PSF is a conservative estimate of the resolving power of the microscope with smaller point sources (here fluorescent microbeads) giving proportionally smaller PSF values, while the Rayleigh criterion calculates the smallest detectable separation between point sources, giving a more sensitive estimate of resolution. Optical aberrations also affect the PSF of the microscope and so, the closer the PSF is to the Rayleigh criterion, the better aligned the microscope.

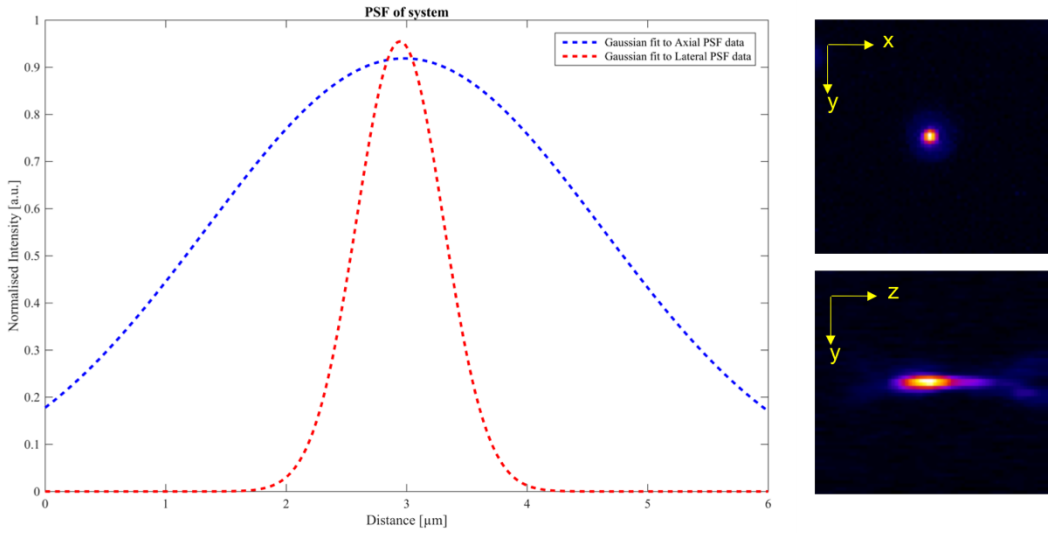

Figure 7: (A) Gaussian curves fitted to experimental data from lateral (red) and axial planes (blue). (B) Image of a fluorescent microsphere along the XY and (C) along the YZ planes to illustrate the system PSF.

Table 2: Experimental and Theoretical PSF of the system

	Lateral PSF	Axial PSF
Experimental	0.825 μm	3.732 μm
Theoretical[1]	0.689 μm	2.796 μm

[1]Theoretical PSF was calculated using equations (6), (7) and (8) above.

Sampling rate

Setting an optimal sampling rate - image voxel (three-dimensional pixel) size – allows the microscope system to theoretically reach its full resolution. The Nyquist criterion dictates the sampling rate required to form an image from the sample under a microscope (Pawley, 1995). The Nyquist limit along lateral axes for a light sheet based microscope system could be described to be (Gao *et al.*, 2014a),

$$\frac{\lambda_{em}}{4NA_{det}} \tag{10}$$

The PSF of the system was not isotropic (see Table 2 above) and so setting an isotropic voxel size would result in oversampling in the Z-axis. Generally, the sampling size is set to less than a third of the resolution and so the sampling in Z (Z-step size) was chosen to be less than a third of the axial PSF (experimental). The sampling rate of the system was set slightly less than the Nyquist limits for all the colour channels (see Table 3).

Table 3: Determining optimum sampling rate

Axis	Nyquist limit at (λ_{ex}/ λ_{em})			Sampling rate
	473/520 nm	**532/565 nm**	**644/680 nm**	
X	260 nm	282.5 nm	340 nm	234 nm
Y	260 nm	282.5 nm	340 nm	234 nm
Z	1244 nm	1244 nm	1244 nm	750 nm

Sample positioning

The total z-stack volume of the sample available for imaging is physically constrained by the working distance of the objective lenses coupled with the physical arrangement of the objective lenses. Practically, this effective

imaging region is further constrained by the depth penetration of the system. Cellular resolution (6 μm) (Huisken *et al.*, 2004) has been reported up to a depth of 500 μm in semi-transparent Medaka [*Oryzias latipes*] embryos with a conventional SPIM. In the more opaque mouse [*Mus sp.*] early embryo, imaging depths of 150 μm have been demonstrated (Ichikawa *et al.*, 2013). Avian oviduct tissue, however, is thick (~5 mm across at the utero vaginal junction 'UVJ') and muscular. Preliminary trials showed the effective depth to which SPIM microscopes could image through avian oviduct tissue to be about 100 μm [Figure 8 (A) and (B)]. Similarly, trials using two-photon excitation (Zeiss LSM 780 META multiphoton invert with Solent Scientific environmental chamber) showed a comparable depth to which structures could be clearly resolved [Figure 8 (C)].

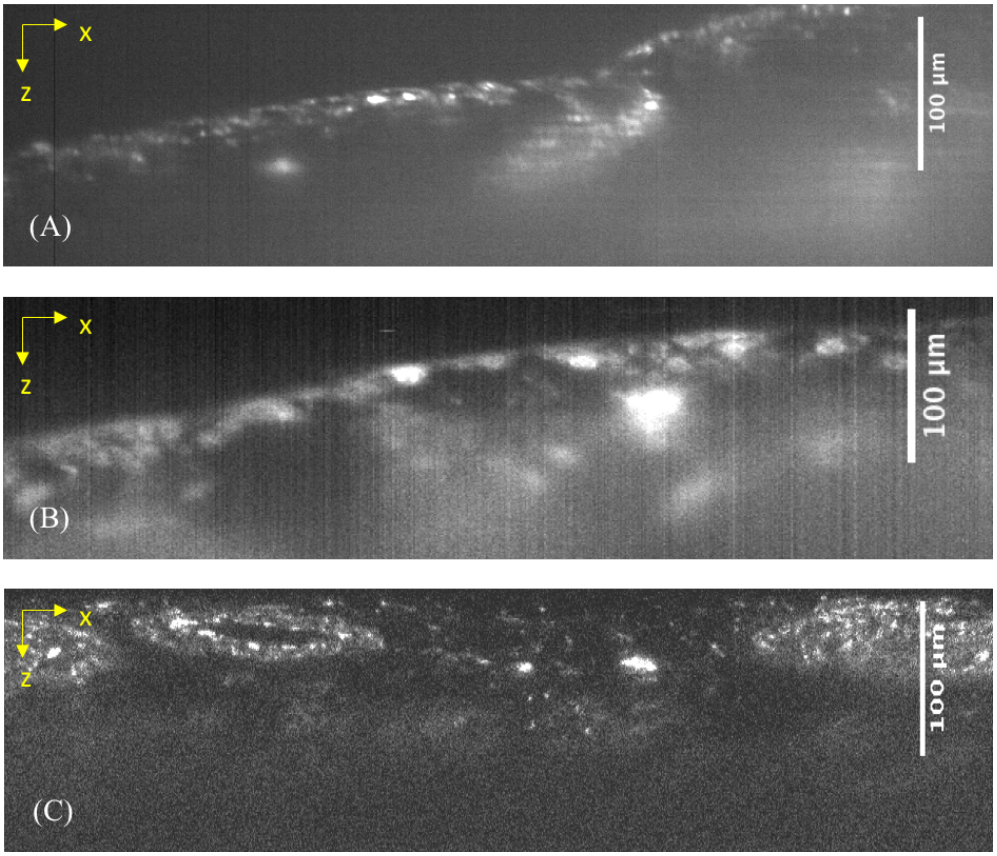

Figure 8: Zebra finch oviduct imaged using (A) our custom-built SPIM [λ_{ex} = 473 nm] (B) the commercial Zeiss Z.1 light sheet microscope [λ_{ex} = 405 nm] and (C) a Zeiss LSM 780 META two-photon microscope [λ_{ex} = 740 nm]. There is a rapid reduction in signal quality beyond 100μm from the surface of the tissue. UVJ samples are from different females.

The effective imaging volume of the sample in our system was therefore 100 μm deep along the illumination path, 100 μm deep along the detection path, and unconstrained (but limited by sample chamber dimensions) in the third axis (Figure 9). So, for large samples, the long axis of the sample volume was aligned with the unconstrained axis for imaging.

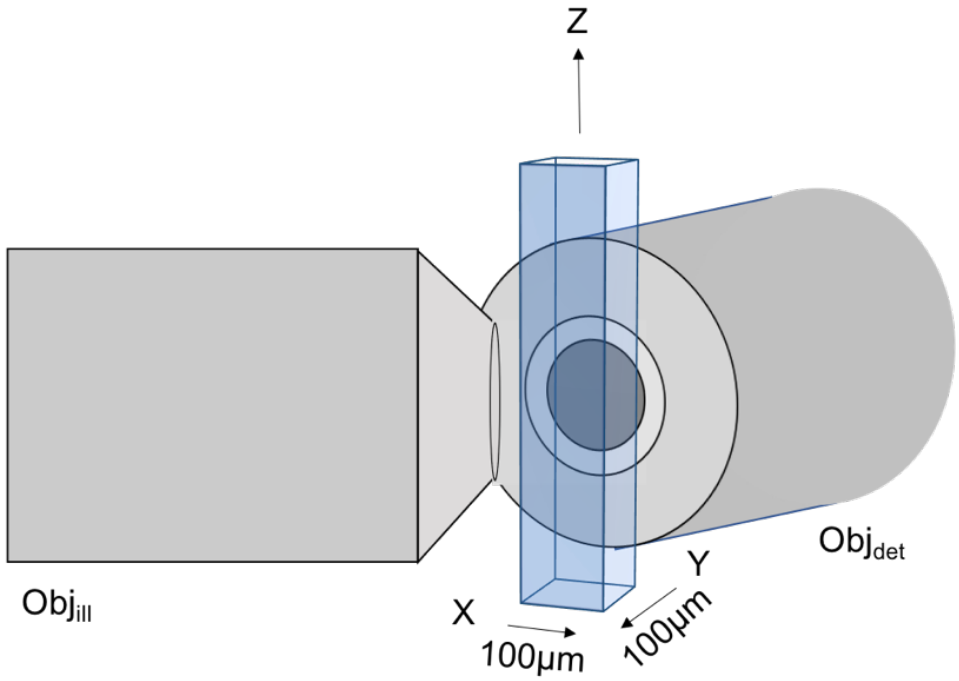

Figure 9: Effective imaging volume. Imaging volume is constrained by penetration depth along the illumination and detection axes but is only constrained by the dimensions of the sample chamber in the Z-axis.

The large sample chamber and a four-axis (X, Y, Z and rotation (θ)) sample positioning system in the microscope allowed for easy imaging of agarose-embedded samples at multiple angles to acquire accurate 3D reconstructions.

When imaging oviduct tissue, to maximise the number of sperm storage tubules (SSTs) imaged with every field of view and to optimise for the recording of information at the SST openings (Chapter 5), the tissue was positioned such that the openings of the SSTs were angled to face the

detection objective – using the coarse positioning system while streaming video to a computer screen, and the light sheet skimmed this surface. Bespoke sample holders were prepared for mounting UVJ tissue (see Chapter 5) and the tissue sample was prepared so that the long axis of the sample ran parallel to the mucosal surface. The sample preparation and mounting methods for sperm cells as well as UVJ tissue are further detailed in Chapter 4 and 5 respectively.

Hardware

The sample positioning system used here differed from the OpenSPIM 4-D stage (Pitrone *et al.*, 2013) and was assembled using three stepper motor stages (NanoPZ series, Newport Corporation; Figure 10 – **SM1, SM2, SM3**), a rotation stage (M-RS65, Newport Corporation; Figure 10 – **Rot**) and a piezo motor nanostage system (PIMars P-562.2CD, Physik Instrumente Ltd; Figure 10 – **Piezo**). A hand-held controller and switchbox were used to control the stepper motor translation stages to enable coarse motorised positioning of the sample along the X, Y and Z axes. The piezo stage was controlled using a piezo controller (E-725.3CD, Physik Instrumente Ltd) and allowed for fast scanning of the sample along the Z-axis. The rotational stage was motorised by attaching it to a stepper motor actuator (NanoPZ series, Newport Corporation) but could also be controlled manually.

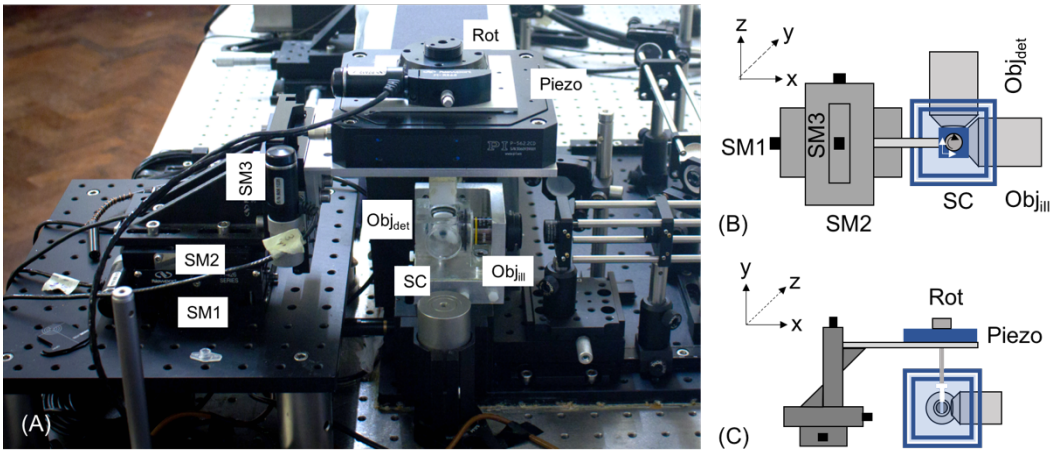

Figure 10: The sample positioning assembly; (A) photograph, (B) schematic top view and (C) schematic side view. Components include: Stepper motor stages – SM1, SM2 and SM3; piezo stage – Piezo; rotation stage – Rot; sample chamber – SC; objective lenses - Obj_{ill}, Obj_{det}.

Prior to the piezo stage being installed, tests were performed to determine the suitability of the stepper motor assembly for sample scanning. A LabView™ [version 14.0.1 (64 bit)] virtual instrument (VI) was written to program the camera to capture an image every time the stepper motor driven Z-axis translation stage finished taking a scanning step. The backlash from the stepper motors at every scanning step resulted in distorted images due to uncontrolled sample movement [Figure 11 (A) and (C)]. The scan program was then modified to perform a continuous scan instead of the step-wise scan. The stepper motors did not possess position sensors (Newport Corporation, 2006) and so Z-step size could not be programmatically set. Although the resulting images from continuous scans no longer showed any distortions in the XY plane from sample movement [Figure 11 (D)], the Z-step size was difficult to control due to its dependence on camera acquisition rate and the speed of writing the images to disk. The installation of the piezo stage helped overcome these limitations by allowing for Z-step size to be programmatically controlled during continuous scans.

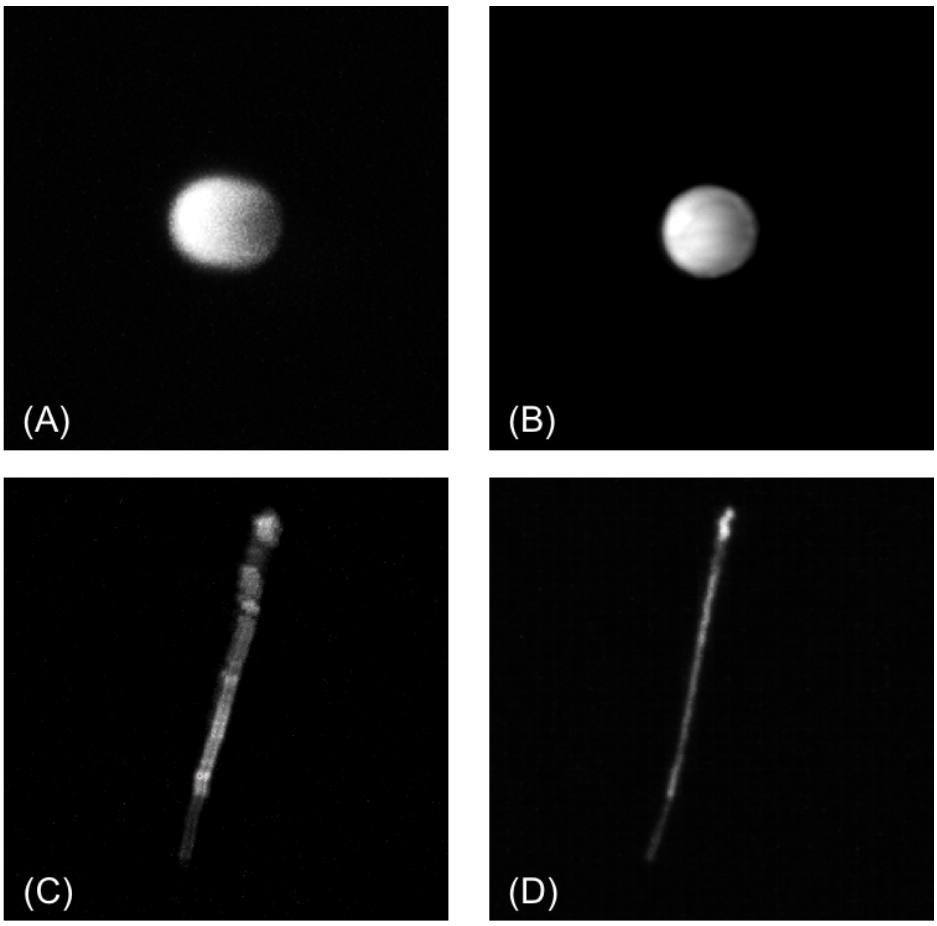

Figure 11: Distorted maximum intensity projections (MIP) of (A) 10 μm FluoSpheres™ (Molecular Probes™, OR), and (C) zebra finch sperm imaged using the start-stop script with stepper motor translation stages. (B) MIP of 10 μm FluoSpheres™ imaged using the piezo stage and (D) MIP of zebra finch sperm [from the same male as in image (C)] using a continuous scan with the stepper motor stage.

The stepper motor actuators were capable of movement at a range of speeds expressed as μsteps/sec, where each μstep corresponds to approximately 10 nm (Newport Corporation, 2006). The maximum travel range for the actuators was 12.5 mm as documented by the manufacturers (Newport Corporation, 2006). The large travel range made these translation stages ideal for coarse sample positioning along with the rotation stage.

System automation

The SPIM microscope was controlled and automated using a desktop computer. This enabled the user to access the settings for the system components, programme experiments and macros, and most importantly, enabled the system to run at full speed. The three main points of external control on the system were the control box for the stepper motor actuators, the controller for the piezo stage and the camera. Each of these could be programmatically controlled via the individual software packages provided by the manufacturers - NanoPZ-Util (version 1.0.2), Newport Corporation; PIMikroMove (version 2.18.0.0), Physik Instrumente Ltd; HCImageLive (version 4.2), Hamamatsu Photonics, or through LabView™ [version 14.0.1 (64 bit)] VIs. The imaging protocols described in this thesis used the individual software packages listed above.

Data from the sCMOS camera (Orca Flash 4.0 V2 C11440-22CU, Hamamatsu Photonics) were streamed to a computer via an Active Silicon Phoenix camera link card to a PCIe x16 card slotted into a Windows 7 computer. The camera was in turn connected to the three lasers via TTL cables for programmatic control of laser channels. This had two major benefits: firstly, to minimise sample exposure to illumination by switching the laser on only when the camera shutter was open and secondly to automate the switching of channels during an imaging session.

Apart from sending TTL signals, the camera was also capable of receiving signals from other instruments. The piezo stage had an inbuilt position encoder which accurately outputted the current position of the stage at any given instance. By connecting a TTL cable from the piezo controller (E-725.3CD, Physik Instrumente Ltd) to the camera, the camera shutter could be programmatically synced with the scanning system.

A switchbox allowed for switching between control of the three stepper motor translation stages. Additionally, a handheld controller enabled manual control of the translation stage assembly.

2.3. SPIM general imaging methods

The general microscopy workflow is illustrated in Figure 12. The instrument parameters were set using the individual software packages – PIMikroMove for the piezo scan system, HCImageLive for the camera and NanoPZ-Util for the coarse positioning system. The lasers were selected and controlled through the camera with the HCImageLive software. As described in the system automation section above, the camera shutter was triggered through the piezo.

The imaging media was loaded manually to fill the imaging chamber using a 5 mL syringe. Samples were mounted either in agarose using a 300 μL syringe (see Chapter 4) or using modified sample holders (see Chapter 5). The syringes/sample holders were suspended into the sample chamber vertically from above by a sample holding arm that extended from the rotation stage in the sample positioning assembly (Figure 10). The filter wheel was adjusted manually to select the appropriate fluorescence emission filter. The laser was then turned on and the camera shutter opened to visualise the sample, which was brought to the image start position using the coarse positioning assembly.

Once at the start position, the camera and lasers were switched to TTL mode and the scan was started. The images captured during the scan were queued to memory before being written to disk at the end of the scan as multi-image '.cxd' files. After each scan, the piezo was returned to the start position, bringing the sample back with it. This was repeated for every colour channel, multi-view angle, time point and/or new imaging area recorded.

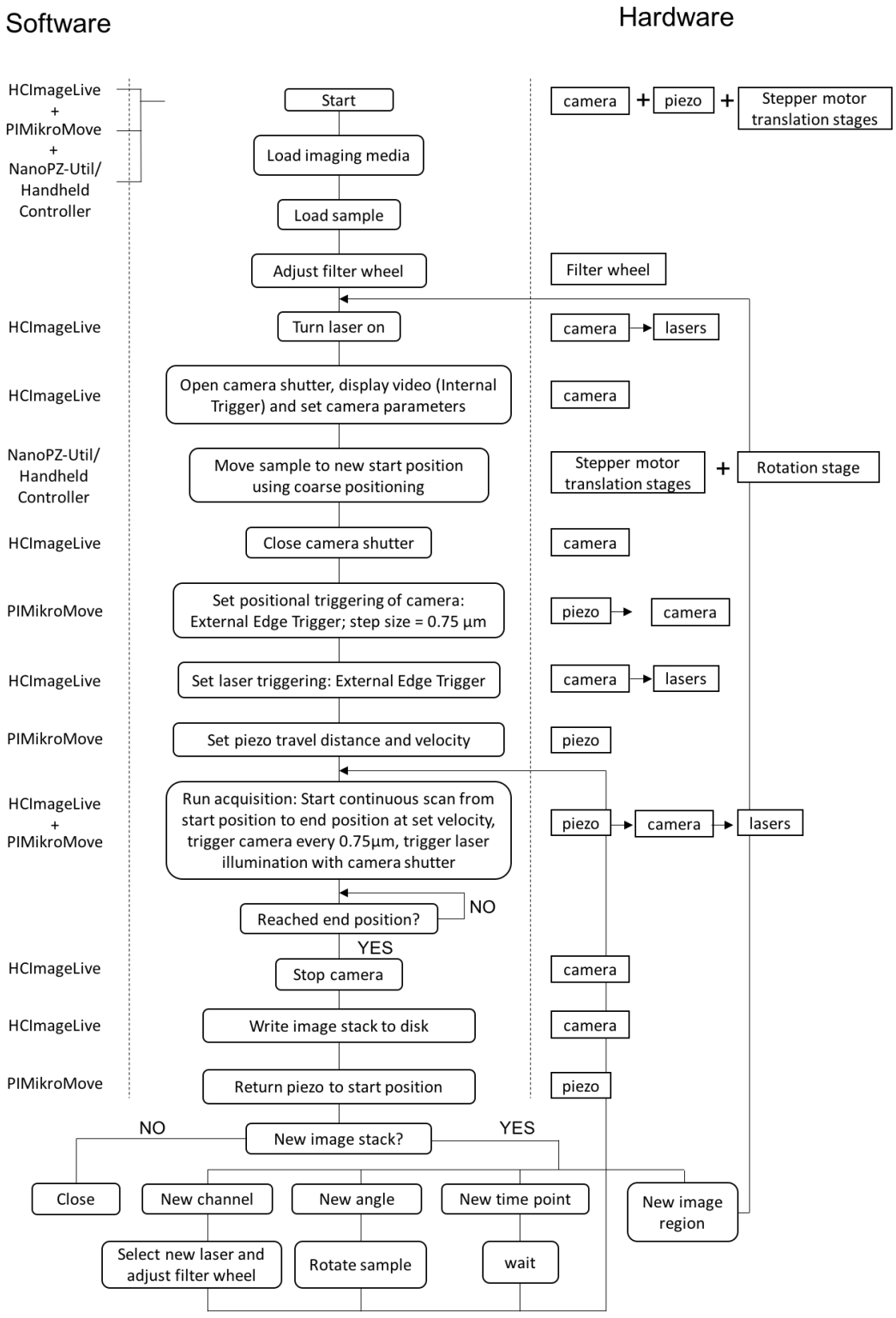

Figure 12: Workflow diagram for SPIM general methods. Adapted from (Greger *et al.*, 2007)

The modular nature of the microscope made it possible to optimise it for imaging single zebra finch sperm (Chapter 4), and the large UVJ tract tissue samples (Chapter 5), by allowing for the installation, replacement and/or removal of hardware and optical components when needed. The SPIM microscope with the resulting modifications allowed me to obtain detailed three-dimensional information on zebra finch sperm and sperm storage tubules (SSTs) giving further insight into their form and function.

Chapter 3.

Assessing the effect of fluorescent dyes on sperm performance

3.1. Introduction

Optical sectioning with fluorescence imaging allows us to non-destructively 'slice' through large, live tissue samples, providing immense potential for visualising post-copulatory sexual selection processes *in vivo*, in real-time. However, the success of live fluorescence imaging is reliant on the choice of suitable fluorophores. The photo-physical properties of a fluorophore can affect both the spatial and temporal resolution achieved while imaging (Lakowicz, 2006b). For *in vivo* tracking of single cells such as sperm, the ideal fluorophore must be of small size so as not to impede sperm motility. The method of targeting, loading and delivering the fluorophore should not compromise the viability of the sperm cells. The fluorophore must display bio-stability and insensitivity to the *in vivo* environment, including pH changes. For studying molecular signalling and transport events between sperm cells and the female reproductive tract tissue, fluorophores that display sensitivity towards molecular targets or products should be used. Fidelity of binding is highly desirable as fluorescence transfer or leaching of the fluorophore into other, non-target cells and tissues will impede or bias data collection. For long term tracking purposes, the fluorophore

should be resistant to photo-bleaching and not induce cytotoxicity or genotoxicity in the sperm cells.

Fluorophores can serve to target specific sperm cell components including the nucleus (Garner *et al.*, 1986; Garner and Johnson, 1995), acrosome (Lee *et al.*, 1987), mitochondria (Graham *et al.*, 1990; Sutovsky *et al.*, 1996), plasma membrane (Garner *et al.*, 1986; Harrison and Vickers, 1990) or even single molecules such as sperm acrosome membrane proteins (Frolikova *et al.*, 2016). Fluorophores that have been used to label sperm previously include recombinant proteins [e.g. Drosophila *D. melanogaster* sperm (Civetta, 1999; Manier *et al.*, 2010)], peptide conjugates [e.g. sea urchin *Strongylocentrotus purpuratus* & *Lytechinus pictus* sperm (Cardullo *et al.*, 1994)], antibody conjugates [e.g. field mice *Apodemus sylvaticus* & *Apodemus microps* sperm (Sebkova *et al.*, 2014; Frolikova *et al.*, 2016)], organic dye molecules [e.g. mammalian sperm; multiple species (Garner *et al.*, 1986)], or metal complexes such as quantum dots [e.g. sea urchin, pig *Sus sp.* and mouse *Mus sp.* sperm; (Robinson *et al.*, 2005)]. Most studies that have successfully documented live sperm-female interactions have employed recombinant fluorescent proteins (FPs). Specifically, variants of green fluorescent protein (GFP) and red fluorescent protein (RFP) have been used to track sperm (Manier *et al.*, 2010; Köttgen *et al.*, 2011; Chang and Suarez, 2012; Marie-Orleach *et al.*, 2014, 2016). In birds, although transgenic GFP lines having been successfully produced (McGrew *et al.*, 2004; Chapman *et al.*, 2005; Scott and Lois, 2005; Agate *et al.*, 2009), there has been a lack of information about the fidelity of FP expression in sperm cells as well as the viability of such FP labelled sperm (and the organisms that produce them). Apart from FPs that are genetically encoded to produce intrinsic fluorescence, all other fluorophore types need to be applied to sperm extrinsically, *in vitro*, prior to insemination. These labelling protocols often involve multiple rounds of pelleting and resuspension of sperm at every stage, which may damage sperm. The results of previous *in vitro* mixing trials with zebra finch [*Taeniopygia guttata*] sperm suggest that caution should be exercised when subjecting sperm to aspiration and centrifugation as

this could lead to loss of viability [J. Thompson (2012), unpublished data]. This problem can be overcome by directly applying cell permeant organic dyes that are readily accepted into cells, using protocols that avoid multiple transfers and washings. The ease with which cell permeant dyes can be used, combined with their wide commercial availability, has made them popular for sperm studies *in vitro* (Garner *et al.*, 1986; Graham *et al.*, 1990; Firman and Simmons, 2014; Bennison *et al.*, 2015; Nosrati *et al.*, 2015).

Despite their wide use *in vitro*, few organic dyes have been used to track live sperm in female tissue (*in vivo* or *ex vivo*) and fewer still have been assessed for their effect on sperm behaviour or sperm-female interactions. Of the organic dyes that have been used to study sperm *in vivo*, the membrane labelling dye Octadecyl Rhodamine Chloride B (Molecular Probes, Eugene, OR) has enabled live tracking of sperm (Druart *et al.*, 2009), and the nucleic acid dye Hoechst 33342 (Molecular Probes, Eugene, OR) has been used to detect sperm in storage tubules in sectioned oviduct tissue (Bakst, 1994; McDaniel *et al.*, 1997; King *et al.*, 2002). Additionally, Lymbery *et al.* (2016) showed that treatment with Mitotracker Green FM had no effect on sperm motility and fertilisation success in the bivalve *Mytilus galloprovincialis*. Little is known about the effect of Octadecyl Rhodamine Chloride B on sperm viability. Hoechst 33342 has been found to have no detrimental effect on sperm motility (King *et al.*, 2002) or fertility success (McDaniel *et al.*, 1997), but was found to impair embryo survival in poultry (McDaniel *et al.*, 1997). King *et al.* (2002) reviewed a range of lipophilic membrane dyes (DiQ, $DiOC_{16}$, DiI, DiI-SP) and a cytoplasmic dye (Cell Tracker™ Orange) alongside Hoechst 33342, and found all except Hoechst 33342 greatly impaired sperm motility. Since then, the selection of commercially available organic dyes has multiplied but the potential of these for labelling live sperm remains unexplored. The study of sperm selection in birds and other vertebrates would be greatly enhanced by identifying not just one, but several suitable organic dyes with a range of fluorescence spectra and target specificities. The use of multi-colour imaging, with different ejaculates

labelled with dyes that excite or emit at different wavelengths and are therefore detected separately, would allow multiple competing ejaculates to be tracked simultaneously in the oviduct, revolutionising the study of sperm competition.

In this study, I tested a range of commercially available dyes that excite in both the blue (470-500 nm) and green (530-560 nm) ranges, for labelling efficacy and effect on sperm behaviour in the zebra finch. I included both nucleic acid dyes and membrane dyes in order to assess their suitability across a range of applications. Nucleic acid dyes are effective for locating and following gross sperm movements but not for visualising contact between the sperm surface and the female tissue. Plasma membrane dyes would help to overcome this limitation by making the entire sperm cell detectable; however, membrane dyes work by inserting themselves in the glycolipid bilayer of the plasma membrane, so there is a possibility that this could hinder sperm motility and behaviour. Encouragingly however, sperm labelled with the membrane dye Octadecyl Rhodamine Chloride B, have been shown to be successfully transported through the ewe genital tract post intra-uterine insemination, and displayed binding with the oviduct epithelium (Druart *et al.*, 2009), indicating that certain membrane dyes may be suitable for studying sperm behaviour *in vivo*.

I report three main experiments in this chapter. For each dye, I compared (1) the labelling efficacy on formalin-fixed sperm. For those dyes that performed well in the labelling efficacy trials, I then assessed (2) their effect on the motility of live sperm *in vitro*. Finally, for those dyes deemed nontoxic in the motility trials, I tested (3) their effect on sperm-female interactions by measuring the rate of acceptance of dye-treated sperm into the sperm storage tubules.

3.2. Materials and Methods

Animals

Zebra finches from a captive population at the University of Sheffield were used for this study (Birkhead *et al.*, 2005; Bennison *et al.*, 2015). All birds used were between 2-3 years old to ensure they were in optimum health and breeding condition at the time of collecting tissue. Male birds used in experiments (1) and (2), which tested for labelling efficacy and effects on sperm motility respectively, were housed in cages (dimensions: 1.2 x 0.5 x 0.4 m) in groups of 10, separated from groups of 10 females in an identical cage behind a wire mesh. This arrangement kept the males physically separated from the females while still receiving visual and acoustic cues to ensure they maintained breeding condition and produce sperm. Preventing physical contact avoided the risk of sperm depletion that would result from copulation (Birkhead and Fletcher, 1995). At the time of running each experiment, the males were humanely euthanized by cervical dislocation in accordance with Schedule 1 [Animals (Scientific Procedures) Act 1986] and dissected immediately. The left seminal glomerus (SG) was extracted and the connective tissue encasing it was removed to unravel the SG. Semen was collected by squeezing the distal region of the SG in warm Ham's F10 Nutrient Mix [Life Technologies, UK] as described in Bennison *et al.* (2014 – see electronic supplementary material).

For experiment (3), which tested for dye effects on sperm-female interactions, male-female pairs were set up in two cages (dimensions of each: 0.6 x 0.5 x 0.4m) placed side-by-side and separated by a wire mesh, with the male and female on either side. Care was taken to ensure the females were either virgins or had been separated from males for at least two weeks prior to being set up. This ensured that the females had no sperm in their sperm storage tubules (SSTs) [sperm can be stored for up to 12 days after mating in zebra finches (Birkhead and Møller, 1992)]. A pair of nest boxes was attached where the cages joined, positioned

adjacent to each other so that both birds had access to a nest box. A window was fashioned in the dividing wall of the pair of nest boxes, overlaid with a piece of wire mesh. This set up ensured that the male and female established a normal breeding pair bond, leading the female to come into full breeding condition, with a fully developed oviduct and SSTs, and ensuring the male produced sperm. The onset of egg laying was used as an indicator of full oviduct development. Female zebra finches lay an average of five eggs per clutch (Haywood, 1993) but occasionally, a single egg is laid in isolation (*pers. Obs.*). The laying of a single egg did not reliably indicate that a female would continue to lay a full clutch, so only after a second egg had been laid was the pair used for the experiment. Semen was collected from the left SG of the male as detailed for experiments (1) and (2). Further details of the three experiments are elaborated in the relevant subsections below.

Fluorescent dyes

Three nucleic acid dyes and four membrane dyes were assessed for their labelling efficacy and effect on sperm performance. A major drawback with fluorescence imaging is background fluorescence from unbound fluorophores, which contribute to background fluorescent noise and therefore hinder the ability to detect fluorescence signal from sperm. As part of the assessment on labelling efficacy, background fluorescence noise was also compared across the dyes. The nucleic acid dyes assessed in this study were SYBR 14, SYTO 13 and SYTO 82. Of these, SYBR 14 has been widely used as part of the Live/Dead sperm viability kit (Molecular Probes Inc., UK), to assess the viability of sperm from across a range of systems [e.g. bovines (Garner *et al.*, 1994), yellow dung fly *Scathophaga stercoraria* (Bernasconi *et al.*, 2002), sheep *Ovis aries* (Druart *et al.*, 2009), quail *Coturnix japonica* (Hiyama *et al.*, 2014)]. Although this dye can be used to assess whether or not the sperm plasma membrane is intact, very little work has been done to understand whether the dye itself has an effect on sperm viability. SYTO 13 and SYTO 82 belong to the same SYTO family of dyes as SYBR 14 and have been used to monitor sperm motility

and interactions with female tissue or proteins [bees *Acromyrmex echinatior* (Liberti *et al.*, 2016); mice *Mus domesticus, Mus musculus musculus, Mus spicile & Mus spretus* (Martín-Coello *et al.*, 2009; Firman and Simmons, 2010)] but again, there is little information about the effect of the dyes on sperm function.

The membrane dyes assessed were Octadecyl Rhodamine Chloride B, FM1-43, 4-Di-16-ASP and 4-Di-10-ASP. Of these, Octadecyl Rhodamine Chloride B has already been demonstrated to be a good candidate for tracking sperm behaviour in sheep (Druart *et al.*, 2009). FM 1-43 is a small molecule non-toxic membrane dye and has been used to track spermatogenesis in *Caenorhabditis elegans* (Washington and Ward, 2006; Bae *et al.*, 2009). 4-Di-16-ASP and 4-Di-10-ASP belong to the same dialkylaminostyryl group of probes as FM1-43 and have similar chemical structures and comparable properties (Spence and Johnson, 2010a). Apart from Octadecyl Rhodamine Chloride B, all membrane dyes have not been previously assessed for their suitability for tracking sperm. There are innumerable organic dyes available but these seven were identified as priority candidates due to their high cell permeability and apparent low toxicity (assumed from live-cell applications listed above).

I refer to 4-Di-10-ASP as 'Di10', 4-Di-16-ASP by its commercial name 'DiA' and Octadecyl Rhodamine Chloride B by its commercial name 'R18'. Labelled samples from all experiments were examined using a wide-field fluorescence microscope (Leica DMBL with Infinity 3 camera, Luminera Corporation).

DiA, Di10 and FM1-43 have very broad emission spectra and therefore, although these dyes have their maxima in the yellow range, they can be appreciably detected between 510 nm (green) – 690 nm (red) (Spence and Johnson, 2010b). The 'I3' fluorescence filter set [for Leica DMBL] used detects these dyes in the green range. The same filter set is used to detect green fluorescence from SYBR 14 and SYTO 13. R18 and SYTO 82 are both detected as red using the 'N2.1' filter set [for Leica DMBL].

Working concentrations for fixed sperm (Table 1, 'Fixed Sperm') were selected from preliminary trials to identify the optimum concentration for maximal labelling of sperm. In most cases, these concentrations proved to be toxic to live sperm, so for the live sperm experiments, the lowest concentrations at which sperm were still clearly detectable using fluorescence excitation were used (Table 1, 'Live Sperm'). Care was taken to conduct all dye treatments, including the control (no dye), under identical experimental conditions, including subjecting all samples to gentle stirring with the micropipette tip for homogenisation and two aspirations before mounting on a slide.

Table 1: Summary table of organic dyes used for labelling efficacy and functional tests.

Dye name	Chemical name	Excitation wavelength	Emission wavelength	Concentration	
				Fixed Sperm	Live Sperm
(a) Membrane Dyes					
DiA (4-Di-16-ASP)	(4-(4-(Dihexadecylamino)styryl)-N-methylpyridinium iodide)	493 nm	510-690 nm	200 μM	-
Di10 (4-Di-10-ASP)	(4-(4-(Didecylamino)styryl)-N-methylpyridinium iodide)	492 nm	510-690 nm	200 μM	50 μM
FM 1-43	(N-(3-Triethylammoniumpropyl)-4-(4-(dibutylamino)styryl) pyridinium dibromide)	509 nm	510-690 nm	200 μM	-
R18 (Octadecyl Rhodamine Chloride B)	Xanthylium,3,6-bis(diethylamino)-9-[2-[(octadecyloxy)carbonyl]phenyl]-, chloride	556 nm	576 nm	30 μM	10 μM
(b) Nucleic acid dyes					
SYBR 14	Not Available	488 nm	516 nm	1 μM	0.10 μM
SYTO 13	Not Available	488 nm	509 nm	1 μM	0.20 μM
SYTO 82	Not Available	541 nm	560 nm	5 μM	0.25 μM

The two columns under 'concentration' refer to the two different concentrations used for the tests on fixed sperm and live sperm. DiA and FM1-43 were excluded from the experiments involving live sperm. All dyes were purchased from Molecular Probes Inc., UK.

Experiment 1: Labelling efficacy

In order to compare labelling efficacy of each dye treatment, semen from the distal end of the left SGs of males (n = 5) was squeezed into warm Ham's F10 Nutrient Mix (Gibco™). Sperm were allowed to "swim out" for 10 seconds and then 20 μL of the resulting cloud of swimming sperm was collected [see Bennison *et al*. (2015) electronic supplementary material] and fixed in 300 μL of 5% formalin. The fixed sperm were divided into 20 μL aliquots and each aliquot was incubated in a water bath at 37° C for 2 mins with one of the dyes listed in Table 1, using the concentrations listed in the 'Fixed Sperm' column. A control aliquot from each male (untreated) was also incubated. 10 μL of each treatment was mounted on a glass slide and examined at 200x magnification using a microscope (Leica DMBL with Infinity 3 camera, Luminera Corporation) with dark-field and fluorescence filters (detailed above).

A minimum of 200 sperm was counted for each treatment, including the control, from each male. In practice, 230 ± 3 (mean ± s.e.m.) sperm were counted, and each sperm was scored for labelling under fluorescence excitation. Preliminary trials showed that the DiA, Di10 and R18 dyes did not label zebra finch sperm uniformly, so across all treatments, each sperm was scored as 'completely labelled' when the entire sperm cell was labelled continuously (Figure 2, B-G) or 'partially labelled' when unlabelled gaps were visible along the cell (Figure 2, A). Each field of view scored under fluorescence excitation was then also examined under dark-field microscopy without fluorescence, and the total number of sperm was recounted to determine the number of unlabelled sperm in the sample.

Sperm counted above [n = 230 ± 3 (mean ± s.e.m.) sperm] were also scored as 'normal' or 'damaged' (under dark-field) with reference to their morphology, to assess the extent of dye-induced damage. Sperm were scored as 'damaged' if components were broken, deformed, or missing; when the mitochondrial helix was unwound; when the nucleus

was swollen; or when the sperm was covered in blebs or particulate aggregates (Figure 1). In general, sperm with aggregates tended to aggregate together. Immature sperm and sperm with developmental abnormalities, such as double tails and abnormally shaped heads (e.g. spear shaped heads), which were not induced by dye treatments, were excluded from analyses.

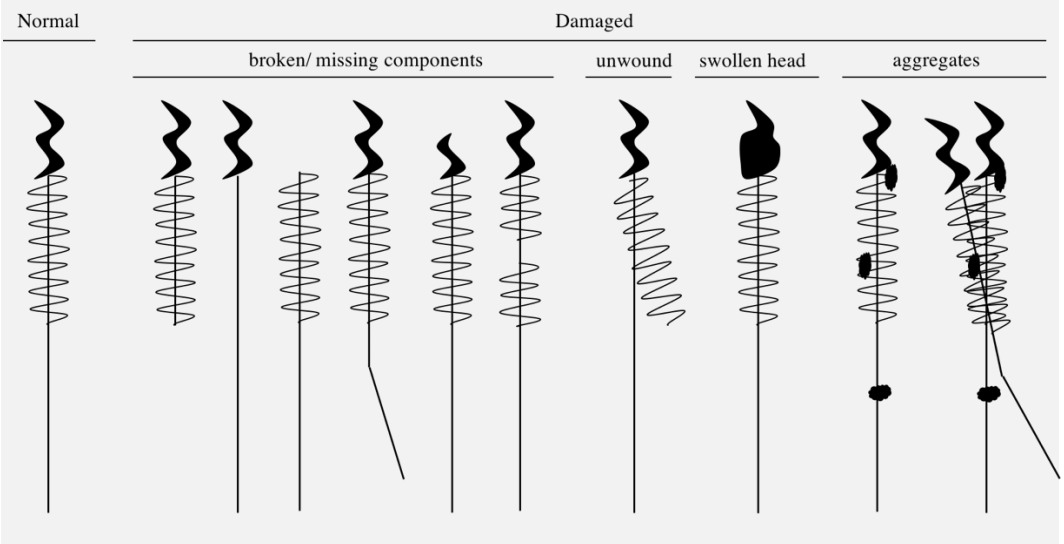

Figure 1: Diagrammatic representation of 'normal' and 'damaged' classifications of sperm. The blobs on sperm scored as 'aggregates' were aggregated dye molecules and/or membrane blebs. Adapted from Bennison (2014).

To quantify the background fluorescence from each treatment, three fields from each slide were captured at 100x magnification under fluorescence excitation using the I3 filter set for SYBR 14, SYTO 13, DiA, Di10 and FM 1-43, and the N2.1 filter set for SYTO 82 and R18. For the control treatment slides, images were taken under both filter sets to control for differences between the backgrounds with each filter. All images were taken under the same camera settings (500 ms exposure and an average intensity of 131 a.u.). For each captured field, the background fluorescence was quantified from three random background selections using the 'Mean Grey Intensities' measurement in Fiji (Schindelin *et al.*, 2012). This measurement gives the average fluorescence intensity

detected by the pixels on the camera sensor and encoded in the image file in the selected background region.

Experiment 2: Effect of dyes on sperm motility

This experiment assessed the performance of Di10, R18, SYBR 14, SYTO 13 and SYTO 82 on sperm motility. DiA and FM 1-43 were not included in the motility trials, since DiA produced a non-uniform pattern of labelling [see Results (Experiment 1) and Figure 2 (A)], and FM 1-43 produced unacceptably high levels of background fluorescence [see Results (Experiment 1) and Figure 2 (C)].

The experimental procedure allowed for a maximum of three treatments to be assessed at a time, so the experiment was performed in three parts with three replicates. Live semen samples were collected from males (n = 9) in warm Ham's F10 Nutrient Mix as described in Experiment 1. In the first trial, three 30 μL aliquots were taken from each male and treated with Di10, R18 and no dye respectively. Similarly, in the second trial, three 30 μL aliquots were treated with SYBR 14, SYTO 13 and no dye respectively. In the final trial, the three aliquots were treated with SYBR 14, SYTO 82 and no dye respectively. Preliminary trials showed that SYBR 14 had no effect on sperm motility [motility of top 10% fastest SYBR14 labelled sperm as compared to untreated sperm (n = 3 males): estimated effect = -0.048, z = -0.313, p = 0.947] and therefore, the other nucleic acid dyes were compared to SYBR 14 as well as to the control (no dye).

Following applications of the dyes, 4 μL aliquots of the sperm samples were loaded into 20 μm slide chamber (Leja®, Netherlands) and left to equilibrate for 30s on a heated stage at 37° C [Bennison *et al.* (2015) – electronic supplementary material]. Motility parameters were obtained by recording videos – each 500 ms long – of the sperm samples in the

Leja® slides immediately after each treatment using the Sperm Class Analyzer® [SCA] (Microptic, Barcelona, Spain) with a Basler acA780-75gc camera connected to an Olympus BX41 microscope as described in Bennison *et al.* (2015 – electronic supplementary material). Sperm have been shown to reach the SSTs within 30 mins and the infundibulum within 60 mins of insemination in domestic fowl (Saeki *et al.*, 1963) and turkeys (Howarth, 1971; Wishart, 1986). Relevant observations while tracking sperm progress in the female tract are therefore expected to occur within a 30 – 60 min time window from the time of insemination. The effect of the dyes on sperm motility was therefore assessed at 30 min intervals up to 90 mins after treatment. Each 500 ms video clip of sperm was captured using pseudo negative phase at x200 magnification. An average of 200 (± 30) sperm was recorded for each treatment from each male. There was a maximum of 10 mins between the first and last video clip recording at each time interval. In between the four 30 min time intervals the sperm samples were maintained at 37° C in a water bath.

SCA provided three kinematic parameters for each sperm: (i) average path velocity (VAP), (ii) curvilinear velocity (VCL), and (iii) straight line velocity (VSL) among others, as well as a motility score of either slow progressive, medium progressive, rapid progressive or static for each sperm. The slow progressive, medium progressive and rapid progressive sperm counts were summed to give the total number of motile sperm, regardless of velocity, for each sample. Debris, immature sperm and abnormal sperm such as those with two tails and abnormally shaped heads were excluded, but sperm deemed 'damaged' as detailed in Experiment 1 methods (above), including those with swollen nuclei, were included, since damage was likely to be dye-induced. Dead and/or drifting sperm were manually classified as static.

Experiment 3: Sperm–female interactions

The final experiment assessed the effect of dye treatments on the entry of sperm into SSTs in female zebra finches. Di10 was not included in this experiment due to the high tendency of this dye to cause sperm to aggregate, leading to a significant reduction in their motility [see Results (Experiment 2)]. R18 was therefore the only membrane dye that was assessed for its effect on sperm-female interactions, alongside the nucleic acid dyes SYBR 14, SYTO 13 and SYTO 82.

The experimental procedure allowed only two treatments to be tested at a time and so, the trials were split into four paired comparisons with three replicates for each. Live semen samples were collected from males (n = 12) as in Experiment 2. In the first trial, the likelihood of SYBR 14-treated sperm being accepted into SSTs for storage was compared to that of untreated sperm. The results from this first trial [see Results (Experiment 3)] showed that there was no effect of SYBR 14 on the number of SSTs filled, so the three other trials compared filling of SSTs with sperm treated with (1) SYTO 13, (2) SYTO 82, and (3) R18, to sperm treated with SYBR 14. This helped compare the performance of each dye to SYBR 14 (considering SYBR 14 treatment was equivalent to control).

For each of the paired comparisons listed above, the oviduct of a female zebra finch in breeding condition was removed by dissection and the utero-vaginal junction (UVJ), where the SSTs are located, was isolated. The UVJ was cut longitudinally to open the tract, and the region with the SSTs was removed, cut into two equal pieces and each piece was pinned into a petri dish filled with silicone elastomer (SYLGARD® 184; Dow Corning). A sufficient quantity of Ham's F10 Nutrient Mix was added to keep the tissue moist but not submerged (to avoid grossly diluting the sperm). The petri dish was placed on a heated mat set to 37° C throughout the experiment. Under these conditions, cilia on the epithelial surface of the female tract tissue could be observed beating under the microscope

at 60 mins post dissection, indicating that the UVJ tissue remained alive and functioning throughout the experiment.

50 μL of live sperm labelled with SYBR 14 was dispensed at the surface of one of the two pieces of the UVJ. The second piece was similarly treated with 50 μL of live sperm that was either left unlabelled or labelled with R18, SYTO 13 or SYTO 82. Each UVJ piece was incubated with live sperm for 15 mins before a randomly selected fold of epithelial tissue was dissected from the UVJ, laid flat on a glass microscope slide with a cover-slip placed on top, and imaged at 400x magnification under a microscope (Leica DMBL with Infinity 3 camera, Luminera Corporation) capable of bright field and fluorescence imaging. All the SSTs in each fold were scored as either empty or containing sperm. An additional two folds were isolated from the same UVJ piece at 30 min intervals and the same procedure was carried out to determine the effect of time on SST filling.

3.3. Data Analysis

The data analysis was performed using R version 3.2.3 (R Development Core Team, 2015). To assess the labelling efficacy of dyes, the effect of each dye on the proportion of labelled sperm was assessed via a linear mixed effects model with a binomial distribution. A dependent variable was constructed to include a vector of 'successes' (completely labelled sperm) and one of 'failures' (sum of partially labelled and unlabelled sperm).

To analyse the extent of dye-induced damage, a similar model was used with the number of damaged sperm (failures) and the number of normal sperm (successes) bound as the dependent variable. All three models included the dye treatments as fixed effects and bird ID as a random effect to account for repeated measures of sperm from each male. To compensate for the over-dispersed data, the models were fitted with quasi-binomial distributions using the 'glmmPQL' function from the

{MASS} library (Venables and Ripley, 2002). Tukey's pairwise comparisons were run post-hoc on the models to compare the performance of each dye treatment to the others using the {multcomp} package (Hothorn *et al.*, 2008).

Averages of the background intensities from images taken of each dye treatment were computed for each male and the difference of these average intensities from the corresponding average background intensities of control samples was determined for each treatment day and fluorescence filter set. A Tukey's pair-wise comparison of these intensity difference values was performed using the {multcomp} package (Hothorn *et al.*, 2008).

To compare the effect of the dye treatments on the proportion of motile sperm, a mixed effects model was fitted with a quasi-binomial distribution using the 'glmmPQL' function (Venables and Ripley, 2002). Here the dependent variable was defined by two vectors: (1) number of motile sperm (successes) and (2) the number of static sperm (failures). Dye treatment was included as a fixed effect and bird ID as a random effect. The time interval at which the motility counts were recorded was initially added as a fixed effect with an interaction term between time interval and dye treatment, but the interaction term was not significant and was therefore removed leaving only the fixed effect in the final model. A Tukey's pair-wise comparison was undertaken to compare the effects of each treatment. Data from each of the three trial groups [see Methods (Experiment 2)] was analysed separately.

VAP, VCL and VSL values obtained from the Sperm Class Analyzer® (Microptic, Barcelona, Spain), were highly correlated, which is typical for zebra finch sperm motility (Mossman *et al.*, 2009; Bennison *et al.*, 2015). A principal components analysis was therefore used to obtain a single index of sperm swimming velocity (PC1) for each sperm as described in Bennison *et al.* (2015). To account for the fact that the large variation in swimming velocity across each male's sperm could potentially mask any

effects of the dyes, the fastest 10% sperm from each male were also considered [as suggested by Bennison *et al.* (2015)] along with analysis at the single cell level including the entire sperm population. The PC1 values (for all sperm) and 10% highest PC1 values were fitted separately to a linear mixed model using the 'lmer' function from the {lme4} (Bates *et al.*, 2014) and {lmerTest} (Kuznetsova *et al.*, 2016) packages, with dye treatment as a fixed effect and bird ID as a random effect. Time interval at which readings were taken was included as a fixed effect with an interaction term with dye treatment. Again, data was analysed separately for the three trial groups [see Methods (Experiment 2)] and post-hoc Tukey's pair-wise comparisons were performed for each.

The effect of dye treatments on sperm acceptance into storage sites was assessed by fitting a linear mixed effects model with a binomial distribution using the {lme4} package (Bates *et al.*, 2014). As with the models above, the dependent variable was defined by two vectors – one for successes (count of filled SSTs) and one for failures (count of empty SSTs). Dye treatment was included as a fixed effect and female ID as a random effect. The time intervals at which the counts were conducted and the interaction between time and dye treatment were initially included as a fixed effect with an interaction term with dye treatment, and then as fixed effects. These were removed from the final model after neither was found to have a significant effect. Data from each of the four paired comparisons was analysed separately.

3.4. Results

Experiment 1: Labelling efficacy

The majority of the dye treatments tested showed high levels of labelling efficacy on formalin-fixed sperm cells. Di10, FM 1-43, R18 and SYTO 82 performed notably well (>97% sperm completely labelled, Table 2) and did not differ significantly from each other in their labelling efficacy. DiA

labelled a significantly smaller proportion of sperm than these four dyes but performed better than SYTO 13 (SYTO 13 – DiA; estimated effect = -1.164, z = -3.224, p = 0.018). There was no significant difference in the labelling efficacy of DiA and SYBR 14 (SYBR 14 – DiA; estimated effect = -0.407, z = -1.043, p = 0.951). SYBR 14 and SYTO 13 treatments showed the lowest proportions (72.05% and 83.28%, respectively) of completely labelled sperm (Table 2) and were comparable in their performance (SYTO 13 – SYBR 14; estimated effect = -0.758, z = -2.201, p = 0.271).

Despite their overall labelling efficacy, DiA, Di10 and R18 dyes show a non-uniform labelling pattern in zebra finch sperm at most concentrations. At optimal labelling concentrations (selected for the labelling efficacy experiment) levels of partially labelled cells were negligible in Di10 and R18, but comparatively higher in DiA (Table 2).

FM 1-43 showed significantly higher levels of background fluorescence than all the other treatments (Table 2). DiA, Di10, R18, and SYTO 82 treatments also had significantly higher background intensities than the control samples. SYBR 14 and SYTO 13 showed the lowest levels of background fluorescence, and were comparable to the control samples (Table 2).

Table 2: Summary of results for staining efficacy tests on formalin fixed sperm (n=5 males). [% values per male]

Dye Treatment	Labelling type	Colour	Concentration (μM)	Percentage of sperm completely labelled (%)[1]	Percentage of sperm partially labelled (%)[1]	Background fluorescence intensity [Treatment – Control] (a.u.; mean ± SD)	Percentage of damaged sperm (%)[1]
Control (no dye)	NA	NA	NA	0.00±0.00	0.00±0.00	0.00±0.00	9.69±5.41
DiA	Membrane dye	Green	200	**88.28±0.06**	**8.40±5.85**	**5.49±2.58**	**39.74±13.79**
Di10	Membrane dye	Green	200	98.78±0.02	0.08±0.18	**7.05±2.03**	**40.86±10.95**
FM 1-43	Membrane dye	Green	200	99.43±0.01	0.00±0.00	**21.66±2.14**	9.42±6.00
R18	Membrane dye	Red	30	99.46±0.01	0.37±0.63	**8.45±3.27**	11.82±5.13
SYBR 14	Nucleic acid dye	Green	1	**83.28±0.18**	0.00±0.00[2]	0.88±2.57	9.94±5.09
SYTO 13	Nucleic acid dye	Green	1	**72.05±0.31**	0.00±0.00[2]	1.16±1.36	9.52±4.40
SYTO 82	Nucleic acid dye	Red	5	97.91±0.02	0.00±0.00[2]	**3.48±2.32**	7.44±3.69

The values in red highlight the worst performing dye treatments in each column category and the values in bold imply significant differences from the control treatment.

[1]n = 5 males, 230 ± 3 sperm from each male (mean ± s.e.m.)

[2]Nucleic acid dyes label only the nucleus and so partial labelling would refer to unlabelled gaps in the nucleus.

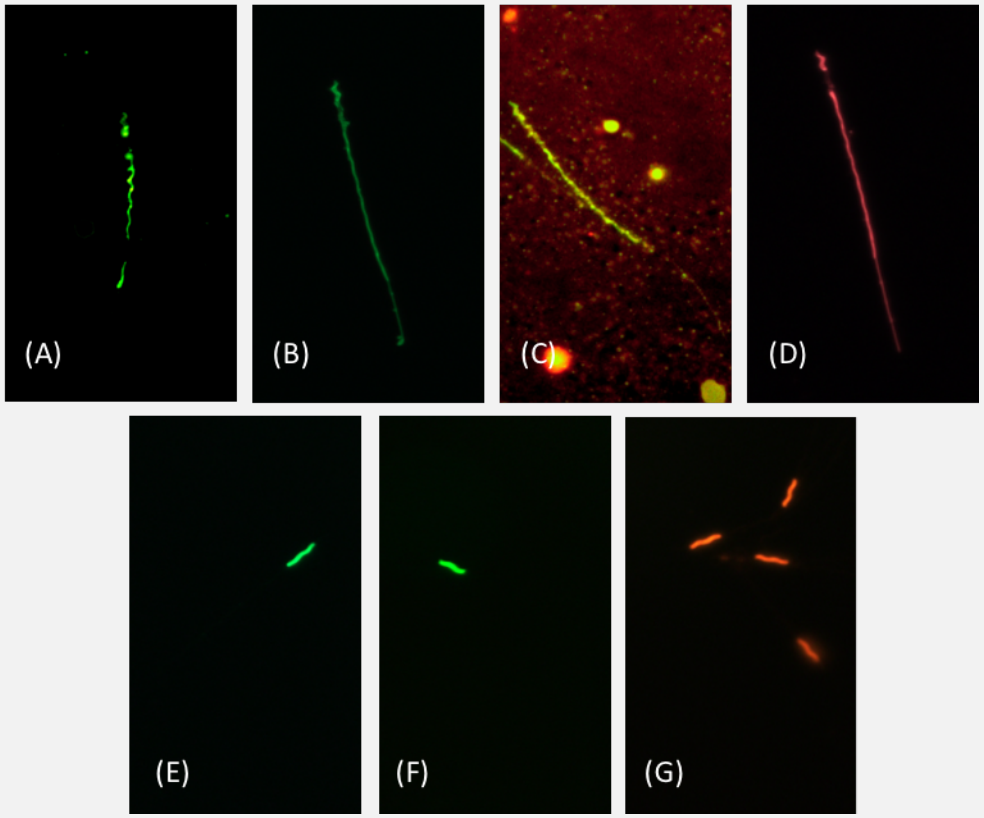

Figure 2: From left to right – sperm labelled with (A) DiA, (B) Di10, (C) FM 1-43, (D) R18, (E) SYBR 14, (F) SYTO 13 and (G) SYTO 82 at concentrations listed in the 'Fixed Sperm' column in Table 2. DiA shows a pronounced non-uniform labelling pattern while FM 1-43 shows significant background fluorescence.

Only DiA and Di10 treated samples showed notably larger proportions of damaged sperm than control samples. When labelled with these two dyes, sperm also appeared to aggregate with each other (as seen in the fixed samples). There was no significant difference between the effect of Di10 and DiA on the proportion of damaged cells (Figure 3).

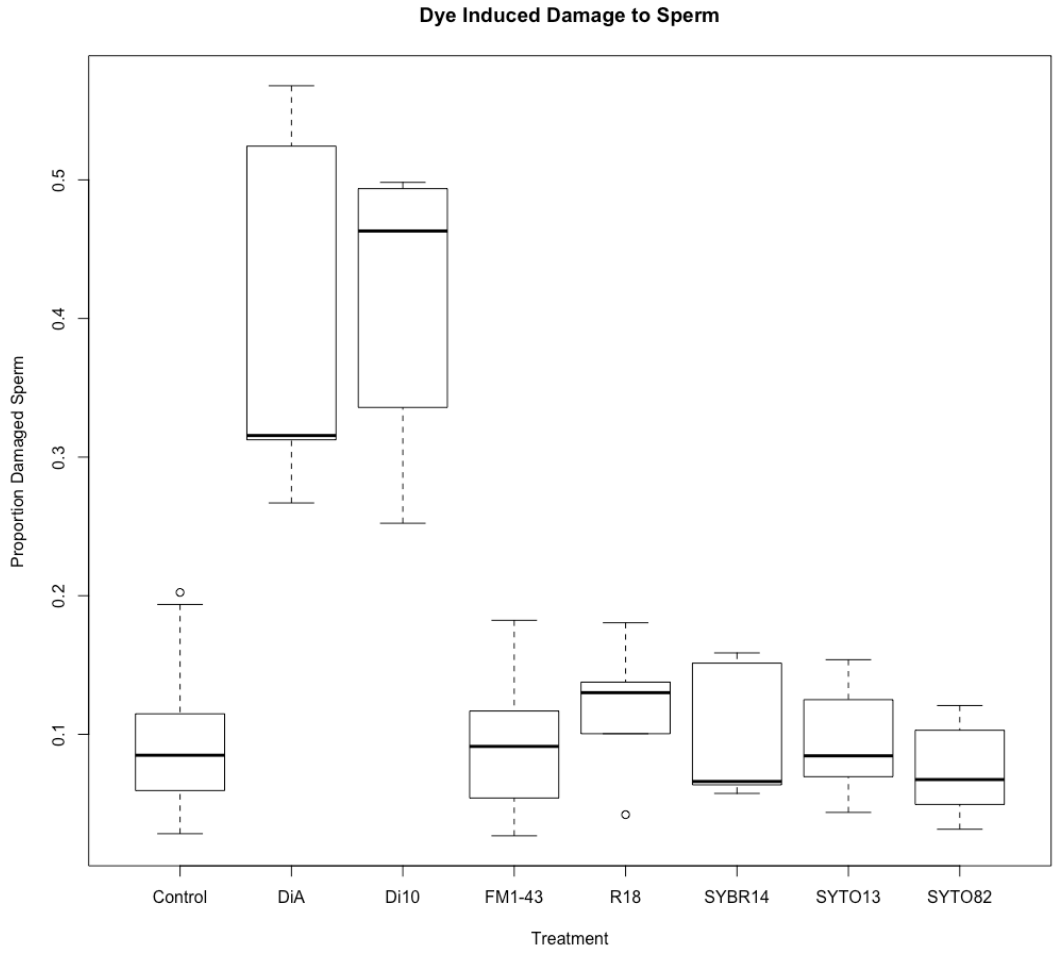

Figure 3: Proportion of damaged sperm in treatment and control samples (n = 5 males). The concentrations used for each dye are listed in the 'Fixed Sperm' column in Table 1. The bold horizontal line in each box plot represents the median diameter for the slice, whiskers represent the range of variation in data and points represent outliers.

Experiment 2: Effect of dyes on sperm motility

Di10, R18, SYBR 14, SYTO 13 and SYTO 82 were tested for their effect on sperm motility. DiA and FM 1-43 were not tested because DiA produced a non-uniform pattern of labelling and FM 1-43 produced unacceptably high levels of background fluorescence (see previous section). R18 had no significant effect on the number of motile sperm or the velocity of swimming sperm. Di10 and SYTO 82 had significant negative effects on the average velocity of sperm (top 10% and entire sperm population, Table 3), but neither of these dyes influenced the proportion of motile

sperm. SYBR 14 showed a small negative effect on sperm swimming velocity (top 10% fastest sperm: estimated effect = -0.266, t = -2.582, p = 0.010; n = 6 birds) but this result was found to be driven by the data from one of the birds. When data from the anomalous trial were excluded, there was no longer a significant effect of SYBR 14 on sperm swimming velocity (Table 3). Sperm from the same bird were also used to test the effect of SYTO 82 but excluding this data did not change the results obtained. SYTO 13 treatment depressed the average swimming velocity of sperm, but surprisingly, appeared to increase the proportion of motile sperm (Table 3). A post-hoc analysis of the effects of the dyes on additional motility parameters (obtained from SCA) showed that SYTO 13 treated sperm had unusual swimming trajectories with higher amplitude of lateral head displacement (ALH) values (top 10% fastest sperm: estimated effect = 0.154, z = 6.041, p = <0.0001) and lower beat cross frequency (BCF) values (top 10% fastest sperm: estimated effect = -6.022, z = -15.030, p = <0.0001) as compared to control samples. We can therefore infer that SYTO 13 hinders normal sperm motility.

Table 3: Summary table of dye effects on sperm motility as compared to control samples

Dye Treatment	Concentration (μM)	Proportion of motile sperm – test statistic		Velocity of Fastest 10% sperm – test statistic		Velocity of entire sperm population – test statistic	
		estimated effect	*p*	estimated effect	*p*	estimated effect	*p*
Di10[1]	50	-0.072	0.934	**-1.826**	**<0.0001**	**-1.628**	**<0.0001**
R18[1]	10	0.205	0.573	0.109	0.696	-0.035	0.935
SYBR 14[2]	0.1	-0.189	0.105	-0.176	0.083	-0.161	0.0635
SYTO 13[1]	0.2	**0.590**	**<0.001**	**-3.822**	**<0.0001**	**-2.669**	**<0.0001**
SYTO 82[1]	0.25	0.113	0.616	**-1.717**	**<0.0001**	**-1.281**	**<0.0001**

Values in bold are significant as compared to the control and values in red denote significant undesirable effects. [[1]n = 3 birds, [2]n = 5 birds]

The effect of the dye treatments on sperm swimming velocity varied with time, such that with the exception of R18, any effects of the dyes on sperm velocity were manifested immediately, and then remained stable until a certain period of time, after which further impact of the dyes was observed [at 30 min interval for SYTO 82 (top 10% fastest sperm: estimated effect = -0.882, t = -5.211, p = <0.0001) and R18 (top 10% fastest sperm: estimated effect = -0.878, t = -4.454, p = <0.0001); 60 min for SYTO 13 (top 10% fastest sperm: estimated effect = 0.627, t = 2.351, p = 0.019), SYTO 82 (top 10% fastest sperm: estimated effect = -0.979, t = -5.634, p = <0.0001) and Di10 (top 10% fastest sperm: estimated effect = 0.505, t = 2.313, p = 0.021)]. Control samples only showed significant reduction in velocity at 90 mins. Additionally, for all treatment conditions including controls, the proportion of motile sperm at the 30 min interval was not

significantly different from that immediately after treatment, but dropped significantly at 60 mins and 90 mins post treatment (Figure 4). This suggests that, except in the case of R18 and SYTO 82, there is a 30 min window from the time of dye treatment where sperm motility is relatively consistent.

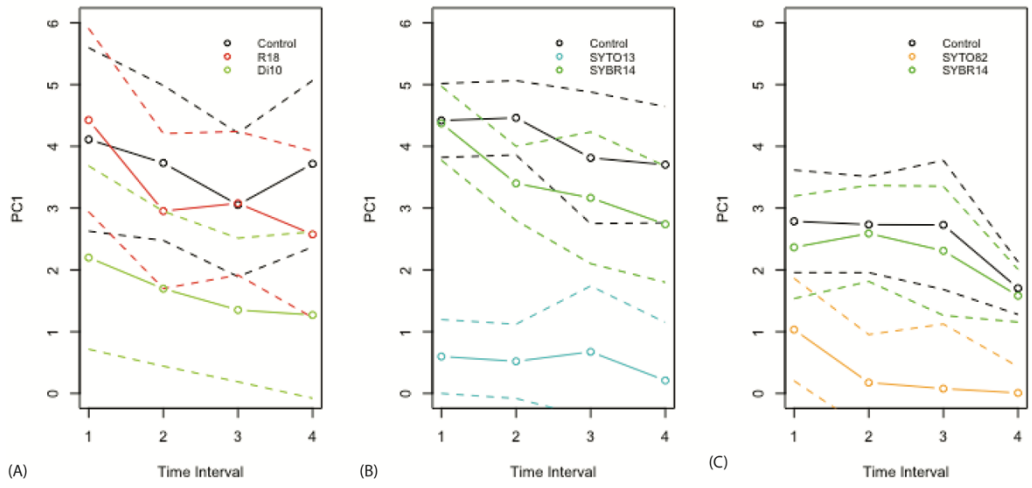

Figure 4: (A)-(C) PC1 values of fastest 10% sperm at 30 min time intervals starting at 0 mins from treatment. PC1 values are parameterised from VCL, VSL and VAP values obtained from the SCA software. The dashed lines represent the standard deviation from the mean velocity values. Data represents the three trials undertaken with three replicates (n = 9)

Experiment 3: Effect on sperm-female interactions

None of the four dye treatments tested (R18, SYBR 14, SYTO 13 and SYTO 82; Di10 was not included in this experiment due its high tendency to cause sperm aggregation and reduce motility) were completely prohibitive to sperm entry into the SSTs (Figure 5). There was no significant difference in the proportion of SSTs filled by SYBR 14 treated sperm compared to control sperm, or in the proportion filled by SYTO 13 treated sperm compared to SYBR 14 treated sperm. A significantly lower proportion of SSTs were filled by R18 treated sperm compared to SYBR 14 treated sperm, while a slightly higher proportion of SSTs were filled by SYTO 82 treated sperm compared to SYBR 14 treated sperm, an effect that was marginally significant (Table 4). Since SYBR 14 is comparable to the control, we can infer that R18 has a negative effect on sperm entrance into the SSTs, SYTO 13 has no significant effect and SYTO 82 has a slight positive effect. There was no difference in the proportion of filled SSTs across the three folds in each trial (the first dissected 15 mins after incubation and the second and third folds dissected at 30 min intervals thereafter), indicating that the majority of sperm entry into SSTs occurred within the first 15 mins of being in the vicinity of the female tissue.

Table 4: The effects of dye treatments on sperm entry into SSTs

Treatment	Proportion of SSTs with treated sperm	
	estimated effect	***p***
SYBR 14 (compared to control)	0.478	0.094
R18 (compared to SYBR 14)	**-0.745**	**0.003**
SYTO 13 (compared to SYBR 14)	-0.213	0.33
SYTO 82 (compared to SYBR 14)	**0.476**	**0.048**

The test was carried out in four parts with three replicates. Values in bold are significant as compared to the control and values in red denote significant undesirable effects.

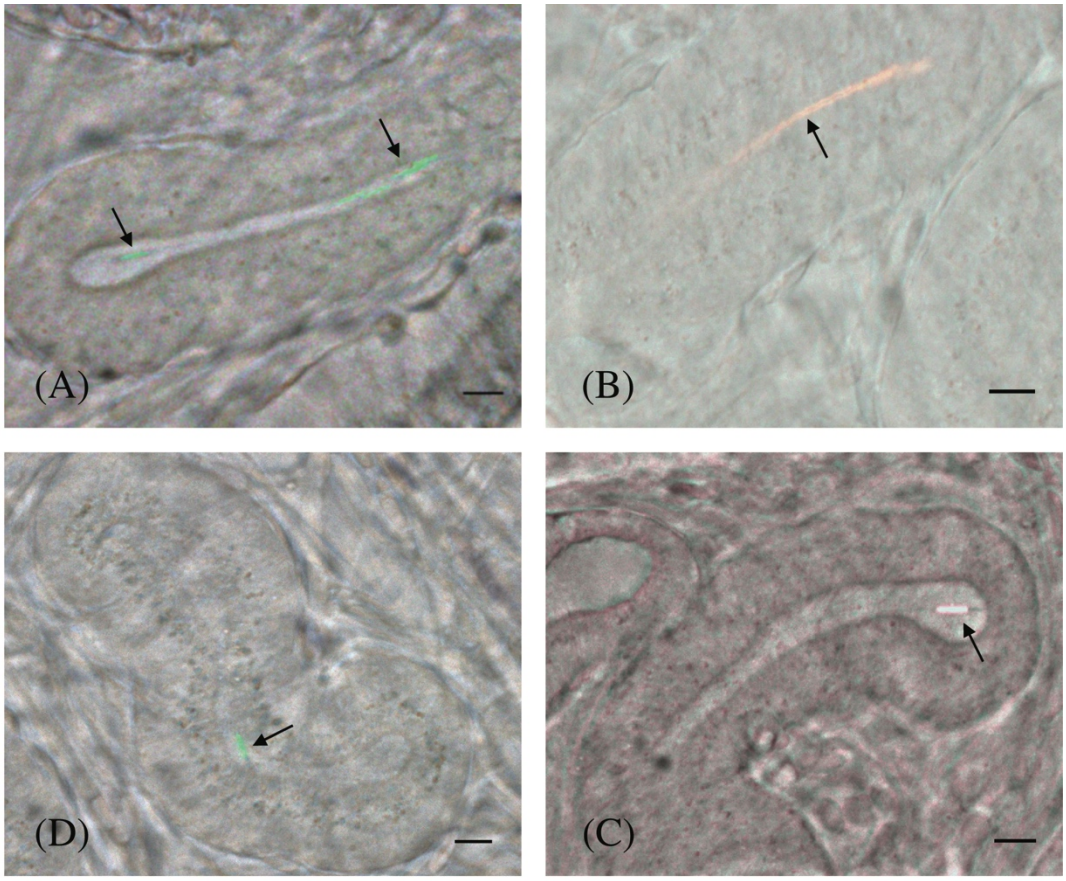

Figure 5: Sperm storage tubules containing sperm treated with the following fluorescent dyes: (A) SYBR 14, (B) R18, (C) SYTO 82 and (D) SYTO 13. Arrows indicate labelled sperm and scale bars represent 10 μm.

3.5. Discussion

In this study, I compared the suitability of seven commercially available organic dyes for labelling live zebra finch sperm for use *in vivo*. I tested the effects of the dyes on sperm structural integrity, motility, and interactions with the female reproductive tract. All seven dyes proved capable of labelling sperm, but most had at least some impact on sperm function.

Of the seven dyes tested, DiA performed the worst overall. Both DiA and Di10 are lipophilic dialkyl aminostyryl dye analogues that label cells by inserting into and diffusing laterally along the plasma membrane

(Spence and Johnson, 2010a). The results suggest this labelling process occurs non-uniformly in zebra finch sperm (Figure 2). Such non-uniform labelling has not been reported before, but these dyes have primarily been used on neuronal cells, in which labelling requirements may differ. Partial labelling can be overcome by increasing the concentration of dye used, but this did not prevent partial labelling with DiA in this study. At the high labelling concentrations selected from preliminary trials a significant proportion of sperm were labelled non-uniformly with DiA. Moreover, at high concentrations dialkyl aminostyryl dyes show a tendency to aggregate in solution and at the cell surface (Waggoner, 1979; Loew and Simpson, 1981), which could potentially explain why there was an increased incidence of sperm damage, characterised by a 'clumpy' appearance with membrane blebs or particulate aggregates on the surface of sperm. We can therefore conclude that DiA is not a good candidate dye for *in vivo* labelling of live sperm.

Despite its similar molecular structure, Di10 showed fewer instances of partial labelling at lower concentrations. However, due to its significant negative impact on average sperm velocity, and the high levels of damage it inflicted on sperm due to particulate aggregates, Di10 should also be considered unsuitable for labelling live sperm.

FM 1-43 is another dialkyl aminostyryl membrane dye that has a chemical structure that is similar to DiA and Di10. It performed well in terms of labelling efficacy but showed inhibitory levels of background fluorescence confirming reports by Pyle *et al.* (1999) and Gaffield and Betz (2007). These previous reports suggested adding a fluorescent quencher such as sulforhodamine to overcome background fluorescence, but this would increase the chemical load on the sperm cells and may impact sperm structure and function. Although this dye must therefore be considered unsuitable for labelling zebra finch sperm, it could potentially be valuable for labelling larger cells, tissues samples or even sperm from other species that can tolerate centrifugation and extensive washing to remove unbound dye particles from the samples [such as

boar sperm at high g-force and short centrifugation duration (Carvajal *et al.*, 2004)].

The cyanine dye R18 performed the best out of all the membrane dyes tested. R18 showed high labelling efficacy, no significant effect on morphological damage, and did not significantly alter the swimming velocity of sperm. It did, however, impede sperm acceptance into SSTs, making it unsuitable for studying sperm-female interactions *in vivo*. Why R18 reduced sperm acceptance into SSTs remains unknown, especially since it does not have any significant effect on sperm motility. It is possible that sperm membrane labelling interferes with female mediated sperm selection, which may be based on sperm membrane protein recognition (Cho *et al.*, 1998; Shen *et al.*, 2013; Holt and Fazeli, 2015) and/or sperm membrane charge (Holt and Fazeli, 2015).

In general, the three nucleic acid dyes performed better across most of the functional trials suggesting that nucleic acid dyes may be better suited to live sperm labelling than membrane dyes. SYTO 13 had an unexpected effect on sperm motility; despite an overall increase in the percentage of motile sperm, swimming velocity was significantly slower than the controls and sperm showed unusual beat patterns with larger amplitude (ALH) and lower frequency (BCF) values. The reason for this is unclear, and unfortunately the chemical structure of the SYTO 13 dye is proprietary of the manufacturing company (Molecular Probes Inc., UK), limiting our ability to further explore the biochemical nature of the dye's effect on sperm swimming velocity. Despite the hindrance to normal sperm motility, SYTO 13 treatment did not have any significant effect on sperm entry into SSTs. Importantly, this (along with the results for the other dye treatments from Experiments 2 and 3) suggests that sperm entry into SSTs does not depend on motility, which has important implications for our understanding of sperm transport into storage.

SYTO 13, along with SYTO 82 and SYBR 14, belong to the SYTO family of cyanine dyes. These dyes intercalate into DNA and RNA and this type

of labelling can involve relatively low affinity binding (Life Technologies Corporation, 2010). SYTO dyes also tend to photobleach under laser illumination (Wlodkowic *et al.*, 2008). These two issues may explain the relatively high proportions of unlabelled sperm observed for the SYTO 13 and SYBR 14 treatments. SYTO 13 along with SYBR 14 showed no background fluorescence and did not inflict any structural damage to labelled sperm. The different SYTO dyes differ from each other in characteristics including cell permeability and binding affinity (Wlodkowic *et al.*, 2009)[also see SYTO Orange product information - Molecular Probes], which could explain why we found a significant difference in the labelling efficacy of SYTO 82 compared to SYTO 13 and SYBR 14.

In contrast to SYTO 13, SYTO 82 did not affect the percentage of motile sperm in treated samples, which is consistent with the findings from the Martín-Coello *et al.* (2009) study, which reported that SYTO 82 had no effect on the proportion of motile sperm or on sperm-oocyte interactions in three murine species. However, our results indicate a negative effect of the dye on the average swimming velocity of labelled sperm; Martín-Coello *et al.* (2009) did not investigate effects on sperm velocity as part of their study. In our study, SYTO 82 also showed a surprising marginally positive effect on the entry of sperm into SSTs, although the reason for this is not clear. The nontoxic nature of SYTO 82, and its higher labelling efficacy compared to the other nucleic acid dyes tested, make it a more suitable nucleic acid dye for labelling live sperm for long-duration experiments.

Despite its tendency towards lower labelling efficacy than the other dyes tested, SYBR 14 generally outperformed most of the dyes tested. Although no significant effect of SYBR 14 dye treatment was found on sperm swimming velocity, these results should be treated with caution due to the small sample size and as one of the trials performed (which was subsequently excluded) drove the results to significance. The reason for this anomalous dye effect in one trial is not known. The results also

show that SYBR 14 does not inflict damage on sperm cells, reduce the percentage of motile sperm, or hinder female sperm storage in zebra finches. This is consistent with Garner's (1995) findings that SYBR 14 had no effect on fertilisation success and early embryonic development in boars [*Sus scrofa*]. Overall, SYBR 14, along with SYTO 82 appear to be potentially valuable for studying sperm across taxa.

In conclusion, the three dialkyl aminostyryl membrane dyes DiA, Di10 and FM1-43 were found to be unsuitable for labelling live zebra finch sperm, primarily due to poor labelling efficacy and structural damage to sperm cells. The cyanine membrane dye R18 appears to have potential for use in tracking and studying sperm behaviour, but is not ideal for investigating sperm-female interactions *in vivo* due to its negative effect on sperm acceptance into SSTs. In contrast to the membrane dyes, the three nucleic acid dyes had relatively benign effects on sperm structure and function, indicating that nucleic acid dyes may generally be better suited to live sperm labelling. SYTO 13 was found to be the least suitable of the three for *in vivo* sperm tracking, due to its unexpected effect on a range of sperm motility parameters. Despite a slight negative effect on sperm swimming velocity, the red nucleic acid dye SYTO 82 and the green nucleic acid dye SYBR 14 appeared to be the most suitable for tracking post copulatory sperm selection events *in vivo* and any experimental design would have to take the reduction in swimming velocity into account. SYBR 14 may be considered preferable for studying sperm-female interactions as it did not influence sperm entry into SSTs, while SYTO 82 had a currently inexplicable marginal positive effect suggesting it may alter normal sperm function. The use of SYBR 14 would be most effective when coupled with light sheet based imaging technology such as SPIM to overcome the photobleaching tendencies.

Since nucleic acid dyes perform more successfully than membrane dyes, a potential avenue for future development would be the synthesis of bespoke dyes that target nucleic acids, but also show irreversible bonding and superior photo-physical properties (lower propensity to

photobleaching) than the dyes investigated here. Identification of alternative target sites for fluorophores, other than the nucleus or sperm membrane, would also broaden the range of potential dyes that could be used for studying sperm behaviour *in vivo*.

Chapter 4.

Volumetric analysis of sperm: regulation of mid-piece size in zebra finch sperm

4.1. Introduction

Sperm morphology in internally fertilising species has evolved to be incredibly diverse, in response to strong selection within the female reproductive tract (Parker, 1970; Eberhard, 1996). In order to fertilise the ovum, sperm must travel through the challenging environment of the female tract, often competing with other sperm to reach the site of fertilisation. Morphological traits that confer enhanced swimming velocity and/or higher energetic capacity are therefore predicted to be favoured.

A number of studies in a range of taxa have demonstrated that species with high sperm competition intensity, due to high rates of female multiple mating, produce sperm that are longer [(Morrow and Gage, 2000; Kleven *et al.*, 2009; Lüpold *et al.*, 2009) but see (Stockley *et al.*, 1997; Gage and Freckleton, 2003)], faster (Fitzpatrick *et al.*, 2009; Kleven *et al.*, 2009; Lüpold *et al.*, 2009; Tourmente *et al.*, 2011), and have greater morphological uniformity (Calhim *et al.*, 2007; Immler *et al.*, 2008; Fitzpatrick and Baer, 2011; Varea-Sánchez *et al.*, 2014). Surprisingly however, the limited information that exists on sperm energetics suggests that there is no direct relationship between sperm competition

intensity and levels of adenosine triphosphate (ATP), a crucial nucleotide for energy metabolism within cells (Rowe *et al.*, 2013)[but see (Tourmente *et al.*, 2013)]. This is unexpected, because high sperm competition tends to select for sperm with longer flagella to provide greater propulsion (see above), and longer flagella would presumably require more ATP in order to function efficiently. In sperm, ATP is generated through oxidative phosphorylation (OXPHOS) in the mitochondria contained in the mid-piece. In some species, longer and faster sperm have longer mid-pieces (Firman and Simmons, 2010), but this is not always the case (Gage *et al.*, 2004; Malo *et al.*, 2006; Humphries *et al.*, 2008). Humphries *et al.* (2008) argued that relative lengths of sperm components, as opposed to absolute lengths, should have a greater effect on performance, as the contributions of individual sperm components to hydrodynamics – head to drag, flagellum to thrust, and mid-piece to generating energy towards thrust, interact in complex ways to influence sperm motility. It is therefore likely that relative lengths, rather than and not absolute lengths, will be the target of selection (Humphries *et al.*, 2008).

Passerine bird sperm possess the same major components as those from most other animal taxa – a head, mid-piece and flagellum. However, in most cases they display a complex helical shape, with an undulating membrane wound around a short head, and fused mitochondria wound around a long stretch of the flagellum to form the mid-piece (Humphreys, 1972; Vernon and Woolley, 1999). This helical shape further complicates the relationship between sperm form and function. In the zebra finch [*Taeniopygia guttata*], a model passerine species (Birkhead, 2010), sperm morphological traits are heritable (Birkhead *et al.*, 2005; Mossman *et al.*, 2009; Kim *et al.*, 2017; Knief *et al.*, 2017a), and mid-piece length is highly variable between males (Kim *et al.*, 2017; Knief *et al.*, 2017a). Sperm with a long flagellum and a mid-piece to tail length ratio approaching 1:1 swim fastest, but there is no obvious independent effect of mid-piece size on velocity (Bennison *et al.*, 2016). Overall, long sperm are more successful at reaching ova, but sperm length alone does not completely predict fertility success (Bennison *et al.*, 2015; Hemmings *et*

al., 2016)]. Recent work has shown that variation in sperm morphology and velocity is controlled by a supergene – a group of closely linked genes that are inherited together and allow for complex phenotypes (Thompson and Jiggins, 2014) – on the Z-chromosome, with heterozygotes producing sperm with long mid-pieces, long tails, and as a result, higher swimming velocity and fertilisation success (Kim *et al.*, 2017; Knief *et al.*, 2017a).

The link between sperm energetics, swimming velocity, and fertilisation success is not clearly understood in the zebra finch. Unexpectedly, sperm with the short mid-pieces have been shown to contain higher concentrations of stored ATP than sperm with long mid-pieces, and no link has been found between stored ATP levels and swimming velocity (Bennison *et al.*, 2016). It is possible that ATP production via OXPHOS in the mid-piece is supplemented or replaced by cytosolic glycolysis for energy production in passerine sperm, as appears to be the case in mammalian sperm (Storey and Kayne, 1975; Takei *et al.*, 2014). However, in the mammalian species studied, glycolytic enzymes have been reported to be bound to the fibrous sheath present along the principal piece of the flagellum (Storey and Kayne, 1975; Westhoff and Kamp, 1997; Krisfalusi *et al.*, 2006). Such a fibrous sheath is not present in passerine sperm (Jamieson, 2007). Moreover, OXPHOS has been shown to be a major energetic pathway for sperm of other bird species (Sexton, 1974; Froman and Feltmann, 1998; Froman *et al.*, 1999). Therefore, although we cannot discount the possibility that glycolysis plays a role in passerine sperm metabolism, current evidence suggests mitochondrial activity is likely to be of primary energetic importance.

Assuming mitochondrial activity is the primary source of energy for zebra finch sperm motility, the disparity between mid-piece length and stored ATP content may be interpreted in two ways: (1) length alone may not be an accurate measurement of overall mid-piece size (if, for example, volume is not proportional to length), and/or (2) the internal organisation of the fused mitochondria inside the mid-piece allows for

greater energetic efficiency in shorter mid-pieces. In mitochondria, the majority of the major complexes involved in oxidative phosphorylation (OXPHOS) metabolism (including 94% of the ATP synthase and complex III, and 85% of cytochrome-*c* (Gilkerson *et al.*, 2003)) are localised in membrane folds called cristae scattered among the mitochondrial matrix. Cristae density increases with energy demand (Mannella *et al.*, 2013) and is not fixed for a cell type (Nielsen *et al.*, 2017). Increased cristae density improves the flow of adenylates to metabolic sites, increasing ATP production (Demongeot *et al.*, 2007). This suggests that mitochondrial packing, along with overall mitochondrial volume, is important for mitochondrial activity.

A small number of mammalian studies have made volumetric measurements of sperm mid-piece (Gage, 1998; Anderson and Dixson, 2002; Gage and Freckleton, 2003), but this approach has not yet been extended to other taxa. Obtaining volumetric data from passerine sperm is particularly challenging, due to their helical shape (Jamieson, 2007). Here I overcome these challenges by employing novel three-dimensional imaging techniques to obtain volumetric data from zebra finch sperm cells, combined with transmission electron microscopy (TEM) to reveal sperm mid-piece structure. My aims were to (1) determine the relationship between sperm mid-piece volume and length in the zebra finch, and (2) assess whether mitochondrial organisation inside the mid-piece varies with mid-piece length.

4.2. Materials and Methods

The present study included two main parts. Firstly, I investigated the relationship between the volume of the sperm mitochondrial helix and mid-piece length in zebra finch sperm, using SPIM - a fast, high contrast, three-dimensional imaging technique (see Chapter 2), which allowed me to access volume and length along the mitochondrial helix directly from the volumetric data. Second, I examined the internal structure of zebra

finch sperm mitochondrial helix by analysing cross-sections imaged using a high resolution TEM microscope. The first part of the study involved the preliminary development of methods which have been described below in the section "Methods Development".

Methods Development

Prior to using our SPIM system to acquire volumetric data from single sperm cells, it was essential to ensure that the resolution limit of the system was suitable for this application. The resolution limit of our self-built SPIM system was defined in terms of its point spread function (PSF). A single view acquisition (single z-stack not subjected to deconvolution) with a light sheet thickness of 4.060 μm, gave PSF measurements of 0.825 μm in the lateral and 3.732 μm in the axial direction (see Chapter 2). Birkhead *et al.* (2005) reported that zebra finch sperm cells have a 3 μm cross-sectional radius (measured from the centre of the flagellum to the centre of the mitochondrial helix) and a variable flagellum length of 53.59 ± 5.11 μm (mean ± SD). Zebra finch sperm were therefore considered to be large enough to image with a diffraction-limited system such as SPIM.

Images of a sub-resolution object would appear distorted and extended in both the lateral and axial directions to fit the PSF profile. Preliminary single view acquisitions of zebra finch sperm showed an extended z-profile (Figure 1), indicating that, contrary to the report of Birkhead *et al.* (2005), these cells have a sub-resolution cross-sectional diameter (<4 μm) which is smaller than previously assumed. These images therefore proved to be inadequate for acquiring volumetric measurements from sperm cells.

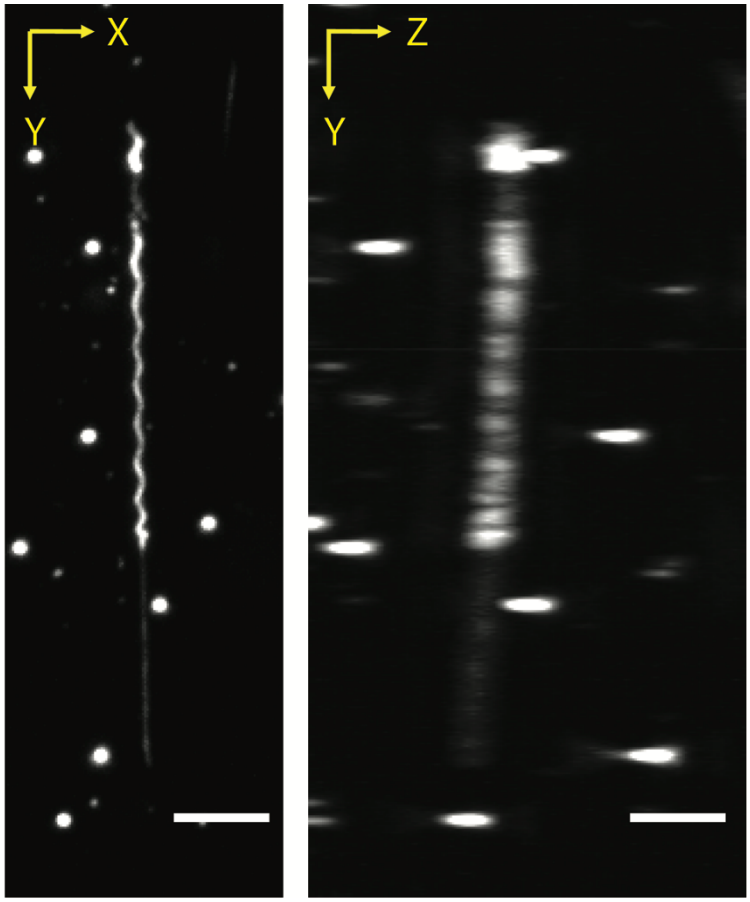

Figure 1: Sperm showing an extended profile in Z. The beads in the imaging volume are 1 μm fiducial markers. Scale bar – 10 μm

In order to overcome this issue, I attempted to enhance the resolution of the system in the axial direction by performing multi-view bead-based registration and deconvolution (Huisken *et al.*, 2004; Preibisch *et al.*, 2010). This involved acquiring multiple image z-stacks of the same sample region while rotating the sample between acquisitions. These multi-angle acquisitions are then aligned in 3D and deconvolved using the multi-view deconvolution plugin (Preibisch *et al.*, 2010) in Fiji (Schindelin *et al.*, 2012). After multi-view deconvolution, distortions and low quality information in each image volume are replaced by higher quality information from overlapping image volumes taken at different acquisition angles (Huisken *et al.*, 2004).

To measure the improvement in the system PSF after multi-view deconvolution, z-stacks of 200 nm Microspheres (λ_{ex}/ λ_{em}= 540/560, 2%

solids; Invitrogen™) suspended in 1% agarose (Sigma Aldrich) were acquired at 5 angles (0°, 72°, 144°, 216° and 288°) using laser excitation at 473 nm and a 525 nm (15) BP fluorescence emission filter (Semrock, Inc.). Upon performing multi-view registration and deconvolution, the full width at half maximum (FWHM) of the intensity profiles of individual microspheres were measured to obtain lateral and axial PSF values as detailed in Chapter 2. The resulting PSF from the deconvolved images showed notable improvement in the axial direction (PSF_{axial} = 1.220 μm) and to a smaller degree in the lateral direction ($PSF_{lateral}$ = 0.654 μm) as compared to the PSF from single view acquisitions (see Chapter 2 and Figure 2 below).

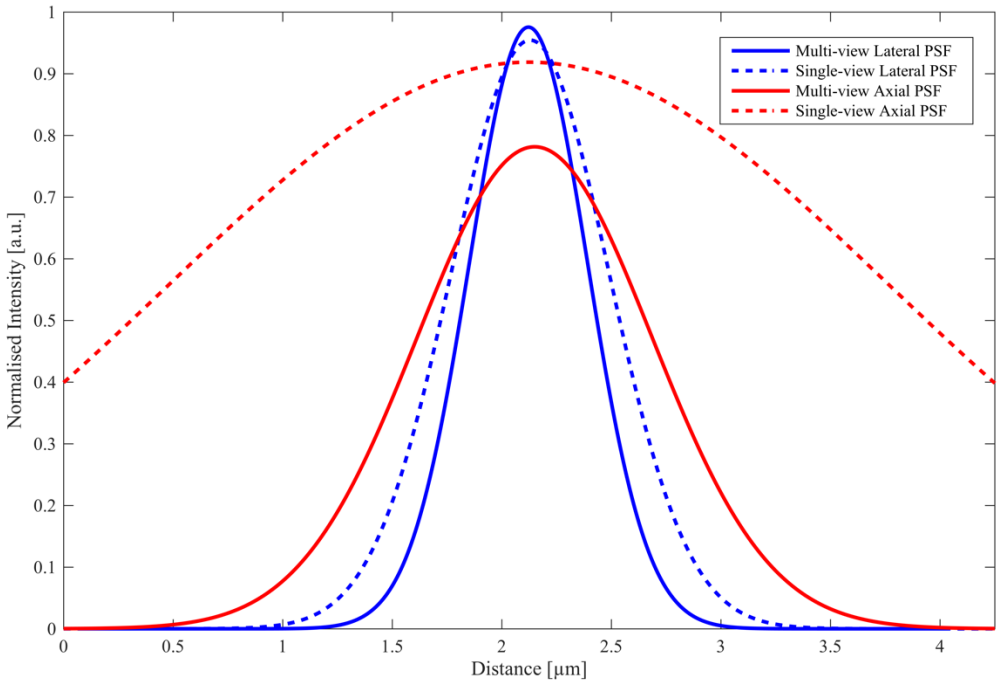

Figure 2: Multi-view deconvolution greatly improves the PSF of the SPIM system. Plots represent Gaussian fits to experimental data.

With the improved axial resolution, z-profile extension was no longer seen (Figure 3). The deconvolved images were used to extract three-dimensional volume and length measurements as detailed in the following sub-section.

Part 1: Volumetric study of mid-piece external morphology

Animals

For part 1, zebra finches were selected from a domesticated population at the University of Sheffield that had been subject to a selective breeding regime to increase numbers of males producing sperm at the extreme ends of the sperm length range for the species (Birkhead *et al.*, 2005; Bennison *et al.*, 2015). Sperm length data were obtained for males hatched in the year 2012 - 2013 by measuring sperm from faecal samples as described by Immler and Birkhead (2005). Males producing sperm with relatively long [37.209 ± 2.623 μm (mean ± SD); n = 10 males] and short mid-pieces [26.822 ± 4.447 μm (mean ± SD); n = 9 males] were compared. 10 males with short mid-pieces were initially selected but the sperm sample from one of these males showed a high proportion of damaged sperm and therefore, data from this individual was excluded.

The birds were housed in cages (dimensions: 1.2 x 0.5 x 0.4 m) in groups of 10, separated from groups of 10 females in identical cages behind a wire mesh as described in Chapter 3, Materials and Methods. Prior to sperm collection, males were humanely euthanized by cervical dislocation in accordance with Schedule 1 (Animals (Scientific Procedures) Act 1986) and dissected immediately. Semen was collected from the left seminal glomerus (SG) by squeezing the distal region into warm Ham's F10 Nutrient Mix (Life Technologies, UK) as described in Bennison *et al.* (2015, electronic supplement). 20 μL of motile sperm from the SG was collected and fixed in 300 μL of 5% formalin.

Instrumentation

Sperm mitochondrial helix volumes were computed from image z-stacks acquired using a self-built selective plane illumination microscope (SPIM) at the University of Sheffield (see Chapter 2 for a detailed description). Images were captured using a sCMOS camera (Orca Flash

4.0 V2 C11440-22CU, Hamamatsu Photonics) which was triggered by a piezo stage controller (E-725.3CD, Physik Instrumente Ltd) and files were written to disk using HCImageLive software (Hamamatsu Photonics).

Microscopy

10 μL aliquots of the fixed sperm samples were incubated with 500 μM Mitotracker Green FM (Molecular Probes, Eugene, OR), a mitochondria specific dye, for 10 mins. 10 μL of the stained sperm was mixed with blue-green fluorescent microbead fiducial markers (1 μm diameter, 1:800 dilution; Invitrogen™) and suspended in agarose (low gelling point, final dilution of 1%; Sigma Aldrich). The above mixture was aspirated into an OpenSPIM sample holder (Pitrone *et al.*, 2013) - a 1 mL syringe modified to hold a 20 μL capillary and plunger (Wiretrol® I, Drummond Scientific Company) - and left to set for 30 mins.

Agarose embedded samples were prepared for each male and 200 μm deep image stacks of each imaging volume were acquired at 5 angles (0º, 72º, 144º, 216º and 288º) in PBS using laser excitation at 473 nm and a 525 nm (15) BP fluorescence emission filter (Semrock, Inc.). Multi-view registration and deconvolution was then performed on these stacks using the 'multi-view deconvolution' (Preibisch *et al.*, 2010) plugin in Fiji (Schindelin *et al.*, 2012) to acquire a single deconvolved stack for each imaging volume.

Image processing

Region of interest (ROI) volumes were cropped around individual sperm in the deconvolved image stacks in Fiji (Schindelin *et al.*, 2012). Image data for sperm – five from eleven males, four sperm from seven males and three sperm from one male, after rejecting sperm that appeared damaged – were processed in this way and 3D length measurements of the mid-piece, flagellum and total length were acquired using the semi-

automated plugin 'Simple Neurite Tracer' (Longair *et al.*, 2011). This plugin traced the helical shape of the mid-piece and therefore, measured the length of the mitochondrial helix if it was unwound and straightened ('straight helix length'). The length of the mid-piece in its coiled state, along the flagellum, was computed by interpolating the straight helix length trace from the Simple Neurite Tracer plugin in each axis using the 'interp1' function in MATLAB® (2015b, version 8.6, The Math Works, Natick, MA) and will be referred to simply as 'mid-piece length' henceforth. Additionally, the number of gyres (helical turns) along each mid-piece was recorded. Immature and damaged sperm – with kinks, breaks or swellings (see Chapter 3, Figure 1 for a guide) - were excluded from the analysis.

The volume of the mitochondrial helix was computed in MATLAB from the sperm ROIs defined above. A selection was made around the mid-piece to isolate the image volume containing the labelled mitochondrial helix and this was then binarised using a threshold. The volume was computed by counting the thresholded pixels using the 'regionprops' function from the Image Processing Toolbox (Thompson and Shure, 1995) in MATLAB and scaling this value to match the microscope voxel ratio after multi-view deconvolution (0.234 x 0.234 x 0.234 μm). Mito-tracker is a mitochondria specific dye which stained the mitochondria more strongly than the flagellum in the sperm analysed. We therefore expect the isolated volumes to represent the mitochondrial helix although we cannot discount some inclusion of the flagellar portion of the mid-piece in the selections.

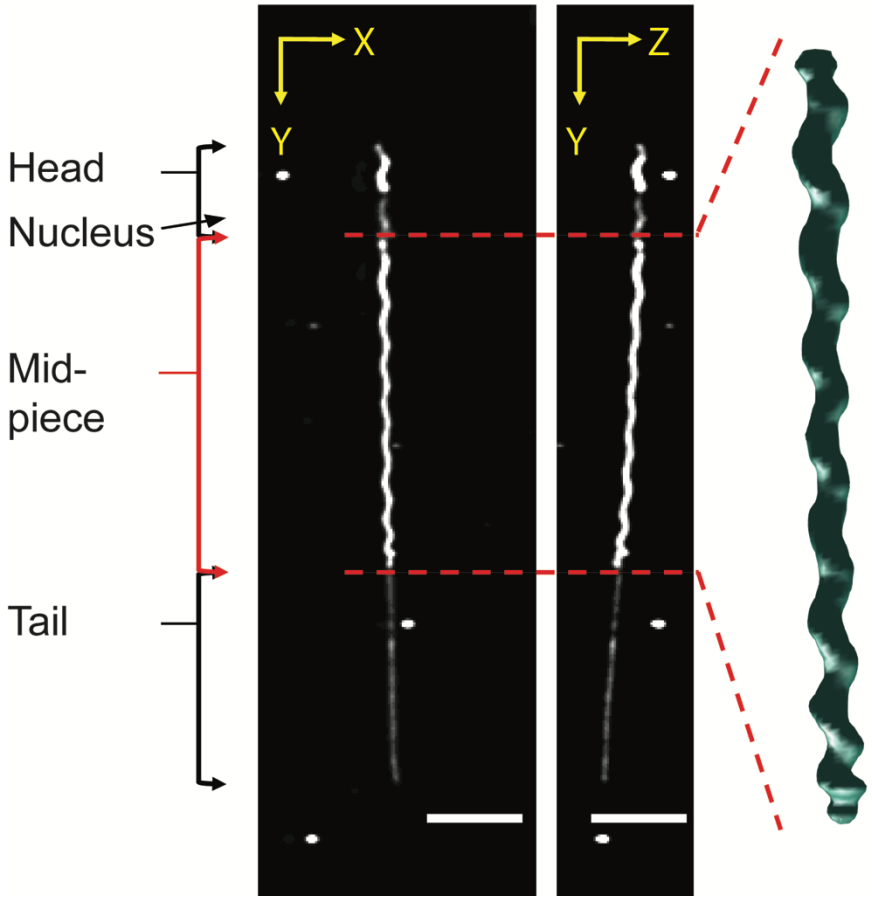

Figure 3: The mid-piece of the sperm was isolated from the deconvolved image z-stacks. Volumetric measures were extracted from the isolated mid-pieces and used to create 3D reconstructions of the sperm mid-piece (right image). The beads in the image volumes are 1 μm fiducial markers. Scale bar – 10 μm. Axes are indicated at top left of each image.

Part 2: Study of mid-piece internal organisation

Animals

For this study, we used zebra finches from the captive study population 'Bielefeld' kept at the Max Planck Institute for Ornithology in Seewiesen (Forstmeier *et al.*, 2007). The genomes of multiple generations of this zebra finch population have been mapped to identify the sperm-trait linked genotype for each individual (Knief *et al.*, 2017a, b). The homokaryotype AA has been shown to determine the production of sperm with the shortest mid-piece lengths, while the heterokaryotype AB

is associated with long mid-pieces (Kim *et al.*, 2017; Knief *et al.*, 2017a). Five zebra finch males with the AA genotype and five with the AB genotype were selected for use. The birds were humanely euthanized by cervical dislocation and dissected immediately. The left SG of each male was immediately removed, cleared of connective tissue and the distal 3 - 4 mm of the SG was unravelled. A 10 μL sample of sperm was collected in phosphate buffered saline (PBS; Sigma Aldrich) as described in part one. This sperm sample was fixed in 200 μL of 5% formalin and used to measure the lengths of the sperm components. The rest of the SG was fixed for TEM imaging by incubating in a glass vial with standard fixative solution [glutaraldehyde (Sigma Aldrich), formaldehyde EM grade (Science Services) and sodium phosphate buffer ($Na_2HPO_4.2H_2O$ and $NaH_2PO_4.2H_2O$, Sigma Aldrich), pH 7.5] at room temperature for 2 hours with gentle agitation (100 rpm). After 2 hours, the glass vials with the SGs were transferred to a fridge at 4° C for 1 - 2 days. At the end of fixation, the SGs were transferred into micro-centrifuge tubes containing cold sodium phosphate buffer at 4° C for transport to the University of York for further processing and TEM imaging.

Microscopy

The fixed SGs from 10 males were embedded in resin blocks and 600 nm sections were cut for TEM imaging. These sections were negatively stained with uranyl acetate and lead citrate before being imaged using a Tecnai 12 TEM (FEI, OR) at 43000X.

Since sperm were sliced to obtain transverse sections, mid-piece lengths were not obtainable from the TEM images. Sperm traits are highly repeatable within male zebra finches (Birkhead *et al.*, 2005; Mossman *et al.*, 2009) and so samples of fixed sperm from the same males were analysed (see Animals sub-section above) to acquire average mid-piece lengths for each male. To do this, 10 μL aliquots from the fixed sperm samples were incubated with the mitochondrial stain Mitotracker Green FM (500 μM, Molecular Probes, Eugene, OR) and the nucleic acid stain

Hoechst 33342 (0.5 mg/mL, Molecular Probes, Eugene, OR) in the dark for 2 mins. The labelled sperm were loaded on glass slides with coverslips and imaged at 400X using a fluorescence wide-field microscope (Leica DMBL with Infinity 3 camera, Luminera Corporation).

Image processing

The density of cristae in the mitochondria was measured from the TEM images as the area of the mitochondria occupied by cristae. In each image, a ROI was defined around the mitochondrial section and this was binarised using a manual threshold for each image to isolate the mitochondrial matrix. The count of the thresholded pixels was calculated using the 'regionprops' function in MATLAB to get the area occupied by the mitochondrial matrix. The 'imfill' function from the Image Processing Toolbox (Thompson and Shure, 1995) in MATLAB was used to dilate the matrix selection to fill gaps occupied by the cristae (Figure 4). This gave a selection that described the area occupied by the mitochondria in cross-section. The area occupied by the cristae was derived by subtracting the area occupied by the matrix from the total area of the mitochondria in cross-section.

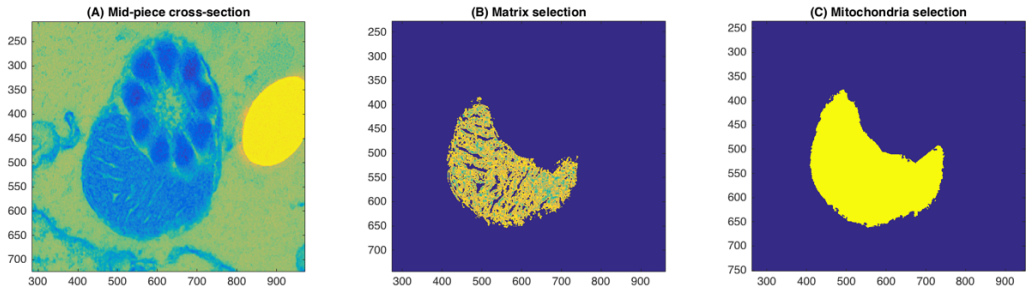

Figure 4: Mitochondrial packing. (a) TEM image of the mid-piece cross-section (b) selection of the mitochondrial matrix (in yellow) made using a threshold and (c) selection of the mitochondria (in yellow).

From high-resolution TEM sperm sections it was also possible to obtain accurate mid-piece diameter measurements. In these cross-sections sperm mitochondria had an elliptical shape, with the minor axis in-line with the flagellar diameter and the major axis extending to either side of the flagellum. Measurements of (1) the flagellum diameter, (2) mitochondrial minor axis diameter, and (3) mitochondrial major axis diameter were made from 10 images where the microtubule doublets appeared to be in a circular arrangement, indicating that the section was close to 90° to the sperm longitudinal axis (Figure 5).

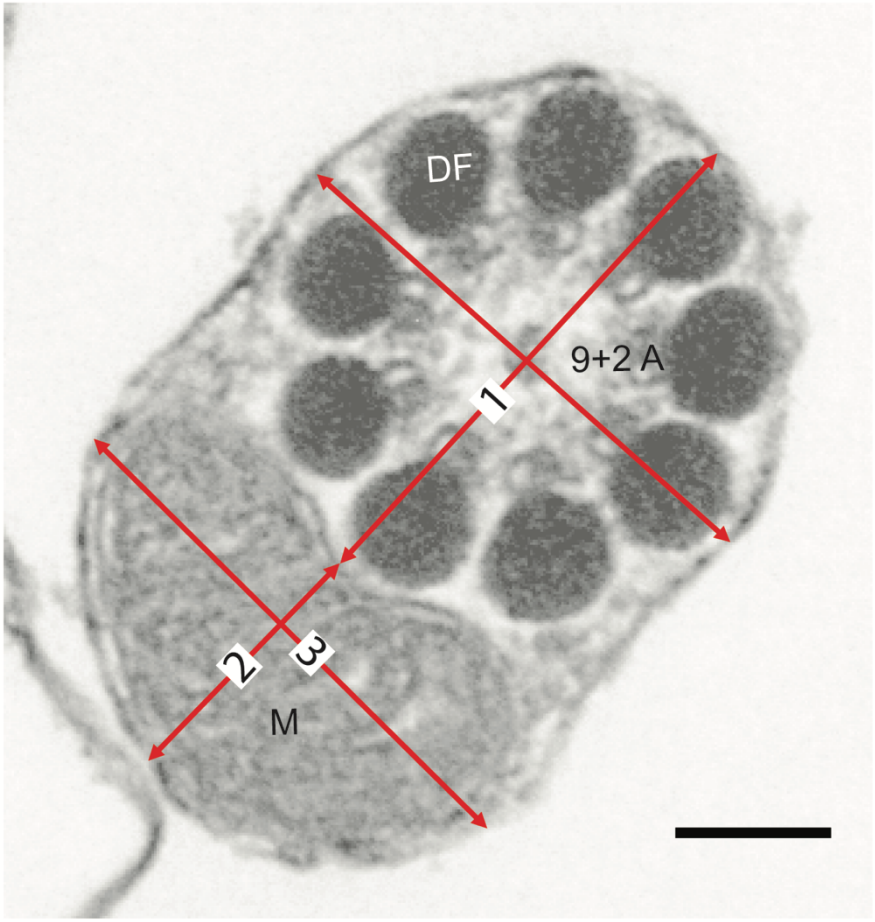

Figure 5: TEM image of cross-section of sperm mid-piece showing mitochondria (M), and the 9+2 axonemal structure (9+2 A) [nine microtubule doublets and a central pair of microtubule singlets] and electron dense bodies called dense fibres (DF) within the flagellum. Measurements were noted for (1) flagellum diameter, (2) mitochondrial minor axis, and (3) mitochondrial major axis diameters. Scale bar – 100 nm

Measurements of sperm flagellar length and total length were recorded along with mid-piece length from the fluorescence wide-field microscopy images by tracing along the respective sperm components in the images using the 'segmented line' tool and the 'measure' function in Fiji (Schindelin *et al.*, 2012) as described previously [see supplementary material for (Bennison *et al.*, 2015)]. Straight helix length has previously been calculated using a general equation which multiplies the mid-piece length measured in this way (i.e. coiled) by a standard constant (Birkhead *et al.*, 2005). However, this equation relies on the assumption that mid-piece radius is uniform within and between males. As one of my objectives was to test this assumption, the equation for straight helix length was not computed and coiled mid-piece length measurements were used directly in the analysis.

4.3. Data Analysis

Statistical analysis was performed using R version 3.2.3 (R Development Core Team, 2015). Mixed effects models were parameterised using the 'lmer' function from the {lme4} (Bates *et al.*, 2014) and the {lmerTest} (Kuznetsova *et al.*, 2016) packages, to test the effect of mid-piece length on (1) volume of mitochondrial helix and (2) number of helical gyres using data from part one of the study. Model (1) included volume of mitochondrial helix as computed from the SPIM images as the dependent variable, while the count of gyres along the mid-piece was included as the dependent variable in model (2). Both models included mid-piece length as a fixed effect and bird ID as a random effect.

Using data from part two of the study, the areas of the mitochondrial cross-sections were calculated as the count of pixels occupied by the mitochondria as described in the methods section above. The areas occupied by the mitochondrial matrix and the cristae were measured similarly. A dependent variable was created to represent cristae density within the mitochondria by binding together the area occupied by the

cristae and the area occupied by mitochondrial matrix for each cross-section and this was fitted to a mixed effects model with a quasi-binomial to correct for model overdispersion using the 'glmmPQL' function from the {MASS} package (Venables and Ripley, 2002) with mid-piece length as the explanatory variable and bird ID as a random effect.

Finally, the effect of mid-piece length on (4) the cross-sectional area of the mitochondria was assessed using a mixed effects model using the 'lmer' function. The cross-sectional area for the mitochondria from each sperm was calculated by assuming the area of an ellipse and using the minor axis and major axis radii measured from the TEM images (Figure 4). This was included as a dependent variable in a mixed effects model along with mid-piece length as an explanatory variable and bird ID as a random effect.

As data fitted to the models were acquired in separate tests involving different sets of individuals, a multivariate mixed effects model could not be used. Instead, statistical significance from the individual models was determined against a conservative Bonferroni-corrected critical p-value of 0.05/4 (the number of individual comparisons) i.e. 0.0125.

4.4. Results

Mid-piece structural organisation

Zebra finch sperm were found to have a diameter of 0.544 ± 0.167 μm (mean ± SD) at the mid-piece, as measured from the high resolution TEM images. This puts the sperm mid-piece thickness close to the resolution limit of the SPIM after multi-view deconvolution (lateral PSF = 0.654 μm, axial PSF = 1.220 μm). There was no significant effect of mid-piece length on mitochondrial cross-sectional area [estimated effect = -0.002, t = -2.250, p = 0.027 (not significant when compared to critical p = 0.0125)] as measured from TEM images. Although the volume of the mitochondrial

helix measured from SPIM images was likely to be over-estimated due to insufficient resolution, a positive linear relationship was found between this volume and mid-piece length [estimated effect = 1.617, t = 4.918, p = <0.001, $r^2_{(m)}$ = 0.285, $r^2_{(c)}$ = 0.731; Figure 6 (A)] implying helix thickness is uniform along the length of the mid-piece (albeit with some unexplained variation), which is consistent with the above results from the TEM images.

Mid-piece length was found to be highly correlated with the number of gyres (helical turns) along the mitochondrial helix [estimated effect = 0.233, t = 13.438, p = <0.0001, $r^2_{(m)}$ = 0.769, $r^2_{(c)}$ = 0.874; Figure 5 (B)], such that an increase in length corresponded with an increase in number of gyres. The mean length along flagellum occupied by each gyre was 3.785 ± 0.4 μm (mean ± SD).

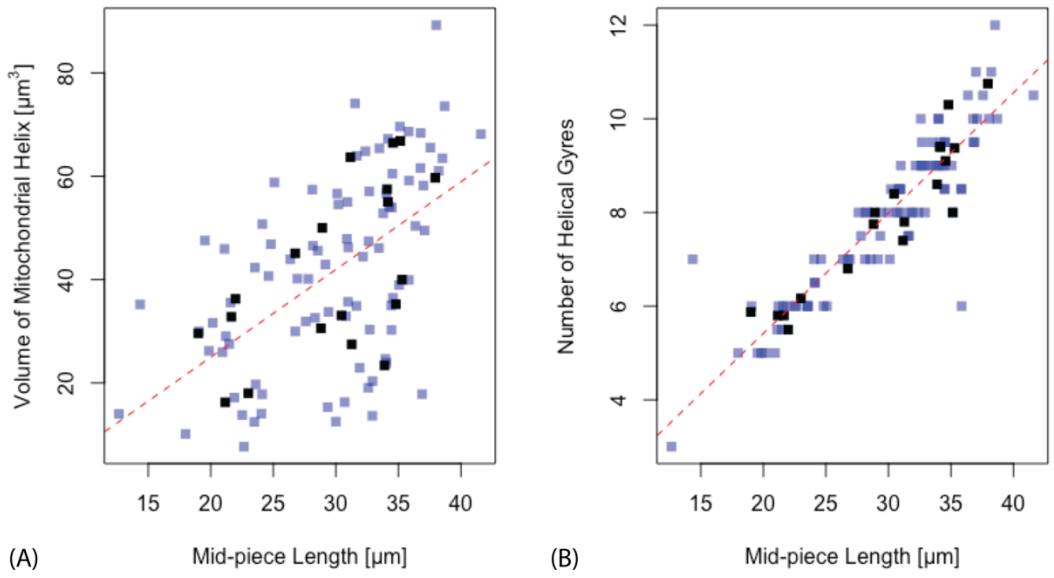

Figure 6: (A) Volume of the mitochondrial helix increased significantly with mid-piece length. (B) Mitochondrial helix gyres have a standard length such that, increase in mid-piece length corresponds with increase in number of gyres. For both plots, the blue data points represent the raw data while mean values for each male (n = 19) are represented as black data points.

Mid-piece internal organisation

There was a statistically significant quadratic relationship between mid-piece length and the proportion of mitochondria occupied by cristae (estimated effect = -1.574, t = -3.390, p = 0.0009, r^2 = 1.793e-06), but this relationship explained only 0.000001% of the variation in mitochondrial area occupied by cristae, indicating that either (a) other factors are much more important in determining mitochondria packaging, or (b) this trait is inherently variable.

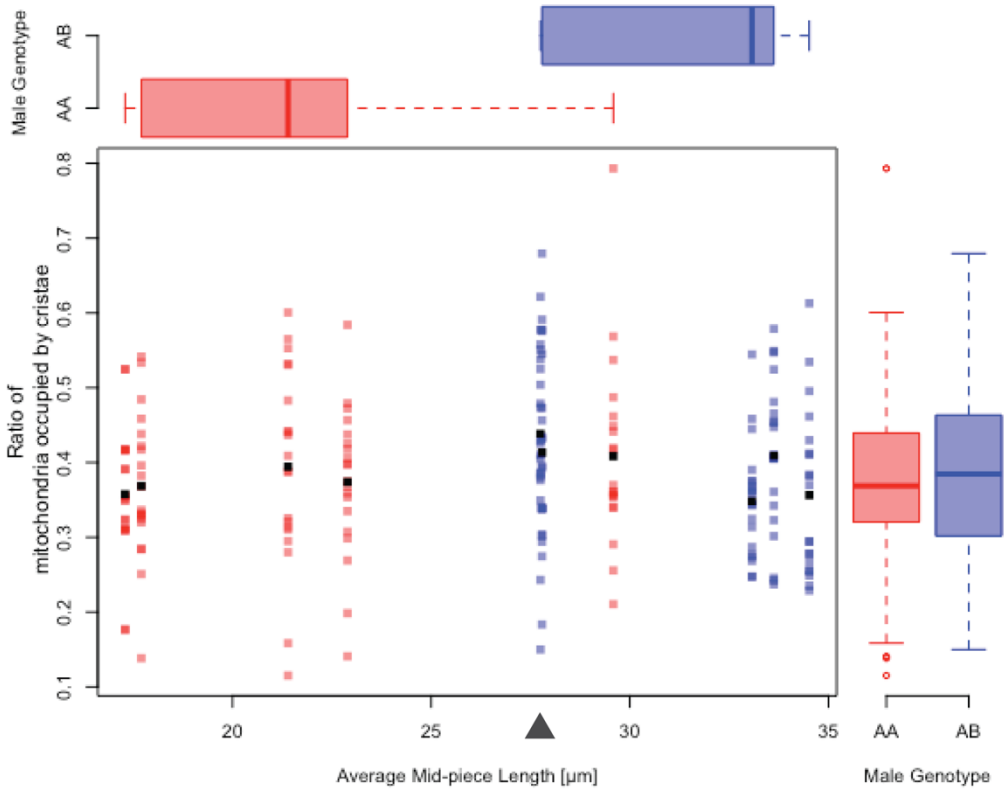

Figure 7: Mitochondrial packing shows a marginal but non-significant increase with increasing mid-piece length up to 28 μm (triangle). Sperm trait genotype, which is a determinant of mid-piece length (boxplots top) did not affect mitochondrial packing (boxplots right). The red colour represents data from AA genotype males (n = 5) and blue colour represents data from AB genotype males (n = 5). The black data points represent the mean values for every male.

The mitochondria showed an elliptical shape in cross-section with a major axis radius of 0.252 ± 0.157 μm (mean ± SD) and a minor axis radius of 0.110 ± 0.030 μm (mean ± SD). The flagellum along the mid-piece showed a radius of 0.183 ± 0.030 μm (mean ± SD). The large variation in the major axis diameter might explain the variation in the cross-sectional area of the mitochondria. Unfortunately, as the TEM images were not serial sections, it was not possible to test if this variation was attributable to variation along the length of the mitochondrial helix.

4.5. Discussion

The results of this study show that sperm mid-piece volume increases linearly with mid-piece length, implying that mid-piece thickness is consistent between males regardless of their overall sperm morphology, and therefore appears to be no trade-off between mid-piece length and thickness i.e. longer mid-pieces are not simply more "stretched out".

Since thickness is consistent along the length of the mid-piece, longer mid-pieces have a larger overall volume, suggesting they may also have a higher energetic capacity. Contrary to this prediction, however, Bennison *et al.* (2016) showed that zebra finch sperm with shorter mid-pieces possessed the highest concentrations of stored ATP. This discrepancy cannot be explained by the internal organisation of the mitochondria, since the results reported here showed that the relative area occupied by cristae in the mitochondria of sperm with long and short mid-pieces does not differ – long and short mid-pieces exhibit very comparable mitochondrial packing in cross-section. I therefore propose that stored ATP may not be a clear indicator of sperm mitochondrial activity, and instead, measurements of active sperm metabolism might yield a more accurate portrayal of sperm energetic capacity and its effect on swimming velocity. In fact, higher stored ATP content could be indicative of a lower efficiency in ATP transfer or usage within the flagellum. In addition, mitochondria are dynamic and regulate

metabolism by rearranging their internal structure between two main states – a condensed matrix with wide cristae and a wide matrix with condensed cristae (Hackenbrock, 1966; Cogliati *et al.*, 2013). This dynamism might explain the variation in mitochondrial packing I observed within males (Figure 7).

An interesting and unexpected finding of this study was that zebra finch sperm are much narrower than previously reported (Birkhead *et al.*, 2005). My measurements find the radius of the mid-piece, as measured from the centre of the flagellum to the centre of the mid-piece helix, to be 0.293 ± 0.05 μm (mean $\pm$ SD), which is an order of magnitude smaller than the 3 μm reported previously (Birkhead *et al.*, 2005). The transmission electron microscope (TEM) used for this study had a point-to-point resolution limit of 34×10^{-4} μm (3.4 Å) - sensitive enough to detect wide within-male variation in the major axis radius of the mitochondria. However, standard TEM image data lacks the three-dimensional information that can be obtained from SPIM to test if this variation also exists within mid-pieces.

The sperm radii measurements obtained from the SPIM volumetric images were twice as large as those obtained from the TEM images, a disparity that was due to the use of diffraction-limited light microscopy techniques for measuring sperm. Sperm range in length across animal phyla from 8 μm for the Hymenoptera [*Meteorus sp.*] to 58,000 μm for the Diptera [*Drosophila bifurca*] (Pitnick *et al.*, 2009a). This dimension is therefore large enough to measure using diffraction-limited microscopy. However, when making transverse measurements of sperm, the resolution of the system must be taken into consideration. Due to the different limitations of both SPIM and TEM, further research into the ultrastructure of sperm mitochondria should look towards super-resolution three-dimensional imaging techniques such as structured illumination microscopy (SIM) or cryo-electron tomography to facilitate investigation of three-dimensional organisation.

Consistent with the findings of Fawcett *et al.* (1971), I found the sperm mitochondrial helix to have a regular helical periodicity, with a repeatable length along each gyre (helical turn). Moreover, I found mid-piece thickness, as well as the internal organisation of the mitochondria, to be relatively consistent between males, implying that long mid-pieces simply possess a greater amount of the same mitochondrial material as compared to short mid-pieces. Fawcett *et al.* (1971) described the addition of mitochondria at the base of the flagellum before the caudal extension of the microtubule bundle which drives the compression and fusion of the mitochondria to impart the helical shape during spermiogenesis in finches. My results imply a potential genetic control on the first step in this process, wherein the number of mitochondria allowed to assemble is programmed depending on the sperm morphology genotype.

I found considerable within male variation in mitochondrial cross-sectional area (although there were no significant differences between males), which may result from thicker gyres at one end of the mid-piece being compensated for by thinner gyres at the other end. Such compensation may result in a regulated structure of the mitochondrial helix, with possible implications for hydrodynamics. Humphreys (1972) and Vernon and Woolley (1999) described the 'twist-drill' motion exhibited by most passerine sperm, with forward motion is achieved by the sperm revolving around its own longitudinal axis, suggesting an important contribution of the helical shape to motility. However, very little is understood of the nature of this contribution and the role of helical periodicity and regulated symmetry in helical sperm motion.

In conclusion, I have shown that sperm volume per unit length does not vary depending on absolute mid-piece length, demonstrating that there is no trade-off between sperm thickness and length. Consistent with this, mitochondrial packing is consistent across long and short mid-pieces, implying that long mid-pieces are larger 'engines' for sperm.

Chapter 5.

Visualising female sperm storage

5.1. Introduction

Across many internally fertilising taxa, females have evolved the capacity to maintain viable sperm in specialised sperm storage organs in their reproductive tract as a strategy to maximise fertility. Sperm storage ensures the female has sufficient sperm for fertilisation when copulation and ovulation are not synchronised (Birkhead, 1992). Since female promiscuity is common across taxa [e.g. birds (Birkhead and Møller, 1995), mammals (Hanken and Sherman, 1981; Tegelström *et al.*, 1991; Amos *et al.*, 1993), reptiles (Uller and Olsson, 2008), fishes (Avise *et al.*, 2002) and insects (Gromko *et al.*, 1984; Moritz *et al.*, 1995; Crozier and Fjerdingstad, 2001)], storage also provides the opportunity for females to exert control over post-copulatory processes (Eberhard, 1996; Birkhead and Møller, 1998; Simmons, 2001). Post-copulatory sexual selection has driven the diversification of sperm storage organs, which vary from single bean-shaped structures in many damselfly species (Siva-Jothy, 1987; Córdoba-Aguilar *et al.*, 2003), to one or more sac-like spermathecae in certain fly species [e.g. three spermathecae in *Scathophaga stercoraria* (Ward, 1993); two spermathecae along with a seminal receptacle in many Drosophila species (Pitnick *et al.*, 1999)], and multiple epithelial crypts in snakes (Fox, 1956), lizards (Conner and Crews, 1980), turtles (Gist and Jones, 1989) and birds (Zavaleta and Ogasawara, 1973; Bakst, 1987).

In birds, epithelial sperm storage crypts are called sperm storage tubules (SSTs) and are located in the utero-vaginal junction (UVJ) of the oviduct (Bobr *et al.*, 1964). The number of SSTs possessed by a single female ranges from around 500 SSTs in the UVJ of the budgerigar [*Melopsittam undulatus*] to 20,000 in the turkey [*Meleagris gallopavo*] (Birkhead and Møller, 1992). One possible explanation for the large numbers of SSTs is that it allows for the spatio-temporal segregation of sperm from competing ejaculates within the oviduct (Briskie, 1996; King *et al.*, 2002; Hemmings and Birkhead, 2017). Briskie (1996) reported a spatio-temporal gradation in maturation, size and filling of SSTs, from the vaginal to the uterine end of the UVJ in the yellow-headed blackbird (*Xanthocephalus xanthocephalus*). Evidence suggests that avian SSTs are a site of sperm selection: Steele and Wishart (1996) demonstrated experimentally that when chicken sperm were treated to remove surface proteins from their membranes, they could not enter the SSTs after normal intra-vaginal artificial insemination, even though sperm treated in the same way were capable of fertilising the ovum when inseminated further up the oviduct, past the selective barrier of the vagina and UVJ. Bobr *et al.* (1964) also noted a lack of abnormal sperm in the SSTs of domestic fowl [*Gallus domesticus*], suggesting that abnormal sperm are unable to reach or enter sperm storage sites. However, the mechanisms by which sperm are selected prior to or during storage remain poorly understood.

To better understand the mechanistic basis of sperm selection during storage, we first require a clearer picture of how the SSTs function. Despite a number of detailed descriptive studies, we still do not know if SSTs play an active or passive role in sperm storage. Froman (2003) proposed a model for sperm storage where SSTs are passive, with sperm motility being pivotal in sperm retention in SSTs. According to this model, sperm must maintain an optimum swimming velocity to maintain their position and counter a fluid current within the SST. This model is supported by evidence that faster sperm emerged out of SSTs later than slower sperm (Froman *et al.*, 2002), and that passive loss of

sperm from storage might be sufficient to explain last male precedence in the domestic fowl, turkeys, and zebra finches [*Taeniopygia guttata*] (Birkhead *et al.*, 1988; Birkhead and Biggins, 1998; but see Hemmings and Birkhead, 2017). However, other studies have detected the presence of sperm motility suppressors such as lactic acid in Japanese quail [*Coturnix japonica*] SSTs (Matsuzaki *et al.*, 2015), critical concentrations of calcium and zinc in the SSTs of chicken, turkeys and Japanese quail (Bakst and Richards, 1985; Holm *et al.*, 2000a), and carbonic anhydrase in the SSTs of turkeys, quail [*Coturnix coturnix*] and ostriches [*Struthio camelus*] (Holm and Ridderstråle, 1998; Holm and Wishart, 1998; Holm *et al.*, 2000b). The neurotransmitter acetylcholine, released by nerve endings detected in the vicinity of SSTs (Freedman *et al.*, 2001), has been shown to enhance sperm motility (Atherton *et al.*, 1980), implying a nervous control on sperm mobilisation at ejection from SSTs. Additionally, Hiyama *et al.*(2014) presented evidence for the potential role of heat shock protein 70 (HSP70) – a family of proteins that stabilise other proteins and bestow greater resistance to damage on the cell when exposed to stressors like heat (Lindquist and Craig, 1988) – in enhancing sperm motility at sperm release. The HSP70 proteins were found to be localised in the surface epithelium of the UVJ and their levels were regulated throughout the ovulatory cycle in Japanese quail (Hiyama *et al.*, 2014). Such evidence for sperm motility suppression and activation within or near the SSTs suggests storage may not be as passive as Froman (2003) suggested.

Alternatively, SSTs may be dynamic structures, capable of directed constriction and dilation to actively trap or eject sperm. Sperm entry and exit may also be regulated by other, more subtle biochemical and/or immunological processes. Numerous studies have failed to find smooth muscle fibres or myoepithelial cells (Van Krey *et al.*, 1967; Gilbert *et al.*, 1968a; Freedman *et al.*, 2001) around SSTs, but Freedman *et al.* (2001) detected fibroblast-like cells and an F-actin rich cytoskeletal mesh called the "terminal web" in turkey SST epithelia. The terminal web is composed of contractile proteins (actin and myosin) and has been shown

to contribute to contractility in other tissues, such as intestinal brush border cells (Hirokawa *et al.*, 1983; Keller *et al.*, 1985) and embryonic pigmented epithelia in chicken (Owaribe *et al.*, 1981). Freedman *et al.* (2001) also found terminal innervations in the turkey UVJ, suggesting there may be some degree of nervous control over SST function. Recent evidence also suggests the possibility of SST contraction, influenced hormonally, by the action of progesterone (Ito *et al.*, 2011; Hemmings *et al.*, 2015).

The lack of consensus on SST function can be attributed to the absence of any direct *in vivo* observations of sperm-female interactions and our limited understanding of SST structure and physiology. The avian oviduct is convoluted, with opaque, muscular walls, creating numerous practical limitations for making *in vivo* observations using conventional microscopy techniques. Empirical studies so far have mainly used histology (Van Drimmelen, 1946; Bobr *et al.*, 1964; Gilbert *et al.*, 1968a; Bakst, 1998) and electron microscopy (Van Krey *et al.*, 1967; Bakst, 1978; Schuppin *et al.*, 1984; Holm *et al.*, 2000a; Bakst and Bauchan, 2015) of fixed tissue sections, but these approaches generally provide two-dimensional information only, and any temporal changes that may be seen in living tissue are completely lost. Moreover, serial sectioning is laborious and loss of material can be difficult to avoid. Commonly used light microscopy alternatives rely on thin sections and squash preparations (Bakst, 1992; King *et al.*, 2002) which distort the tissue and allow only limited imaging depths.

The aim of this chapter is to describe the three-dimensional structure of SSTs, imaged through segments of the oviduct of female zebra finches [*Taeniopygia guttata*]. This work was made possible by the development of a novel method for live, *ex vivo* imaging using selective plane illumination microscopy (SPIM). This microscopy technique allowed me to optically section through the tissue up to depths of 100 μm (see Chapter 2) while leaving it physically whole, so that UVJ folds could be

imaged without distorting or damaging the mucosal tissue structure. I also demonstrate that the inherent autofluorescence emitted by oviductal tissue can be harnessed for imaging purposes, removing the need to use labels that may affect normal cell behaviour. The images and data obtained from this work provide the first true estimates of the 3D shape and structure of avian SSTs in living tissue.

5.2. Materials and Methods

This study required the development and testing of novel imaging methods, so a dedicated 'Methods Development' section describing this preliminary work precedes the rest of the methods in this chapter.

Methods Development

Optimising the SPIM set up

Imaging was performed on our self-built SPIM microscope (see Chapter 2 for a detailed system description). Images were captured using a sCMOS camera (Orca Flash 4.0 V2 C11440-22CU, Hamamatsu Photonics) which was triggered by the Piezo Controller (E-725.3CD, Physik Instrumente Ltd) and files were written to disk using HCImageLive software (Hamamatsu Photonics).

For the purposes of this study, minor adjustments were made to the sample chamber on the microscope set-up by fitting a temperature controlled heated cable (Repti Heat Cable, ZooMed Laboratories Inc.) around the sample chamber to enable imaging of live tissue at physiological temperatures. The heated cable was wrapped around all sides of the chamber for uniform distribution of heat.

Imaging Media

The choice of imaging media is critical for successful live imaging. The imaging media must be able to support live processes over prolonged periods while also having a refractive index (RI) that matches the objective lenses being used. Mismatches between objective lens RI and imaging media RI impart spherical aberrations and distort the point spread function (PSF) of the imaging system (Hecht, 2002). The SPIM uses water immersion objective lenses that are optimised for imaging through media with RI equal to that of water (RI = 1.33). As live tissue cannot be maintained in water (due to damage resulting from osmolysis), the physiological solution phosphate buffered saline (PBS, Sigma Aldrich) is generally used as an alternative (Huisken *et al.*, 2006). Tests were performed to compare the effect PBS and another physiological solution, phenol free DMEM/F12 (with added HEPES, Gibco™) on the PSF of the imaging system.

100 nm TetraSpeck™ Microspheres (Invitrogen™) were embedded in 1% agarose and imaged to obtain the system PSF (as described in Chapter 2) with water, PBS and DMEM/F12 as imaging media and with a light sheet thickness of 4.060 μm. PBS and phenol free DMEM/F12 both extend the axial PSF of the system only slightly compared to imaging in water (Figure 1). The PSF extension for DMEM/F12 (PSF_{axial} = 4.280 μm) was marginally larger than that with PBS (PSF_{axial} = 4.179 μm). I interpreted these results to be indicative of both PBS and DMEM/F12 showing similar performance as imaging media, but since PBS alone lacks the necessary nutrients for prolonged maintenance of tissue health and sperm motility, the phenol-free DMEM/F12 mix was used for the imaging experiments in this chapter.

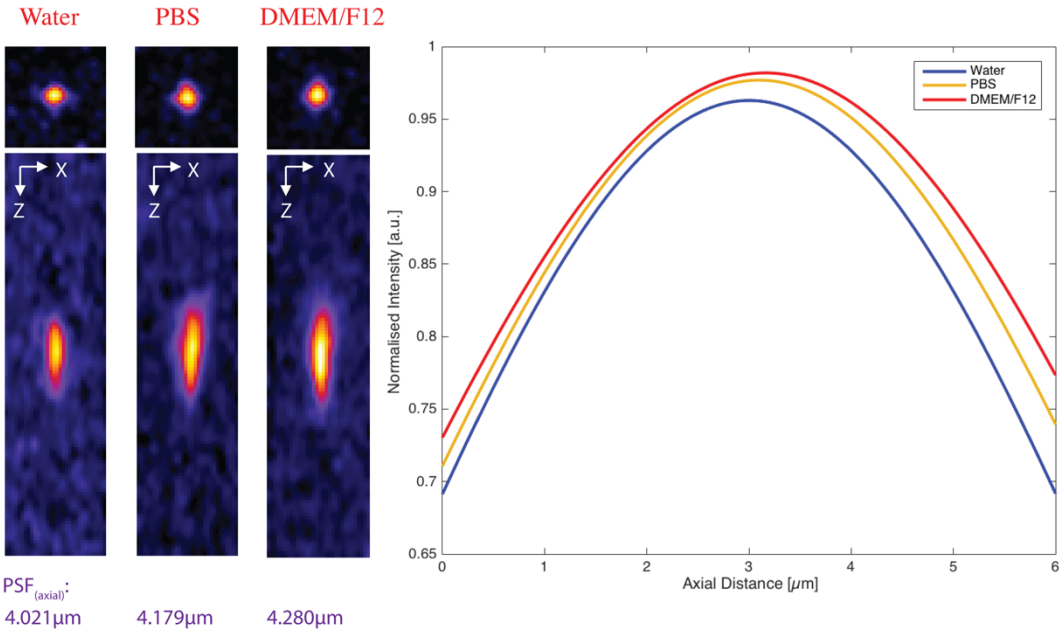

Figure 1: PSF of the system with water, PBS and phenol-free DMEM/F12. PSF values were measured using 100 nm TetraSpeck™ Microspheres (left top row – lateral PSF; bottom row – axial PSF). PBS and phenol-free DMEM/F12 show similar performance under the imaging conditions tested.

Sample Suspension

Conventional sample suspension methods with SPIM involve embedding samples in agarose or alternatively, using adhesives or hooks to grip large tissue samples. Embedding the tissue would block access to SST orifices making it inappropriate for studying sperm-female interactions. Moreover, gripping UVJ tissue with hooks or adhesives was found to be unsuitable in preliminary tests due to the flexible nature of the tissue, which resulted in wobble during imaging scans. To overcome this problem, a modified sample holder was designed for suspending UVJ tissue in the sample chamber as follows:

The bottoms of free-standing micro-centrifuge tubes were cut to a depth of 5 mm. 1 mL syringes were cut to remove the dispensing tip and the micro-centrifuge tube pieces were fixed at right angles to the syringes using epoxy glue (see Figure 2). The well of the micro-centrifuge tube was filled with silicon elastomer (SYLGARD® 184; Dow Corning). UVJ

tissue samples and/or individual UVJ folds could be mounted on to the surface of the silicon elastomer using the ends of fine insect needles. The free end of the syringe was fastened on the sample arm of the SPIM positioning system for imaging.

Figure 2: Customised sample holders of two sizes for imaging oviduct tissue samples. The tissue samples were pinned on the silicon elastomer surface with the UVJ mucosal surface and the SST orifices exposed.

Characterisation of tissue autofluorescence

To identify suitable fluorescence excitation sources and emission filters for imaging SSTs, the autofluorescence spectra from UVJ tissue were analysed. The UVJ was isolated from live oviduct tissue immediately after dissection and placed in ice cold PBS to delay tissue necrosis. A STS-VIS Miniature Spectrometer (Ocean Optics) was used to record the autofluorescence emission spectra with excitation from a blue laser (λ_{ex} = 440 - 490 nm) and a red laser (λ_{ex} = 630 - 660 nm). A cuvette was filled with PBS and blank readings were recorded using each laser excitation, one at a time. Following this, the UVJ tissue was introduced into the cuvette with PBS and the autofluorescence emission spectra for each excitation source was recorded. Two more sets of data were recorded from the same tissue sample. The cuvette contents were emptied and the

cuvette rinsed with PBS between each replicate reading. Data were recorded using Overture software (Ocean Optics).

The emission spectrum from blue excitation (440-490 nm) showed broad autofluorescence signal with a peak at λ_{em} = 635 nm (Figure 3). Weak autofluorescence signal was also seen in the 520-550 nm range. No appreciable emission peaks were noted with excitation at 630-660 nm (Figure 3).

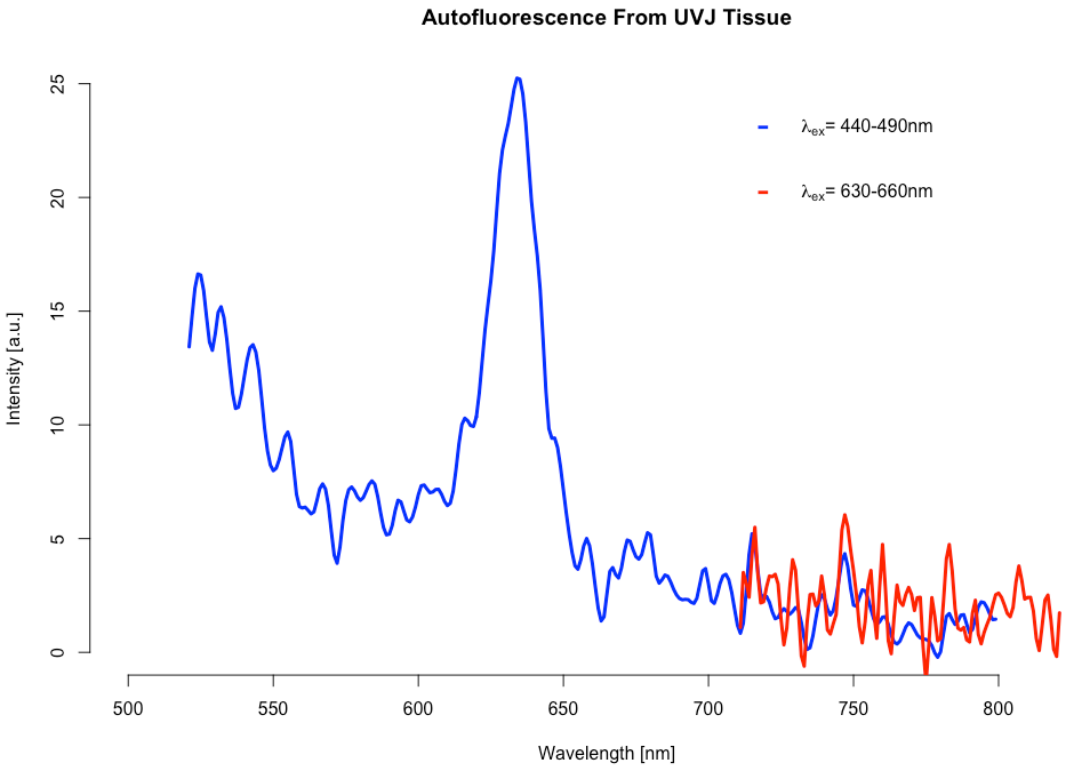

Figure 3: Tissue autofluorescence emission peaks at 635 nm with 440-490 nm excitation. No autofluorescence emission was noted when the tissue was excited in the 630-660 nm range.

Since autofluorecence emission from the UVJ tissue was noted when excitation was in the blue (440-490 nm) range, the 473 nm laser on the SPIM was used for imaging the UVJ tissue. Preliminary imaging in the absence of any emission filters showed the scattering noise from tissue

was too great to capture fine structural detail [Figure 4, (A)]. In an attempt to overcome the scatter, a ground glass disk attached to a servomotor was installed in the illumination path of the microscope. This ground glass disk ('de-speckler') was made to spin at high speeds during imaging. The resulting scrambled laser light averaged-out the scattered light from the tissue while still allowing for the image to form in the imaging plane (McKechnie, 1975; Smith, 1983). However, in the absence of emission filters, although speckled noise was removed, no fine structural detail could be discerned. Under these imaging conditions, SSTs themselves were not visible in the UVJ tissue [Figure 4, (B)]. Therefore, a 520 nm long pass (LP) fluorescence emission filter (Semrock, Inc.) was introduced in the SPIM detection pathway to filter out tissue scatter by wavelength. This approach eliminated maximum scatter while allowing tissue autofluorescence to pass through to the camera sensor [Figure 4, (C)]. Using the de-speckler in combination with the emission filter resulted in excessive loss of signal and did not result in any improvement to the image. The de-speckler was therefore removed from the final microscope set up and imaging was performed with the fluorescence emission filter alone.

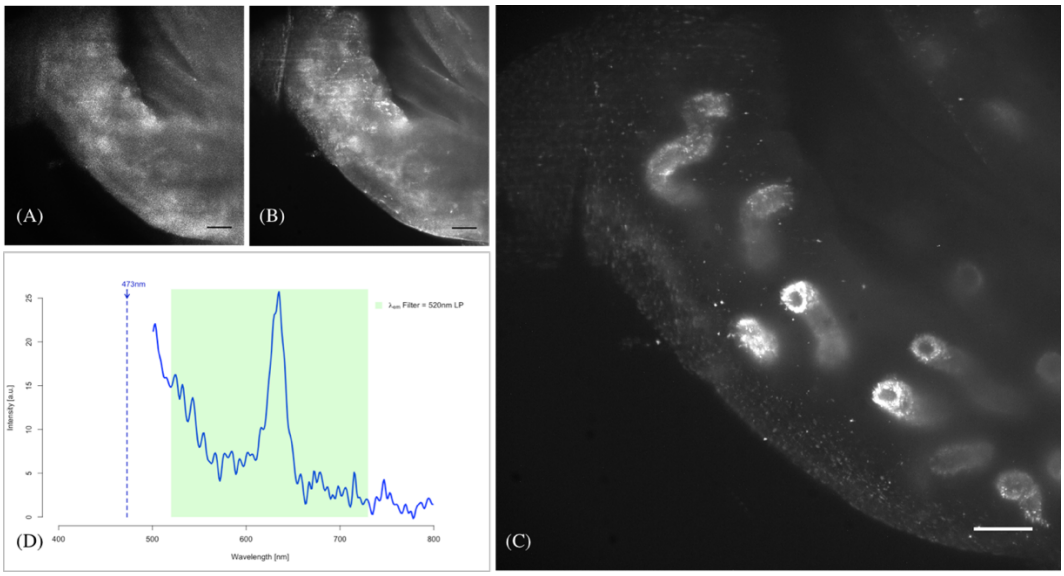

Figure 4: UVJ tissue was imaged using 473 nm laser excitation (A) without any emission filters, (B) with a ground glass de-speckler and (C) - (D) with a 520 nm LP fluorescence emission filter. Scale bar – 50 μm.

Once the scattering noise was removed using the fluorescence emission filter, SSTs were clearly identifiable in live UVJ tissue. SSTs had a punctate appearance on account of autofluorescent granules in the SST epithelia [Figure 4, (C)], which appeared to be mostly confined to SST epithelial cells and were present along the entire length of the SST from orifice to blind end. No other cell structure or organelle was visible in these autofluorescence images. Similar granules were not visible in fixed and labelled tissue or in histological sections. This is likely to be an effect of fixation and/or the autofluorescence signal being lower than the signal from the external fluorophore respectively.

To determine the organisation of the autofluorescent granules in the SST epithelium, live UVJ folds (n = 10 birds) were imaged using the SPIM. These images were compared to those of fixed UVJ tissue folds imaged, on the SPIM after staining for nucleic acids (n = 3 birds), and on a bright-field microscope after general histochemical staining (n = 3 birds).

Imaging methods for live and fixed UVJ tissue on the SPIM are described in detail below (see "Analysis of SST shape"). For histochemical examination, pieces of fixed UVJ tissue from three females were sent to the Skeletal Analysis Laboratory (skelet.AL) at the University of Sheffield for processing. The tissue was set in resin blocks and 3 μm thick sections were cut using a microtome. The tissue sections were stained with haematoxylin to label nucleic acids and eosin to label the cytoplasm and other acidophilic structures. The sections were mounted on individual slides and micrographs were taken of the slides on an upright microscope with bright-field (Leica DMBL with Infinity 3 camera, Luminera Corporation) at 250X magnification using a tiling method. Multiple overlapping image tiles with a 50% overlap were taken for each slide. The individual image tiles were then stitched together using the 'TrakEM2' plugin (Cardona *et al.*, 2012) in Fiji (Schindelin *et al.*, 2012) to digitally reconstruct each histological section.

The SST epithelium is polarised (Figure 5) with the nuclei at the basal end of each cell, at the periphery of the SST in cross-section. 10 random SST transverse sections from the histology slides for each bird (n = 3 birds) were measured using Fiji (Schindelin *et al.*, 2012). Two measurements were recorded for each (1) the lumen diameter; (2) the diameter between SST nuclei (referred to as 'inter-nuclear diameter' from here on), and (3) the diameter bound by the basement membrane (the 'outer diameter') of the SST from each cross-section (Figure 5). The diameter of the SST from autofluorescence images and the inter-nuclear diameter from SPIM images were measured as outlined later in the chapter (see "Analysis of SST shape" and workflow diagram, Figure 8).

To characterise the autofluorescence, 12 random autofluorescent granules were measured from 5 SSTs imaged using the SPIM. The measurements (1.000 ± 0.2 μm (mean ± SD)) were near the resolution limit of the system (~0.800 μm, also see Chapter 2) implying that the granules are likely to be sub-resolution in size [Figure 6, (B)].

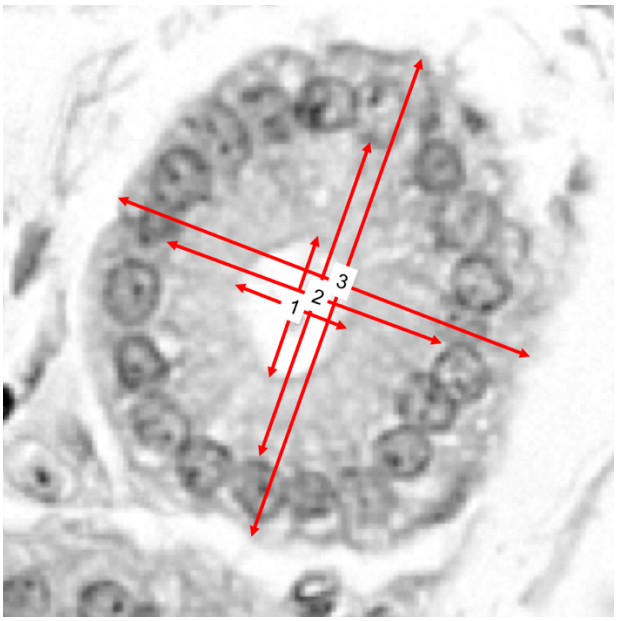

Figure 5: Cross section of a SST from histology with arrows indicating the diameters measured from the images: 1. lumen diameter, 2. the inter-nuclear diameter and 3. outer diameter of the SST.

Table 1: Diameter measurements [μm] from SST sections

	n (Birds*)	Diameter (mean ± S.D.)
lumen from histology	3	8.299 ± 2.342 μm
autofluorescence from SPIM	10	16.075 ± 6.603 μm
inter-nuclear diameter from SPIM	3	22.912 ± 7.695 μm
inter-nuclear diameter from histology	3	26.873 ± 5.339 μm
outer diameter of SST from histology	3	40.235 ± 5.657 μm

*Data are based on 10 randomly selected SST transverse sections per individual.

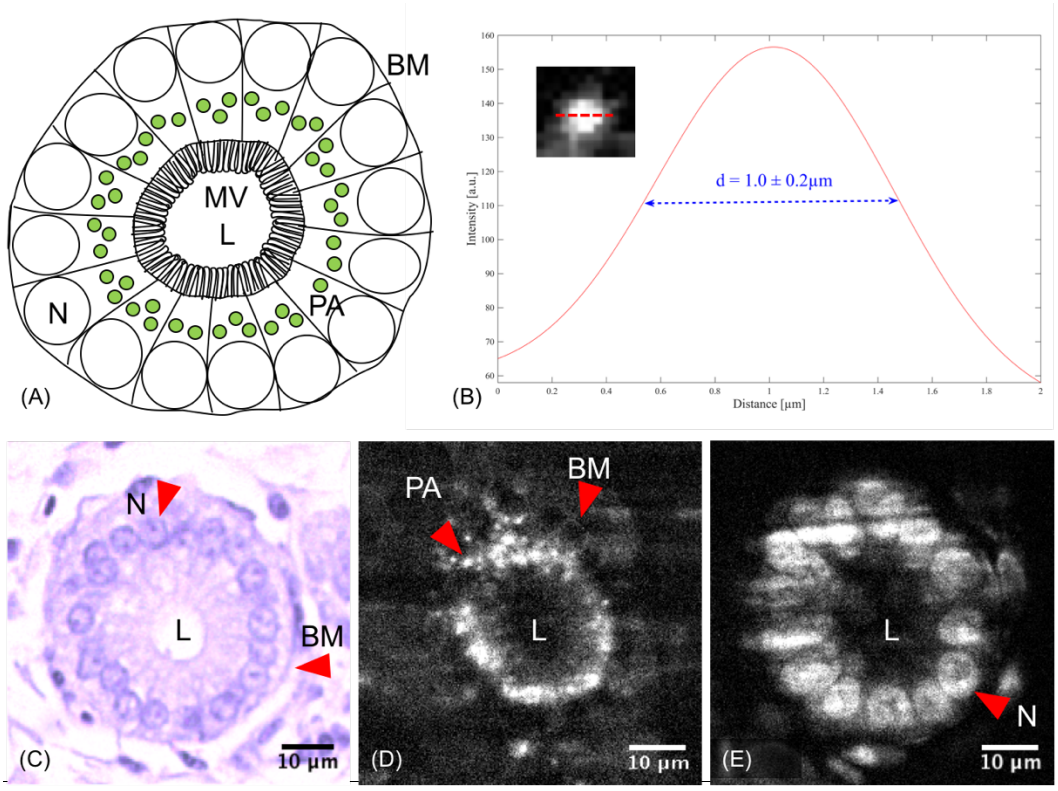

Figure 6: (A) Schematic of SST transverse section showing cellular polarisation with nuclei (N) towards the basement membrane (BM) and microvilli (MV) at the apical end of the epithelium. The punctate autofluorescence (PA) detected by the SPIM is present proximal to the nucleus but not at the apical end of the epithelium near the lumen (L). (B) Fluorescence intensity profile through an autofluorescent granule. The full width at half maximum (FWHM) indicates a diameter of 1±0.2 μm (Mean±SD), which is at the resolution limit of the system, suggesting the granules are sub-resolution in size. (C)-(E) Cross section of SST from histology, autofluorescence imaged on the SPIM, and SYTO-13 labelled nuclei imaged on the SPIM respectively.

These diameter measurements indicate that the autofluorescent granules are present in the supranuclear region of the SST epithelium (Figure 6). The three different diameter measurements from the histology images showed a linear correlation (lumen and inter-nuclear diameter: estimated effect = 0.362, t = 5.715, p = <0.0001) suggesting that lumen size scales proportionately with the size of the SST epithelial cells (Figure 7). Changes in the diameter of autofluorescence could therefore be considered to be representative of changes in SST lumen size, so the three-dimensional structure of live SSTs could be analysed from the autofluorescence images. In the following sections, "lumen" measurements specifically refer to the diameter between the autofluorescent granules.

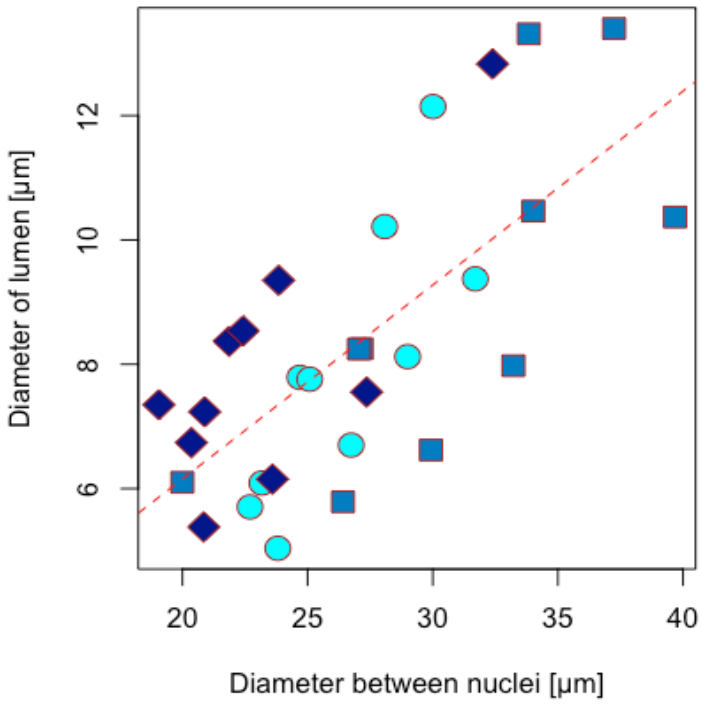

Figure 7: Diameter of SST lumen is positively correlated with diameter between SST epithelial nuclei and the outer diameter of the SST. Measurements were recorded from histology images (n = 3 birds, with 10 transverse sections measured per bird). Different shapes have been used for data points from each individual.

Analysis of SST shape

Animals

Oviduct tissue used in this study was obtained from ten zebra finch females from a captive population kept at the University of Sheffield (Birkhead *et al.*, 2005; Bennison *et al.*, 2015). The females were between one to three years of age and were kept separated from males for at least two weeks, before each was housed opposite a male with a wire divider to prevent copulation, as described in Chapter 3, Experiment 3. This separation period ensured that there were no sperm from previous copulations present in the oviducts or storage organs of the experimental females (Birkhead and Møller, 1992). To ensure the oviducts were sufficiently developed at the time of dissection, females were euthanized (in accordance with Schedule 1 [Animals (Scientific Procedures) Act 1986)] only after they laid a second egg in the ovulatory cycle. The oviduct, including the cloaca, was immediately removed and the connective tissue surrounding it was cleared to uncoil and straighten the vagina and the utero-vaginal junction (UVJ). The lower end of the oviduct was cut through the middle of the uterus to obtain a segment that consisted of the UVJ, vagina and cloaca. This piece of the oviduct was then cut open longitudinally and prepared for imaging (see below).

Sample preparation

(1) Label-free imaging of live tissue

Freshly dissected UVJ tissue was pinned on a petri-dish filled with silicone elastomer (SYLGARD® 184; Dow Corning) and a sufficient quantity of Ham's F10 Nutrient Mix was added to keep the tissue moist but not submerged. UVJ folds were cut individually with iris scissors and mounted one at a time, on the custom-made sample holder using fine insect needles. The sample holder, with the UVJ fold mounted, was suspended into the sample chamber containing phenol-free DMEM/F12 media, at 37° C, using the sample arm of the SPIM sample positioning

system. From previous tests (see Chapter 3), it was known that cilia on the epithelial surface of the female tract tissue could be observed beating under the microscope at 60 mins post dissection when maintained at 37° C and kept moist. This indicated that the tissue remained alive under these conditions. The suspended sample was illuminated with the 473 nm laser and a 520 nm LP fluorescence emission filter (Semrock, Inc.). The coarse sample positioning stages along with the rotation stage were used to manoeuvre the tissue until SSTs were visible in the field of view, and image stacks were acquired using 500 ms exposure, starting at the outer surface of the fold and moving up to 100 μm deep into the fold tissue.

(2) Labelled fixed tissue

After 2-3 folds had been removed for live tissue imaging (see above), the remaining UVJ tissue was flooded with 5% formalin while still pinned flat on the silicone elastomer and left to fix for two hours at room temperature. The fixed tissue samples were then transferred to micro-centrifuge tubes with 1 mL of 5% formalin for storage at room temperature. For imaging fluorescently stained SST epithelia, individual folds were cut from the fixed UVJ tissue of three females and incubated with 100 μL solution of 10 μM SYTO 13 nucleic acid stain (concentration based on trials for labelling large tissue samples; Molecular Probes Inc., UK) in PBS overnight at room temperature in the dark. The labelled folds were then mounted on the sample holder, one at a time, in the same way as the live tissue samples, and imaged in phenol free DMEM/F12 on the SPIM using the same settings as with live tissue (above), but with 1 ms exposure time.

Image Analysis

The image stacks acquired as described above were used to reconstruct 480 x 480 x 100 μm tissue sections containing three-dimensional information on SST structure as follows (see Figure 8 for an illustrated workflow guide). SST shape information was extracted by measuring (1)

the autofluorescence lumen diameter from images of live tissue and (2) the inter-nuclear diameter from images of labelled, fixed tissue, at ten points along the length of the SST. UVJ tissue image stacks were first pre-processed in Fiji (Schindelin *et al.*, 2012). Individual unbranched SSTs were selected from each female such that the entire SST structure was included in the 3D image stacks. Regions of interest (ROIs) were defined around the selected SSTs and these were cropped and saved as multi-page .tiff files. A Fiji macro was written to perform further pre-processing on the SST ROI images ('Dilate.ijm', Appendix). This macro (1) scaled the images to match the instrument voxel dimensions, (2) converted the image bit depth to 8-bit and (3) applied a background subtraction to isolate foreground information for processing.

The SSTs follow convoluted paths through the UVJ fold tissue, so in order to measure cross-sectional lumen diameter at multiple points, it was necessary to slice the image volume at oblique angles to ensure the measurement planes were perpendicular to the direction of the SST structure. This was accomplished by first tracing the direction of the SST structure using a dilated version of the SST image, to smooth the punctate autofluorescence (Figure 8). The dilated image was generated by applying a dilation filter using the 'MorphoLibJ' plugin (Legland *et al.*, 2016) followed by the application of Gaussian blur (see 'Dilate.ijm', Appendix). Two outlines for each SST were then semi-automatically traced, from the orifice to the blind end and along opposite sides of the SST lumen, using the 'Simple Neurite Tracer' (Longair *et al.*, 2011) plugin in Fiji. These traces were exported as '.csv' files of Cartesian coordinates for computing slicing positions along the SST.

The next stage of image analysis was performed using MATLAB® (2015b, version 8.6, MathWorks, Natick, MA) (for script see – 'SST_shape.m', Appendix). The two traces for each SST were imported into MATLAB and an average trace was computed from the Cartesian XYZ coordinates which passed through the SST lumen. SST length was measured from the

average trace for each SST. This averaged luminal trace was interpolated at ten equidistant points (Figure 8). At each interpolated point, the 3D coordinates of the two closest neighbouring points on the trace were found and a vector describing the direction of the trace at the point was computed using these neighbours. By using this vector and the points on the trace, a plane normal to the vector was computed for slicing. 2D image planes were extracted from the un-dilated original ROI stacks using the indices of the planes defined in this way. The intensities on the slice along with the coordinates of each pixel were exported using the 'ExtractSlice.m' (Teng, 2011) function. For every extracted slice, its distance from the orifice along the luminal trace of the SST was computed using the 'Arclength.m' (D'Errico, 2012) function, and the lumen was measured to record the major axis diameter (d1) and the minor axis diameter (d2). The 'slice number' also denoted the relative position of the slice along the SST with 'slice 1' at the orifice and 'slice 10' closest to the blind end of the SST.

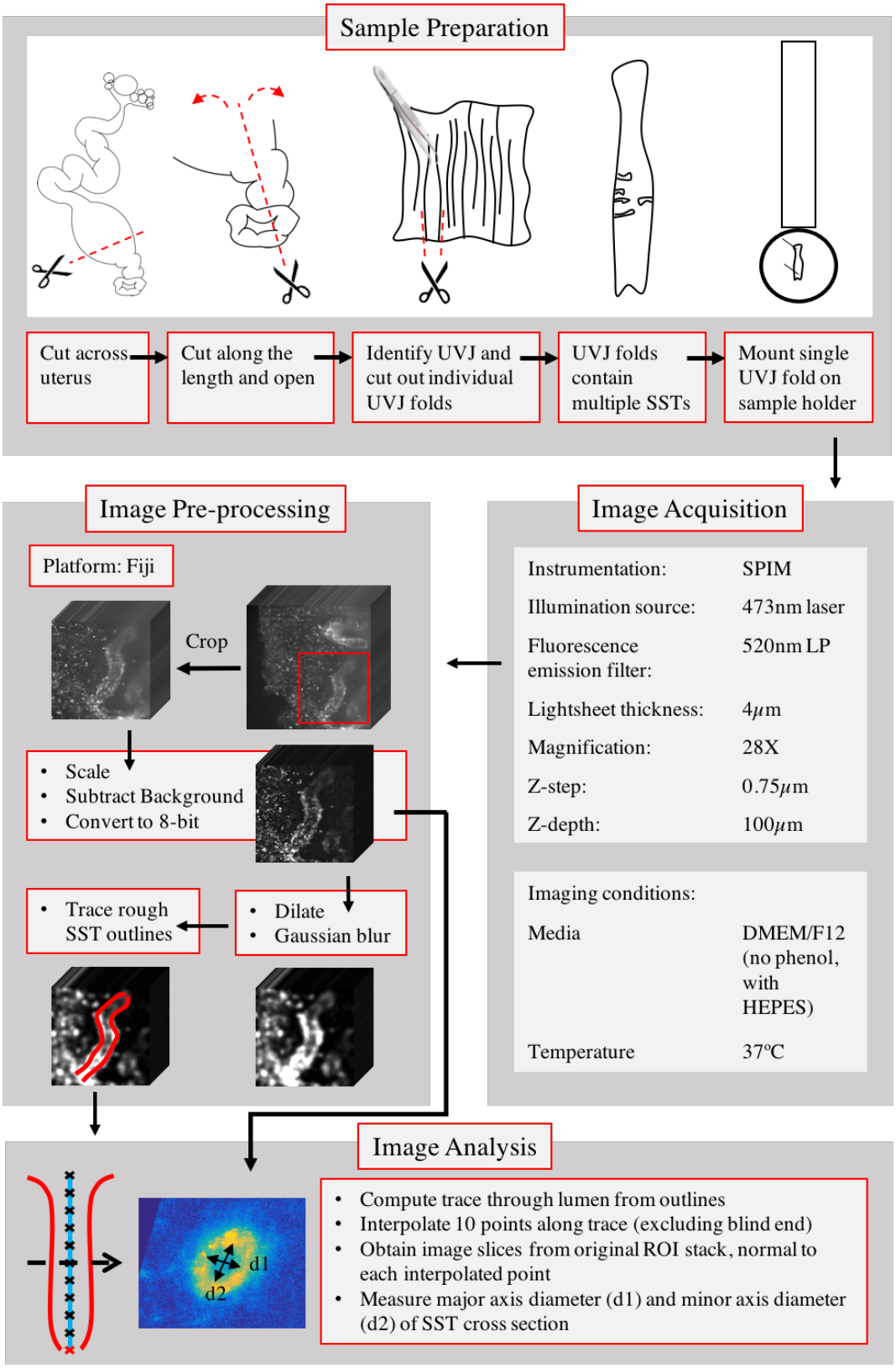

Figure 8: Workflow diagram for extracting structural information from label-free images of live SSTs. Full details of each step can be found in the main text.

5.3. Data Analysis

Data analysis was performed using the statistical package R, version 3.2.3 (R Development Core Team, 2015). The relationship between SST length and SST diameter was analysed using a mixed effects model ['lmer' function from the {lme4} package (Bates *et al.*, 2014) along with the {lmerTest} package (Kuznetsova *et al.*, 2016)] with average SST diameter [(d1+ d2) / 2] at the sampled point as the dependent variable, the distance of sampled point from SST orifice and the SST total length as fixed effects, and the bird ID as a random effect. Data from live and fixed UVJ images were analysed separately.

To assess if SST lumens are elliptical, a circularity index was calculated by dividing the lumen major axis diameter (d1) by the minor axis diameter (d2). A circularity index of one indicates a circular lumen. Change in circularity in response to SST length was assessed using a mixed effects model using the 'lmer' function (Bates *et al.*, 2014) with the circularity index as the dependent variable and the sum of the major and minor axis diameters (d1+ d2) [to account for magnitude of change in diameter along each axis], and distance of sampled point from SST orifice as fixed effects with an interaction term between them. The total length of the SST was also included as a fixed effect and bird ID was included as a random effect to account for repeated measures from each female.

5.4. Results

There was a significant quadratic relationship between SST diameter and the distance from the SST orifice (estimated effect = -16.761, t = -3.085, p = 0.003), such that SST diameter was smallest at its orifice and then showed a slight increase with distance up to a point, and then decreasing towards the blind end of the SST. This indicates that when functional, SSTs are constricted at their orifice (Figure 9). SST shape (and length) showed wide variation. A post-hoc comparison showed a wide, slightly

elliptical but variable SST shape at one extreme, and a thinner, more uniform tubular shape at the other. This variation appeared to be a continuous range rather than representing two independent morphs (Figure 10).

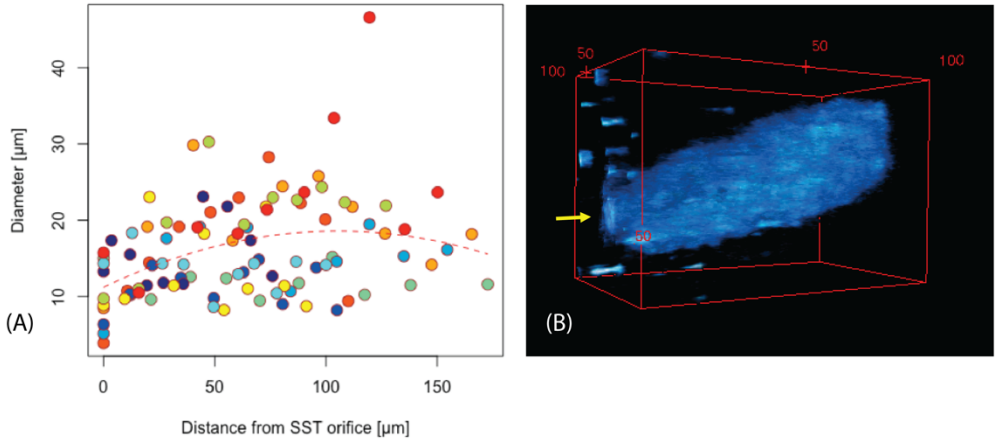

Figure 9: (A) SST diameter has a quadratic relationship with distance from the SST opening suggesting a constriction at the orifice and a slight increase in diameter along its length up to the middle of the SST. Each colour on the plot represents measurements from the same SST (n=10). (B) 3D rendering of an SST. Arrow is pointing at orifice. Scale on red bounding box is in μm

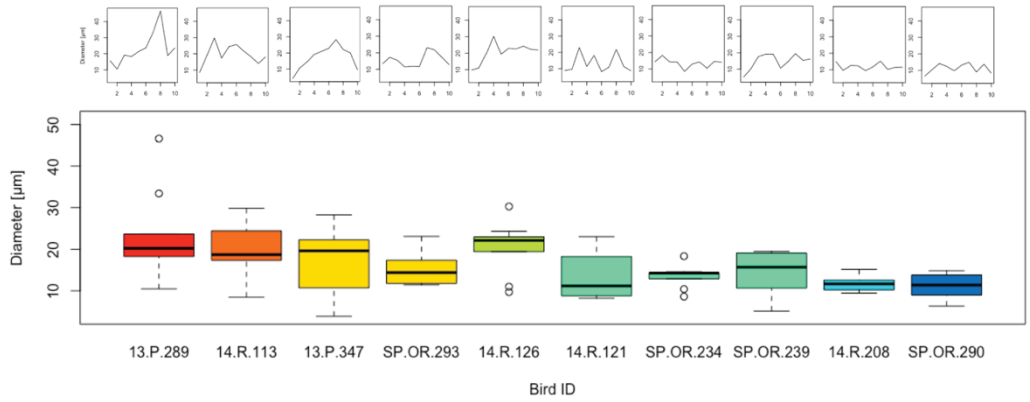

Figure 10: SST shapes lie on a continuous range (n = 10 birds) with wider SSTs on the left and thinner SSTs on the right. Each box plot represents a SST from an individual. The thick horizontal line represents the median and the whiskers represent the data range. Line graphs above each box plot show SST diameter against relative distance from orifice for each individual. Plots with the same colour represent SSTs that do not differ significantly from each other.

SST diameter did not vary with SST length, so long SSTs were neither wider nor thinner than short SSTs (estimated effect = 0.038, t = 1.058, p = 0.319). This was true for mean, maximum, and minimum diameter (Figure 11).

The circularity of the SST lumen did not vary significantly with SST diameter (estimated effect = 0.014, t = 0.979, p = 0.330), distance from orifice (estimated effect = 0.003, t = 0.587, p = 0.558), or the interaction between these two variables (estimated effect = -0.00009, t = -0.587, p = 0.559). Lumen circularity was also not related to SST total length (estimated effect = -0.004, t = -1.14, p = 0.282).

Measurements were also taken of SSTs from labelled fixed UVJ tissue. The results show a similar quadratic relationship between inter-nuclear diameter and distance from SST orifice (estimated effect = -25.293, t = -4.530, p = 0.0001, Figure 12) confirming that the autofluorescence has a uniform distribution and is a fair proxy for analysing SST shape in label-free images.

As size of the lumen diameter scaled linearly with the size of the SST epithelial cells (Figure 7), shape information from the above analyses could be extrapolated to the SST lumen giving a predicted value of 2.938 ± 0.513 μm (mean ± SD) for the lumen diameter at the orifice (Table 2).

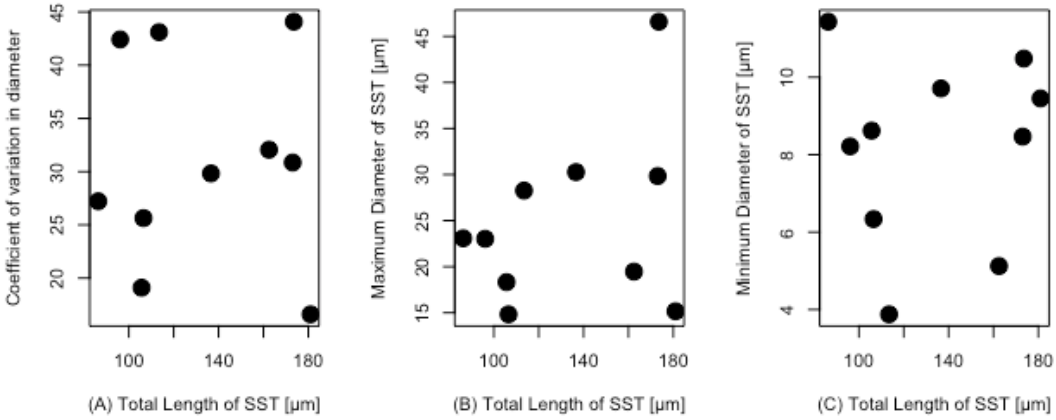

Figure 11: (A) Variation in SST diameter, (B) maximum SST diameter, and (C) minimum SST diameter are independent of the total length of the SST. Each data point represents one SST from one individual.

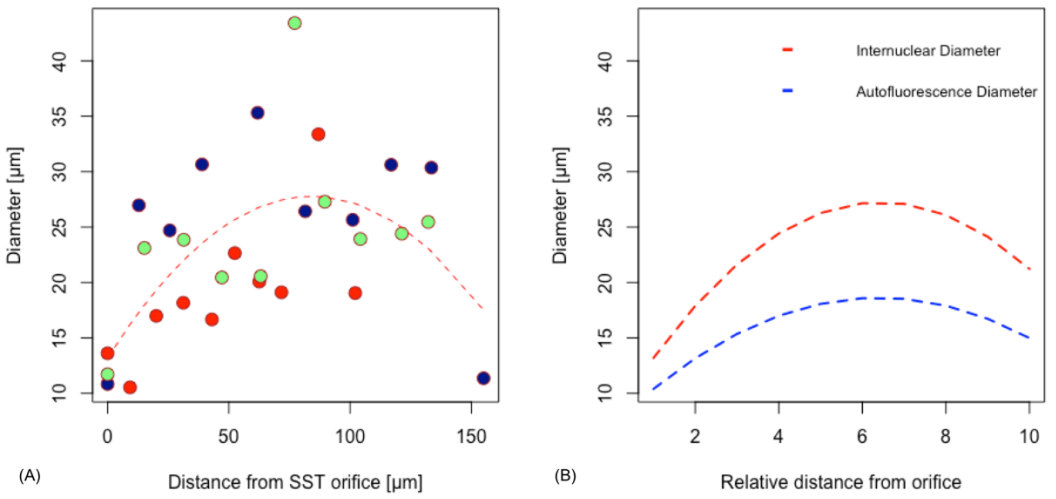

Figure 12: The inter-nuclear diameter shows the same relationship with distance from orifice as the autofluorescence diameter. (A) Each colour represents data from a SST. (B) Fits to experimental data from label-free images of SSTs (blue, n=10) and labelled fixed SSTs (red, n=3).

Table 2: SST dimensions at orifice and widest section

	Diameter (mean ± SD)	
	at orifice (μm)	**at widest section (μm)**
inter-nuclear diameter[1]	12.060 ± 1.419	30.830 ± 11.055
autofluorescence[1]	10.065 ± 4.288	16.374 ± 6.610
lumen diameter[2]	2.938 ± 0.513	9.733 ± 4.002

SST diameter is the smallest at its orifice and widest at the relative slice position 'slice 6', where slice 1 is at the orifice and slice 10 is nearest to the blind end of the SST.

[1]Measurements acquired from SPIM image z-stacks

[2]SST lumen diameter values were predicted from the model describing the relationship between lumen and inter-nuclear diameter (See Methods Development, Histological sectioning of fixed tissue)

5.5. Discussion

In this study, I demonstrate successful label-free imaging of live SSTs in UVJ tissue from zebra finch females. This was possible because of the presence of punctate/granular autofluorescence confined to the SST epithelial cells. These granules were found to have a supranuclear localisation in the SST epithelial cells (Table 1 and Figure 6). Although identifying the exact source of the autofluorescence was beyond the scope of this study, autofluorescence in a similar range has been noted in the ewe [*Ovis aries*] endometrium ($\lambda_{ex}/\lambda_{em}$ = 488/525-575 nm) (Druart *et al.*, 2009) and in human colonic crypts ($\lambda_{ex}/\lambda_{em}$ = 488/580 nm) (DaCosta, 2005). While such autofluorescence has been attributed to NADH metabolism in mitochondria (Brookner *et al.*, 2000; Druart *et al.*, 2009), another likely source might be lipofuscin in lysosomes (DaCosta, 2005). Mitochondria are not confined to the apical cytoplasm and tend to be elongated in the supranuclear region in SST epithelium in turkeys (Schuppin *et al.*, 1984) and domestic fowl (Burke *et al.*, 1972) so it is unlikely that these granules represent mitochondria. Lysosomes on the

other hand, are globular vesicles similar to the autofluorescent granules observed here in size (< 1 μm) (Chiba and Nakamura, 2001), and have been detected in the apical cytoplasm of turkey SST epithelia (Schuppin *et al.*, 1984), and less abundantly in domestic fowl (Burke *et al.*, 1972) and passerine alpine accentor [*Prunella collaris*] (Chiba and Nakamura, 2001). Multiple studies have also detected the presence of acid phosphatase, an enzyme found in lysosomes, in the supranuclear cytoplasm of SST epithelia in turkeys (Zavaleta and Ogasawara, 1973), quail (Renden *et al.*, 1981), domestic fowl (Gilbert *et al.*, 1968b) and ducks [*Anas sp.*] (Pal, 1977), but not in the SST lumen, which corresponds with the autofluorescence pattern we observed here. Acid phosphatase has been implicated in autolysis associated with oviduct regression (Heryanto *et al.*, 1997) as well as with sperm release (Pal, 1977). If this is true, the label-free imaging methods developed here may provide an exciting new means for investigating SST functional development throughout the reproductive cycle. Identifying the chemical nature of the autofluorescent substance present in SST granules therefore represents an important avenue for future research.

Due to the presence of these granules throughout the SST, autofluorescence was uniform and present along the entire length of the SST. This enabled SST shape measurements to be extracted from label-free images of living UVJ tissue samples. SST diameter was found to be constricted at the orifice (Figure 9) and then increased slightly with distance from the orifice until near the midpoint along the SST's length, after which generally diameter decreased up to the blind end of the tubule. The maximum diameter along the SST however, is a fraction of the total length of the SST. The relationship between SST diameter and distance from orifice also held true with data from labelled nuclei (Figure 11), confirming that the shape measured from autofluorescence images was real and not an artefact resulting from the distribution of the autofluorescence granules.

The constricted opening found at the entrance to the SSTs is suggestive of contractile activity for active entrapment and release of sperm. The F-actin rich terminal web – the only possible contractile structure found in SSTs so far (Freedman *et al.*, 2001) – was detected among epithelial cells in a coiled pattern along the entire length of the SSTs in turkeys. It remains to be seen if (1) such organisation of the terminal web is conserved in SSTs across bird species, (2) the structure contributes to SST contraction, and (3) contractility is isolated to specific regions such as the orifice.

Alternatively, SSTs may retain a relatively fixed structure during their functional period. The narrow SST orifice (mean diameter of about 3 μm), with the added obstruction of microvilli [1-2 μm in length, (Bakst and Bauchan, 2015)] could restrict the rate of sperm (mean diameter at mid-piece - ~0.6 μm, see Chapter 4, Results) entering the SST. Such a constricted orifice structure together with the microvilli may act like a valve, allowing unidirectional movement of sperm only, and preventing them from being flushed back out. The small luminal diameter along the SST (mean - 9 μm, Table 1) may also limit the ability of sperm to turn around inside the SST and swim out.

In addition to their constricted openings SSTs were also found to have slightly elliptical lumens in cross-section, with the major axis diameter being about 1.6 times (95% CI = 1.472, 1.811) larger than the minor axis diameter. This ellipticity was independent of SST radius, the distance along the SST from orifice, or total SST length. Cross-sectional ellipticity would increase the surface area of the SST epithelial apical surface and allow for greater number of microvilli (as compared to a circular lumen with the same volume) for increased contact with sperm and optimum exchange of nutrients and waste.

My results show that lumen diameter varies widely, resulting in a continuous range of SST shapes, from those with larger diameters and a more distended shape at one extreme and thinner, more uniform SSTs at

the other (Figure 13). Shugart (1988) made similar observations in Cedar waxwings [*Bombycilla cedrorum*], describing two types of SSTs – longer tubules without constrictions and shorter buds with constrictions. However, the SSTs measured in our study did not show any correlation between shape and SST total length and constriction was always at the orifice. Mero and Ogasawara (1970) and Burke (1968) also described 'swollen' tubules in chicken and suggested swelling to be associated with sperm release, but contrary to our findings, they report the widest section of such swollen tubules to be at the terminal end. Birkhead *et al.* (1990) suggested that some SSTs might remain inactive in the zebra finch UVJ even in its fully developed state. It is possible that some of the variation in SST shape that we observed can be explained by the presence of functional and non-functional SSTs, but it is unclear which of the two shape extremes would represent active SSTs, or if a conformational change in SST shape from functional to non-functional by neural stimulation (Gilbert and Lake, 1963; Freedman *et al.*, 2001) and/or hormonal effects (Ito *et al.*, 2011; Hemmings *et al.*, 2015) could aid sperm release. Variation in SST shape might also be explained by factors not tested in this study, including age, hormone levels and location of the SST in the UVJ.

About 4 – 27% of all the sperm storage tubules in the zebra finch UVJ are branched (Birkhead and Hunter, 1990; Hemmings and Birkhead, 2017). These were not included in the present study but individual branches are expected to show similar shapes as unbranched tubules. Hemmings and Birkhead (2017) described (albeit a single observation) sperm from different males differentially stored in separate branches of a branched SST. Further study of the 3D structure of branched SSTs could shed light on the mechanisms that might prevent mixing in such branched tubules.

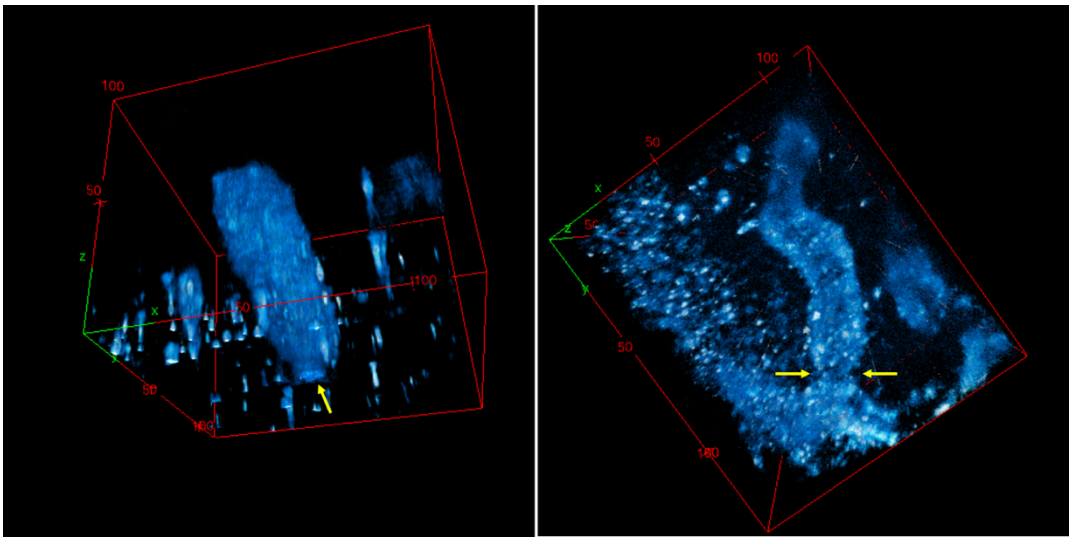

Figure 13: Sperm storage tubules (SSTs) imaged label-free using the SPIM. SST shaped showed a general constricted opening (yellow arrows) but varied between more elliptical shapes (left) and thinner, more uniform shapes (right). Scale on red bounding box is in μm.

In summary, I have shown here that SSTs in living tissue can be imaged label-free using a SPIM microscope, and this novel three-dimensional imaging technique has enabled the most detailed account of zebra finch SST structure to date. The imaging methods described here hold immense potential for studying SST function and interactions with sperm in real time.

Chapter 6.

Summary and Conclusions

6.1. Overview

In this thesis, I have demonstrated the use of three-dimensional fluorescence microscopy, using a purpose-designed self-built SPIM microscope, to study the structure and organisation of the sperm mid-piece (Chapter 4) and sperm storage tubules (SSTs) (Chapter 5) of a model passerine bird, the zebra finch. I have also reviewed a selection of candidate fluorescent labels for use in *in vivo* sperm tracking. Here I summarise these results and discuss potential avenues for future research. This thesis involved considerable development and optimisation of methods, so I include a section on the outcomes from these developments. Finally, I conclude by looking to future research directions that might emerge from this work.

Regulation of mid-piece size in zebra finch sperm

The results of this thesis show that the mitochondrial helix, which forms the mid-piece of zebra finch sperm, is a regulated structure with consistent thickness, helical periodicity and internal organisation (density of cristae packing) across males, irrespective of mid-piece length. Sperm with longer mid-pieces are therefore likely to have more mitochondria and as a consequence, may have a higher bio-energetic capacity than those with shorter mid-pieces. This work is important for our interpretation of previous work on zebra finch sperm energetics, which showed that, surprisingly, sperm with shorter mid-pieces had

higher concentrations of stored ATP (Bennison *et al.*, 2016). The apparent discrepancy between this finding, and the results reported in Chapter 4 of this thesis, may be explained in two key ways.

First, ATP may not be stored in the sperm mid-piece alone. Nevo and Rikmenspoel (1970), demonstrated bull [*Bos taurus*] and sea urchin [*Echinus esculentus*] sperm to possess ATP concentrations in excess of what was required for a steady state as per the ATP diffusion models they described, and suggested that this excess ATP might be stored in the sperm tail, buffered by the action of creatine phosphate. Accordingly, Bennison et al. (2016) demonstrated that zebra finch sperm with the shortest mid-pieces also tend to have the longest tails. It is possible that the high concentrations of stored ATP detected in Bennison et al.'s (2016) study were the result of long tails, rather than short mid-pieces, however, there has been no further empirical evidence to support Nevo and Rikmenspoel's hypothesis and so it remains to be seen if this is true.

Second, passerine sperm may not generate their energy by mitochondrial oxidative phosphorylation (OXPHOS) exclusively. Bennison *et al.* (2016) showed that swimming velocity was not determined by mid-piece length alone, but rather the ratio of mid-piece to tail length – sperm with a 1:1 mid-piece to tail length ratio were the fastest, implying a trade-off between a mid-piece and tail size. While the mitochondria in the mid-piece are responsible for oxidative phosphorylation (OXPHOS), cytosolic glycolysis in the tail is an alternative metabolic pathway available to sperm. Sperm from all avian species that have been studied primarily use the OXPHOS pathway (Sexton, 1974; Froman and Feltmann, 1998; Froman *et al.*, 1999; Rowe *et al.*, 2013), which has greater metabolic efficiency than glycolysis, but in some mammalian species, sperm generate most of their energy from glycolysis (Storey and Kayne, 1975; Takei *et al.*, 2014). OXPHOS and glycolysis are however, strongly linked and it is likely that most species lie on a continuum between a reliance on OXPHOS versus reliance on glycolysis for sperm energy production (Sexton, 1974; Cummins, 2009; Tourmente *et al.*, 2015). Interactions

between the mid-piece and flagellum, for the exchange of metabolites and metabolic products, could potentially determine power and therefore, swimming velocity. The extent of such an interaction between mitochondria and the cytoplasm might also help to provide an explanation for the optimal mid-piece to tail ratio observed in this species, and may also explain the helical structure of the mid-piece. Arranged as a helix, a given volume of mitochondria can extend further along the flagellum than if it enveloped the flagellum, and a spiral structure still maintains symmetry for progressive motion (Berg, 1993).

Important avenues for future research are to identify the mode of sperm energy production in zebra finch (and other passerine bird species) by studying active metabolism, and how it relates to sperm structure and performance.

Sperm storage tubules (SSTs) show a constricted opening

The work in this thesis has revealed that zebra finch sperm storage tubules have a constricted opening (Chapter 5), which is suggestive of contractility for the entrapment and release of sperm. This constricted opening is likely to be covered in microvilli, which would further obstruct sperm movement by acting like a turnstile to control rate of sperm entry (and possibly release). Freedman *et al.* (2001) detected the presence of a coiled organisation of F-actin in the SSTs of turkeys. This multicellular organisation of F-actin might possibly provide structural stability and/or contractility to SSTs, but it is not yet known if such organisation is present in the SSTs of the zebra finch. F-actin is prone to re-organisation which can be initiated by a number of factors, including the action of hormones or the nervous system (Sanchez *et al.*, 2012; Ambrosio *et al.*, 2014). The hormone progesterone has been implied as a potential sperm release factor in a few studies on female sperm storage in birds (Yoshimura *et al.*, 2000; Ito *et al.*, 2011; Hemmings *et al.*, 2015) and it is therefore plausible that progesterone may act on the organisation of

F-actin in the SSTs, mediating sperm release from storage. Consistent with this hypothesis, Ito *et al.* (2011) noted that SST dimensions changed following treatment with progesterone.

The results of Chapter 5 also showed that SST diameter varied widely across the SSTs measured, but this variation was irrespective of SST length. Variation in SST diameter could be indicative of functional changes in SST structure throughout the reproductive cycle. SSTs have been found to vary in size between the vaginal and uterine ends of the UVJ (Briskie, 1996), possibly due to differences in functionality and/or maturity. However, the location of the SSTs in this project were not recorded so I could not test whether variation in SST shape is related to the location of the SST in the UVJ.

Previous work has shown that SST length strongly correlates with sperm length across species (Birkhead and Møller, 1992; Briskie and Montgomerie, 1993), and within species, there can be coevolution of sperm and female storage organs [e.g. seminal receptacles in artificially selected populations of *Drosophila melanogaster*; Miller & Pitnick (2002)]. This thesis presents the first known study of the three-dimensional structure of SSTs. It remains to be seen if the three-dimensional form of SSTs – particularly the shape and dimensions of the SST orifice – co-evolves with three-dimensional measures of sperm morphology, within and across species.

Our self-built SPIM harnessed autofluorescence, naturally present in the SST epithelium, to produce three-dimensional images of live tissue. The autofluorescent granules that facilitated this imaging were sub-resolution in size and had a supra-nuclear localisation (Chapter 5). These granules were not found in the lumen, so it is unlikely that they are secretory substances. However, their location in the female epithelium suggests they could be lipofuscin in lysosomes [lysosomes have been shown to have similar localisation, autofluorescence spectra and size (Chiba and Nakamura, 2001; DaCosta, 2005)]. Identifying the chemical

nature of these autofluorescing granules provides an exciting avenue for further research into SST biochemistry and secretory activity.

Research tool developments

In this thesis, I have demonstrated successful three-dimensional, label-free imaging of SSTs using a self-built SPIM microscope. Label-free imaging provides a powerful means to study live tissue dynamics with minimum treatment of the specimen. However, label-free autofluorescence imaging suffers from lower signal-to-noise ratio (SNR) than imaging with fluorophores, due to the comparatively lower intensity of the autofluorescence. This necessitates longer exposure times (Chapter 5), slowing down the imaging process and exposing the specimen to illumination for longer durations. The next step forward for this technology would involve the development of non-toxic labelling protocols that could quickly and efficiently label large UVJ tissue samples in a targeted manner, to improve SNR and enable faster imaging of dynamic processes.

The penetration depth of the self-built SPIM used in this thesis was limited to 100 μm. Some other variants of light sheet microscopy that alter the beam function of the light sheet [e.g. Bessel beam light sheet (Fahrbach *et al.*, 2013a)] or those that use multiphoton excitation (Mahou *et al.*, 2014) have reported higher penetration depths in large specimens. However, oviduct tissue, when imaged using a multiphoton point scanning microscope as part of the preliminary tests in Chapter 5, showed no notable improvement over the depth imaged as compared to our self-built SPIM. These multiphoton point scanning microscopes have been shown to perform slightly better at greater imaging depths than multiphoton light sheet microscopes (Supatto *et al.*, 2011). It is crucial that future developments in optical microscopy move towards the capability to image deeper and with higher imaging resolution in opaque, living specimens.

Since SPIM is a diffraction limited microscopy technique, there is a limit to the size of the objects it can resolve. In our microscope, the limit was approximately 800 nm in the lateral plane and 4 μm in the axial plane. Multi-view reconstruction improved this to 600 nm and 1 μm respectively, but this was still not sensitive enough to obtain precise data on zebra finch sperm measurements. The resolution of the microscope can be further improved by reducing the thickness of the light sheet (Chapter 2), but this will not be sufficient to allow structures beyond the resolution limit of the system to be imaged. Adaptations to SPIM such as lattice light sheet (Chen *et al.*, 2014) or LS-RESOLFT (Hoyer *et al.*, 2016) can allow for the microscope to achieve super-resolution imaging capabilities, but these are neither trivial nor cost effective to set up. Alternatives for further investigations into sub-resolution sperm structure are commercially available super-resolution microscopes such SIM, STED (both - Frolikova *et al.*, 2016) or STORM (Chung *et al.*, 2014).

Finally, I tested the effects of a range of commercially available organic fluorescent dyes for their effects on sperm structural integrity, motility, and interactions with the female reproductive tract (Chapter 3), in order to identify suitable candidates for labelling sperm for *in vivo* tracking. Although I demonstrated nucleic acid dyes to be more suitable than membrane dyes for studies of sperm function and sperm-female interactions, I found at least some limitations associated with all dyes tested. It is imperative that tests like those carried out in this thesis are replicated with other fluorophores, and not just organic dyes. Future research must consider the development of bespoke fluorophores, improved labelling techniques and the identification of suitable target sites on sperm cells.

6.2. Future Directions

The work described in this thesis has developed a suite of tools for imaging sperm-female interactions, *in vivo* and in real time. To date, research into avian sperm motility dynamics has mostly been restricted to *in vitro* studies, which may not provide biologically relevant information about sperm function and behaviour inside the female reproductive tract. Moving forward, it is therefore essential that sperm motility is characterised in three-dimensions, as well as in the presence of female tissue and/or oviductal fluid. SPIM has already been shown to be suitable for three-dimensional tracking studies (Ritter *et al.*, 2010), and the large sample chamber associated with the SPIM set-up would facilitate experimental manipulations required to test the effect of female substances on sperm motility in an un-constrained environment.

SPIM is also highly suitable for imaging labelled sperm inside SSTs. Following artificial insemination of females with *in vitro* labelled sperm, three-dimensional imaging of live SSTs would help answer many long standing questions regarding sperm entry and exit from SSTs, as well as the orientation and motility status of stored sperm in the SSTs – do they maintain a constant swimming velocity as Froman (2003) suggested, or are they quiescent? In an additional pilot project carried out towards the end of my PhD, I successfully imaged zebra finch sperm residing inside SSTs by fluorescently labelling fixed UVJ tissue from females that had been mated and therefore, had sperm in their SSTs, with 10 μM SYTO 13 (as described in Chapter 5; Molecular Probes Inc., UK), using the self-built SPIM system (Figure 1). Although studying sperm-female interactions inside the SSTs was beyond the scope of this thesis, this preliminary work nonetheless provides proof of concept, demonstrating SPIM to be an exciting tool for studying post-copulatory sexual selection in the future.

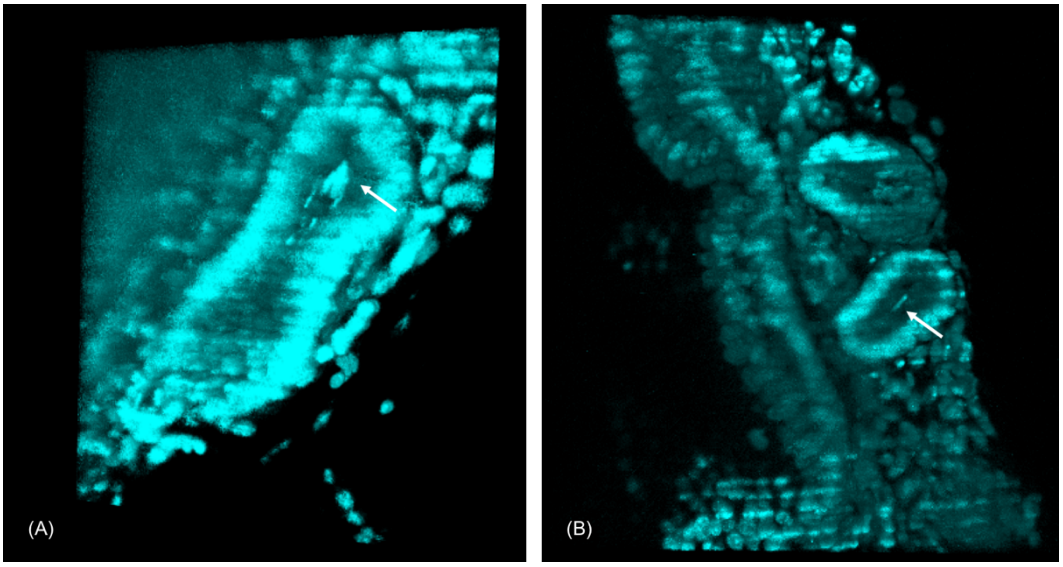

Figure 1: SSTs containing sperm (arrows). Fixed specimens were stained with the nucleic acid dye SYTO 13. Visible here: sperm nuclei (arrows) and nuclei from SST epithelia and surround UVJ tissue.

Ultimately, SPIM provides a means for the live imaging of sperm entering and/or leaving SSTs, shedding light on sperm selection. We are now within reach of achieving this, in part due to the developments described in this thesis.

Bibliography

Afzelius B (1959) Electron microscopy of the sperm tail; results obtained with a new fixative. *The Journal of Biophysical and Biochemical Cytology* **5** 269–278.

Agard DA (1984) Optical sectioning microscopy: cellular architecture in three dimensions. *Annual Review of Biophysics and Bioengineering* **13** 191–219.

Agate RJ, Scott BB, Haripal B, Lois C and Nottebohm F (2009) Transgenic songbirds offer an opportunity to develop a genetic model for vocal learning. *Proceedings of the National Academy of Sciences* **106** 17963–17967.

Ahrens MB, Orger MB, Robson DN, Li JM and Keller PJ (2013) Whole-brain functional imaging at cellular resolution using light-sheet microscopy. *Nature Methods* **10** 413–420.

Ambrosio JR, Ostoa-Saloma P, Palacios-Arreola MI, Ruíz-Rosado A, Sánchez-Orellana PL, Reynoso-Ducoing O, Nava-Castro KE, Martínez-Velázquez N, Escobedo G, Ibarra-Coronado EG *et al.* (2014) Oestradiol and progesterone differentially alter cytoskeletal protein expression and flame cell morphology in Taenia crassiceps. *International Journal for Parasitology* **44** 687–696.

Amos W, Twiss S, Pomeroy PP and Anderson SS (1993) Male mating success and paternity in the grey seal, Halichoerus grypus: a study using DNA fingerprinting. *Proceedings. Biological Sciences* **252** 199–207.

Anderson MJ and Dixson AF (2002) Sperm competition: motility and the midpiece in primates. *Nature* **416** 496.

Atherton RW, Cisson CM, Wilson BW and Golder TK (1980) Quantitation of avian spermatozoan motility: Neurochemical regulation. *Gamete Research* **3** 17–24.

Avise JC, Jones AG, Walker D and DeWoody JA (2002) Genetic mating systems and reproductive natural histories of fishes: lessons for ecology and evolution. *Annual Review of Genetics* **36** 19–45.

Bae YK, Kim E, L'Hernault SW and Barr MM (2009) The CIL-1 PI 5-Phosphatase Localizes TRP Polycystins to Cilia and Activates Sperm in C. elegans. *Current Biology* **19** 1599–1607.

Bakst MR (1978) Scanning Electron Microscopy of the Oviductal Mucosa Apposing the Hen Ovum. *Poultry Science* **57** 1065–1069.

Bakst MR (1987) Anatomical basis of sperm-storage in the avian oviduct. *Scanning Microscopy* **1** 1257.

Bakst MR (1992) Observations on the turkey oviductal sperm-storage tubule using differential interference contrast microscopy. *Journal of Reproduction and Fertility* **95** 877–883.

Bakst MR (1994) Fate of fluorescent stained sperm following insemination: new light on oviducal sperm transport and storage in the turkey. *Biol Reprod* **50** 987–992.

Bakst MR (1998) Structure of the avian oviduct with emphasis on sperm storage in poultry. *The Journal of Experimental Zoology* **282** 618–626.

Bakst MR and Bauchan G (2015) Apical blebs on sperm storage tubule epithelial cell microvilli: Their release and interaction with resident sperm in the turkey hen oviduct. *Theriogenology* **83** 1438–1444.

Bakst MR and Bauchan G (2016) Lectin staining of the uterovaginal junction and sperm-storage tubule epithelia in broiler hens. *Poultry Science* **95** 948–955.

Bakst MR and Bird DM (1987) Localization of Oviductal Sperm-storage Tubules in the American Kestrel (Falco sparverius). *The Auk* **104** 321–324.

Bakst MR and Richards MP (1985) Concentrations of selected cations in turkey serum and oviductal mucosae. *Poultry Science* **64** 555–563.

Bakst MR, Wishart G and Brillard JP (1994) Oviducal sperm selection, transport, and storage in poultry. *Poultry Science Reviews* **5**.

Barker DM (1994) Copulatory plugs and paternity assurance in the nematode Caenorhabditis elegans. *Animal Behaviour* **48** 147–156.

Bates DM, Machler M, Bolker BM and Walker SC (2014) Fitting Linear Mixed-Effects Models using lme4. *Journal of Statistical Software* **67** 1--48.

Bennison C (2014) Sperm morphology and fertilisation success in the zebra finch Taeniopygia guttata. University of Sheffield.

Bennison C, Hemmings N, Slate J and Birkhead T (2015) Long sperm fertilize more eggs in a bird. *Proceedings. Biological Sciences* **282** 20141897.

Bennison C, Hemmings N, Brookes L, Slate J and Birkhead T (2016) Sperm morphology, adenosine triphosphate (ATP) concentration and swimming velocity: unexpected relationships in a passerine bird. *Proceedings. Biological Sciences* **283** 69–149.

Berg HC (1993) *Random Walks in Biology*. Princeton University Press.

Bernasconi G, Hellriegel B, Heyland A and Ward PI (2002) Sperm survival in the female reproductive tract in the fly Scathophaga stercoraria (L.). *Journal of Insect Physiology* **48** 197–203.

Birkhead TR (1987) Sperm-storage glands in a passerine: the zebra finch Poephila guttata (Estrildidae). *Journal of Zoology* **212** 103–108.

Birkhead TR (1992) Sperm Storage and the Fertile Period in the Bengalese Finch. *The Auk* **109** 620–625.

Birkhead TR (1998) Cryptic female choice: criteria for establishing female sperm choice. *Evolution* 1212–1218.

Birkhead TR (2010) Post-copulatory sexual selection and the Zebra Finch. *Emu* **110** 189.

Birkhead TR and Biggins JD (1998) Sperm competition mechanisms in birds: models and data. *Behavioral Ecology* **9** 253–260.

Birkhead TR and Fletcher F (1995) Male phenotype and ejaculate quality in the zebra finch Taeniopygia guttata. *Proceedings. Biological Sciences* **262** 329–334.

Birkhead TR and Hunter FM (1990) Numbers of sperm-storage tubules in the Zebra Finch (Poephila guttata) and Bengalese Finch (Lonchura striata). *The Auk* **107** 193–197.

Birkhead TR and Møller AP (1992) Numbers and size of sperm storage tubules and the duration of sperm storage in birds: a comparative study. *Biological Journal of the Linnean Society* **45** 363–372.

Birkhead TR and Møller AP (1993) Sexual selection and the temporal separation of reproductive events: sperm storage data from reptiles, birds and mammals. *Biological Journal of the Linnean Society* **50** 295–311.

Birkhead TR and Møller AP (1995) Extra-pair copulation and extra-pair paternity in birds. *Animal Behaviour* **49** 843–848.

Birkhead TR and Møller AP (1998) *Sperm Competition and Sexual Selection*. Academic Press.

Birkhead TR and Montgomerie R (2009) Three centuries of sperm research. In *Sperm Biology*, pp 1–42.

Birkhead TR, Pellatt JE and Hunter FM (1988) Extra-pair copulation and sperm competition in the zebra finch. *Nature* **334** 60–62.

Birkhead TR, Pellatt JE and Hunter FM (1990) Numbers and Distribution of Sperm in the Uterovaginal Sperm Storage Tubules of the Zebra Finch. *The Condor* **92** 508–516.

Birkhead TR, Pellatt JE, Brekke P, Yeates R and Castillo-Juarez H (2005) Genetic effects on sperm design in the zebra finch. *Nature* **434** 383–387.

Bobr LW, Lorenz FW and Ogasawara FX (1964) Distribution of Spermatozoa in the Oviduct and Fertility in Domestic Birds. I. Residence Sites of Spermatozoa in Fowl Oviducts. *Journal of Reproduction and Fertility* **8** 39–47.

Bourgenot C, Saunter CD, Taylor JM, Girkin JM and Love GD (2012) 3D adaptive optics in a light sheet microscope. *Optics Express* **20** 13252.

Briskie J V (1996) Spatiotemporal patterns of sperm storage and last-male sperm precedence in birds. *Functional Ecology* **10** 375–383.

Briskie J V and Montgomerie R (1993) Patterns of Sperm Storage in Relation to Sperm Competition in Passerine Birds. *The Condor* **95** 442–454.

Brookner CK, Follen M, Boiko I, Galvan J, Thomsen S, Malpica A, Suzuki S, Lotan R and Richards-Kortum R (2000) Autofluorescence Patterns in Short-term Cultures of Normal Cervical Tissue. *Photochemistry and Photobiology* **71** 730–736.

Burke WH (1968) Release of spermatozoa from storage sites in the hen's oviduct. Univ. of California, Davis.

Burke WH, Ogasawara FX and Fuqua CL (1972) A study of the ultrastructure of the uterovaginal sperm-storage glands of the hen, Gallus domesticus, in relation to a mechanism for the release of spermatozoa. *Journal of Reproduction and Fertility* **29** 29–36.

Calhim S, Immler S and Birkhead TR (2007) Postcopulatory sexual selection is associated with reduced variation in sperm morphology. *PLoS ONE* **2** e413.

Cardona A, Saalfeld S, Schindelin J, Arganda-Carreras I, Preibisch S, Longair M, Tomancak P, Hartenstein V and Douglas RJ (2012) TrakEM2 software for neural circuit reconstruction. *PLoS ONE* **7** e38011.

Cardullo RA, Herrick SB, Peterson MJ and Dangott LJ (1994) Speract receptors are localized on sea urchin sperm flagella using a fluorescent peptide analog. *Developmental Biology* **162** 600–607.

Carvajal G, Cuello C, Ruiz M, Vázquez JM, Martínez EA and Roca J (2004) Effects of Centrifugation Before Freezing on Boar Sperm Cryosurvival. *Journal of Andrology* **25** 389–396.

Chang H and Suarez SS (2012) Unexpected flagellar movement patterns and epithelial binding behavior of mouse sperm in the oviduct. *Biology of Reproduction* **86** 1–8,140.

Chapman SC, Lawson A, Macarthur WC, Wiese RJ, Loechel RH, Burgos-Trinidad M, Wakefield JK, Ramabhadran R, Mauch TJ and Schoenwolf GC (2005) Ubiquitous GFP expression in transgenic chickens using a lentiviral vector. *Development (Cambridge, England)* **132** 935–940.

Chen B-C, Legant WR, Wang K, Shao L, Milkie DE, Davidson MW, Janetopoulos C, Wu XS, Hammer JA, Liu Z *et al.* (2014) Lattice light-sheet microscopy: Imaging molecules to embryos at high spatiotemporal resolution. *Science* **346** 1257998–1257998.

Chen S, Zhang L, Le Y, Waqas Y, Chen W, Zhang Q, Ullah S, Liu T, Hu L, Li Q *et al.* (2015) Sperm storage and spermatozoa interaction with epithelial cells in oviduct of Chinese soft-shelled turtle, Pelodiscus sinensis. *Ecology and Evolution* **5** 3023–3030.

Chiba A and Nakamura M (2001) Microscopic structure of the sperm storage tubules in the polygynandrous alpine accentor, Prunella collaris (Aves). *Acta Zoologica* **82** 299–306.

Cho C, O'Dell Bunch D, Faure J-E, Goulding EH, Eddy EM, Primakoff P and Myles DG (1998) Fertilization Defects in Sperm from Mice Lacking Fertilin β. *Science* **281**.

Chung JJ, Shim SH, Everley RA, Gygi SP, Zhuang X and Clapham DE (2014) Structurally distinct Ca2+ signaling domains of sperm flagella orchestrate tyrosine phosphorylation and motility. *Cell* **157** 808–822.

Civetta A (1999) Direct visualization of sperm competition and sperm storage in Drosophila. *Current Biology* **9** 841–844.

Cogliati S, Frezza C, Soriano ME, Varanita T, Quintana-Cabrera R, Corrado M, Cipolat S, Costa V, Casarin A, Gomes LC *et al.* (2013) Mitochondrial cristae shape determines respiratory chain supercomplexes assembly and respiratory efficiency. *Cell* **155** 160–171.

Conchello J-A and Lichtman JW (2005) Optical sectioning microscopy. *Nature Methods* **2** 920–931.

Conner J and Crews D (1980) Sperm transfer and storage in the lizard Anolis carolinensis. *J. Morphol.* **163** 331–348.

Córdoba-Aguilar A, Uhía E and Rivera AC (2003) Sperm competition in Odonata (Insecta): the evolution of female sperm storage and rivals' sperm displacement. *Journal of Zoology* **261** 381–398.

Crowe SA, Kleven O, Delmore KE, Laskemoen T, Nocera JJ, Lifjeld JT and Robertson RJ (2009) Paternity assurance through frequent copulations in a wild passerine with intense sperm competition. *Animal Behaviour* **77** 183–187.

Crozier RH and Fjerdingstad EJ (2001) Polyandry in social Hymenoptera - disunity in diversity? *Annales Zoologici Fennici* **38** 267–285.

Cummins J (2009) Sperm motility and energetics. In *Sperm Biology*, pp 185–206. Elsevier.

D'Errico J (2012) arclength.

DaCosta RS (2005) Autofluorescence characterisation of isolated whole crypts and primary cultured human epithelial cells from normal, hyperplastic, and adenomatous colonic mucosa. *Journal of Clinical Pathology* **58** 766–774.

Daly JM and Golding DW (1977) A description of the spermatheca of Spirorbis spirorbis (L.) (Polychaeta: Serpulidae) and evidence for a novel mode of sperm transmission. *Journal of the Marine Biological Association of the United Kingdom* **57** 219–227.

Darwin C (1871) *The Descent of Man and Selection in Relation to Sex*. London: John Murray.

Demongeot J, Glade N, Hansen O and Moreira A (2007) An open issue: The inner mitochondrial membrane (IMM) as a free boundary problem. *Biochimie* **89** 1049–1057.

Dixit R and Cyr R (2003) Cell damage and reactive oxygen species production induced by fluorescence microscopy: effect on mitosis and guidelines for non-invasive fluorescence microscopy. *The Plant Journal* **36** 280–290.

Van Drimmelen GC (1946) 'Spermnests' in the oviduct of the domestic hen. *J. South African Vet. Med. Assoc* **17** 42–52.

Druart X, Cognié J, Baril G, Clément F, Dacheux JL, Gatti JL, Cognie J, Baril G, Clement F, Dacheux JL *et al.* (2009) In vivo imaging of in situ motility of fresh and liquid stored ram spermatozoa in the ewe genital tract. *Reproduction* **138** 45–53.

Eberhard WG (1996) *Female Control: Sexual Selection by Cryptic Female Choice*. Princeton University Press.

Eberhard WG (2000) Criteria for Demonstrating Postcopulatory Female Choice. *Evolution* **54** 1047–1050.

Fahrbach FO and Rohrbach A (2010) A line scanned light-sheet microscope with phase shaped self-reconstructing beams. *Optics Express* **18** 24229–24244.

Fahrbach FO, Gurchenkov V, Alessandri K, Nassoy P and Rohrbach A (2013a) Light-sheet microscopy in thick media using scanned Bessel beams and two-photon fluorescence excitation. *Optics Express* **21** 13824–13839.

Fahrbach FO, Voigt FF, Schmid B, Helmchen F and Huisken J (2013b) Rapid 3D light-sheet microscopy with a tunable lens. *Optics Express* **21** 21010.

Fawcett DW, Anderson WA and Phillips DM (1971) Morphogenetic factors influencing the shape of the sperm head. *Developmental Biology* **26** 220–251.

Firman RC and Simmons LW (2010) Sperm midpiece length predicts sperm swimming velocity in house mice. *Biology Letters* **6** 513–516.

Firman RC and Simmons LW (2014) No Evidence of Conpopulation Sperm Precedence between Allopatric Populations of House Mice. *PLoS ONE* **9** e107472.

Firman RC, Gasparini C, Manier MK and Pizzari T (2017) Postmating Female Control: 20 Years of Cryptic Female Choice. *Trends in Ecology and Evolution* **32** 368–382.

Fitzpatrick JL and Baer B (2011) Polyandry reduces sperm length variation in social insects. *Evolution* **65** 3006–3012.

Fitzpatrick JL and Lüpold S (2014) Sexual selection and the evolution of sperm quality. *Molecular Human Reproduction* **20** 1180–1189.

Fitzpatrick JL, Montgomerie R, Desjardins JK, Stiver KA, Kolm N and Balshine S (2009) Female promiscuity promotes the evolution of faster sperm in cichlid fishes. *Proceedings of the National Academy of Sciences* **106** 1128–1132.

Forstmeier W, Segelbacher G, Mueller JC and Kempenaers B (2007) Genetic variation and differentiation in captive and wild zebra finches (Taeniopygia guttata). *Molecular Ecology* **16** 4039–4050.

Fox W (1956) Seminal receptacles of snakes. *The Anatomical Record* **124** 519–539.

Freedman SL, Akuffo VG and Bakst MR (2001) Evidence for the innervation of sperm storage tubules in the oviduct of the turkey (Meleagris gallopavo). *Reproduction* **121** 809–814.

Fritz AH and Turner F. R (2002) A light and electron microscopical study of the spermathecae and ventral receptacle of Anastrepha suspensa (Diptera: Tephritidae) and implications in female influence of sperm storage. *Arthropod Structure and Development* **30** 293–313.

Frolikova M, Sebkova N, Ded L and Dvorakova-Hortova K (2016) Characterization of CD46 and β1 integrin dynamics during sperm acrosome reaction. *Scientific Reports* **6** 33714.

Froman DP (2003) Deduction of a model for sperm storage in the oviduct of the domestic fowl (Gallus domesticus). *Biology of Reproduction* **69** 248–253.

Froman DP and Feltmann AJ (1998) Sperm mobility: a quantitative trait of the domestic fowl (Gallus domesticus). *Biology of Reproduction* **58** 379–384.

Froman DP, Feltmann AJ, Rhoads ML and Kirby JD (1999) Sperm mobility: A primary determinant of fertility in the domestic fowl (Gallus domesticus). *Biology of Reproduction* **61** 400–405.

Froman DP, Pizzari T, Feltmann AJ, Castillo-Juarez H and Birkhead TR (2002) Sperm mobility: mechanisms of fertilizing efficiency, genetic variation and phenotypic relationship with male status in the domestic fowl, Gallus gallus domesticus. *Proceedings. Biological Sciences* **269** 607–612.

Gaffield MA and Betz WJ (2007) Imaging synaptic vesicle exocytosis and endocytosis with FM dyes. *Nature Protocols* **1** 2916–2921.

Gage MJG (1998) Mammalian sperm morphometry. *Proceedings. Biological Sciences* **265** 97–103.

Gage MJG and Freckleton RP (2003) Relative testis size and sperm

morphometry across mammals: no evidence for an association between sperm competition and sperm length. *Proceedings. Biological Sciences* **270** 625–632.

Gage MJG, Macfarlane CP, Yeates S, Ward RG, Searle JB and Parker GA (2004) Spermatozoal Traits and Sperm Competition in Atlantic Salmon. *Current Biology* **14** 44–47.

Gao L (2015) Optimization of the excitation light sheet in selective plane illumination microscopy. *Biomedical Optics Express* **6** 881–890.

Gao L, Shao L, Higgins CDD, Poulton JSS, Peifer M, Davidson MWW, Wu X, Goldstein B and Betzig E (2012) Noninvasive imaging beyond the diffraction limit of 3D dynamics in thickly fluorescent specimens. *Cell* **151** 1370–1385.

Gao L, Shao L, Chen B-CC and Betzig E (2014a) 3D live fluorescence imaging of cellular dynamics using Bessel beam plane illumination microscopy. *Nat Protoc* **9** 1083–1101.

Gao L, Zhu L, Li C and Wang L V. (2014b) Nonlinear light-sheet fluorescence microscopy by photobleaching imprinting. *Journal of The Royal Society Interface* **11** 20130851–20130851.

Garner DL and Johnson LA (1995) Viability assessment of mammalian sperm using SYBR-14 and propidium iodide. *Biology of Reproduction* **53** 276–284.

Garner DL, Pinkel D, Johnson LA and Pace MM (1986) Assessment of spermatozoal function using dual fluorescent staining and flow cytometric analyses. *Biology of Reproduction* **34** 127–138.

Garner DL, Johnson LA, Yue ST, Roth BL and Haugland RP (1994) Dual DNA staining assessment of bovine sperm viability using SYBR-14 and propidium iodide. *Journal of Andrology* **15** 620–629.

Gilbert AB and Lake PE (1963) Terminal Innervation of the Uterus and Vagina of the Domestic Hen. *Reproduction* **5** 41–NP.

Gilbert AB, Reynolds ME and Lorenz FW (1968a) Distribution of spermatozoa in the oviduct and fertility in domestic birds. V. Histochemistry of the

uterovaginal sperm-host glands of the domestic hen. *Journal of Reproduction and Fertility* **16** 433–444.

Gilbert AB, Reynolds ME and Lorenz FW (1968b) Distribution of spermatozoa in the oviduct and fertility in domestic birds. 8. The effect of a foreign object in the uterus on secretions of the sperm-host glands and the survival of spermatozoa in the oviduct of the domestic hen. *Journal of Reproduction and Fertility* **17** 311–314.

Gilkerson RW, Selker JML and Capaldi RA (2003) The cristal membrane of mitochondria is the principal site of oxidative phosphorylation. *FEBS Letters* **546** 355–358.

Gist DH and Jones JM (1989) Sperm storage within the oviduct of turtles. *Journal of Morphology* **199** 379–384.

Giusti F and Selmi MG (1985) The seminal receptacle and sperm storage in Cochlostoma montanum (Issel) (Gastropoda: Prosobranchia). *Journal of Morphology* **184** 121–133.

Graham JK, Kunze E and Hammerstedt RH (1990) Analysis of sperm cell viability, acrosomal integrity, and mitochondrial function using flow cytometry. *Biology of Reproduction* **43** 55–64.

Greger K, Swoger J and Stelzer EHK (2007) Basic building units and properties of a fluorescence single plane illumination microscope. *Review of Scientific Instruments* **78** 23705.

Gromko MH, Gilbert DG and Richmond RC (1984) Sperm transfer and use in the multiple mating system of Drosophila. *Sperm Competition and the Evolution of Animal Mating Systems* 371–426.

Gustafsson MGL (2000) Surpassing the lateral resolution limit by a factor of two using structured illumination microscopy. *Journal of Microscopy* **198** 82–87.

Hackenbrock CR (1966) Ultrastructural Bases for Metabolically Linked Mechanical Activity in Mitochondria. *The Journal of Cell Biology* **30**.

Hanken J and Sherman PW (1981) Multiple paternity in Belding's ground squirrel litters. *Science* **212** 351–353.

Harrison RAP and Vickers SE (1990) Use of fluorescent probes to assess membrane integrity in mammalian spermatozoa. *Journal of Reproduction and Fertility* **88** 343–352.

Haywood S (1993) Sensory Control of Clutch Size in the Zebra Finch (Taeniopygia guttata). *The Auk* **110** 778–786.

Hecht E (2002) *Optics*. San Francisco: Addison-Wesley.

Hell SW and Wichmann J (1994) Breaking the diffraction resolution limit by stimulated emission: stimulated-emission-depletion fluorescence microscopy. *Optics Letters* **19** 780.

Hellriegel B and Bernasconi G (2000) Female-mediated differential sperm storage in a fly with complex spermathecae, Scatophaga stercoraria. *Animal Behaviour* **59** 311–317.

Hemmings N and Birkhead TR (2017) Differential sperm storage by female zebra finches Taeniopygia guttata. *Proceedings. Biological Sciences* **284** 20171032.

Hemmings N, Birkhead TR, Brillard JP, Froment P and Briere S (2015) Timing associated with oviductal sperm storage and release after artificial insemination in domestic hens. *Theriogenology* **83** 1174–1178.

Hemmings N, Bennison C and Birkhead TR (2016) Intra-ejaculate sperm selection in female zebra finches. *Biology Letters* **12** 4–7.

Heryanto B, Yoshimura Y, Tamura T and Okamoto T (1997) Involvement of Apoptosis and Lysosomal Hydrolase Activity in the Oviducal Regression During Induced Molting in Chickens : A Cytochemical Study for End Labeling of Fragmented DNA and Acid Phosphatase Treatment of Birds and Collection of Samples. *Poultry Science* **76** 67–72.

Hirokawa N, Keller TCS, Chasan R and Mooseker MS (1983) Mechanism of brush border contractility studied by the quick-freeze, deep-etch method. *Journal of Cell Biology* **96** 1325–1336.

Hiyama G, Matsuzaki M, Mizushima S, Dohra H, Ikegami K, Yoshimura T, Shiba K, Inaba K and Sasanami T (2014) Sperm activation by heat shock

protein 70 supports the migration of sperm released from sperm storage tubules in Japanese quail (Coturnix japonica). *Reproduction* **147** 167–178.

Höhn S, Honerkamp-Smith AR, Haas PA, Trong PK and Goldstein RE (2015) Dynamics of a Volvox Embryo Turning Itself Inside Out. *Physical Review Letters* **114** 178101.

Holm L and Ridderstråle Y (1998) Localization of carbonic anhydrase in the sperm-storing regions of the turkey and quail oviduct. *Histochemical Journal* **30** 481–488.

Holm L and Wishart GJ (1998) The effect of pH on the motility of spermatozoa from chicken, turkey and quail. *Animal Reproduction Science* **54** 45–54.

Holm L, Ekwall H, Wishart GJ, Ridderstråle Y and Ridderstrale Y (2000a) Localization of calcium and zinc in the sperm storage tubules of chicken, quail and turkey using X-ray microanalysis. *Journal of Reproduction and Fertility* **118** 331–336.

Holm L, Ruziwa SD, Dantzer V and Ridderstråle Y (2000b) Carbonic anhydrase in the utero-vaginal junction of immature and mature ostriches. *British Poultry Science* **41** 244–249.

Holt W V and Fazeli A (2015) Do sperm possess a molecular passport? Mechanistic insights into sperm selection in the female reproductive tract. *Molecular Human Reproduction* **21** 491–501.

Hosken DJ and Stockley P (2004) Sexual selection and genital evolution. *Trends in Ecology & Evolution* **19** 87–93.

Hosken DJ, Garner TWJ and Ward PI (2001) Sexual conflict selects for male and female reproductive characters. *Current Biology* **11** 489–493.

Hothorn T, Bretz F and Westfall P (2008) Simultaneous Inference in General Parametric Models. *Biometrical Journal* **50** 346–363.

Howarth B (1971) Transport of Spermatozoa in the Reproductive Tract of Turkey Hens. *Poultry Science* **50** 84–89.

Hoyer P, Medeiros G de, Balázs B, Norlin N, Besir C, Hanne J, Kräusslich H-G, Engelhardt J, Sahl SJ, Hell SW *et al.* (2016) Breaking the diffraction limit of

light-sheet fluorescence microscopy by RESOLFT. *Proceedings of the National Academy of Sciences* **113** 3442–3446.

Huisken J, Swoger J, Del Bene F, Wittbrodt J and Stelzer EHK (2004) Optical Sectioning Deep Inside Live Embryos by Selective Plane Illumination Microscopy. *Science* **305** 1007–1009.

Huisken J, Swoger J, Lindek S and Stelzer EHK (2006) Selective plane illumination microscopy. In *Handbook of Biological Confocal Microscopy: Third Edition*, pp 672–679. Boston, MA: Springer US.

Humphreys PN (1972) Brief observations on the semen and spermatozoa of certain passerine and non-passerine birds. *J. Reprod. Fert.* **29** 327–336.

Humphries S, Evans JP and Simmons LW (2008) Sperm competition: linking form to function. *BMC Evolutionary Biology* **8** 319.

Ichikawa T, Nakazato K, Keller PJ, Kajiura-Kobayashi H, Stelzer EHK, Mochizuki A and Nonaka S (2013) Live Imaging of Whole Mouse Embryos during Gastrulation: Migration Analyses of Epiblast and Mesodermal Cells. *PLoS ONE* **8** e64506.

Ichikawa T, Nakazato K, Keller PJ, Kajiura-Kobayashi H, Stelzer EHK, Mochizuki A and Nonaka S (2014) Live imaging and quantitative analysis of gastrulation in mouse embryos using light-sheet microscopy and 3D tracking tools. *Nature Protocols* **9** 575–585.

Immler S and Birkhead TR (2005) A non-invasive method for obtaining spermatozoa from birds. *Ibis* **147** 827–830.

Immler S and Birkhead TR (2007) Sperm competition and sperm midpiece size: no consistent pattern in passerine birds. *Proceedings. Biological Sciences* **274** 561–568.

Immler S, Calhim S and Birkhead TR (2008) Increased postcopulatory sexual selection reduces the intramale variation in sperm design. *Evolution* **62** 1538–1543.

Ito T, Yoshizaki N, Tokumoto T, Ono H, Yoshimura T, Tsukada A, Kansaku N and Sasanami T (2011) Progesterone is a sperm-releasing factor from the

sperm-storage tubules in birds. *Endocrinology* **152** 3952–3962.

Jamieson BGM (2007) Avian spermatozoa: structure and phylogeny. In *Reproductive Biology and Phylogeny of Birds*, pp 349–511. Science Publishers.

Keller PJ (2013) In vivo imaging of zebrafish embryogenesis. *Methods* **62** 268–278.

Keller PJ and Stelzer EH (2008) Quantitative in vivo imaging of entire embryos with Digital Scanned Laser Light Sheet Fluorescence Microscopy. *Current Opinion in Neurobiology* **18** 624–632.

Keller TCS, Conzelman KA, Chasan R and Mooseker MS (1985) Role of myosin in terminal web contraction in isolated intestinal epithelial brush borders. *Journal of Cell Biology* **100** 1647–1655.

Keller PJ, Schmidt AD, Wittbrodt J and Stelzer EHK (2008a) Reconstruction of zebrafish early embryonic development by scanned light sheet microscopy. *Science* **322** 1065–1069.

Keller PJ, Pampaloni F, Lattanzi G and Stelzer EHK (2008b) Three-Dimensional Microtubule Behavior in Xenopus Egg Extracts Reveals Four Dynamic States and State-Dependent Elastic Properties. *Biophys J* **95** 1474–1486.

Kim K-W, Bennison C, Hemmings N, Brookes L, Hurley LL, Griffith SC, Burke T, Birkhead TR and Slate J (2017) A sex-linked supergene controls sperm morphology and swimming speed in a songbird. *Nature Ecology & Evolution* **1** 1168–1176.

King LM, Brillard JP, Garrett WM, Bakst MR and Donoghue AM (2002) Segregation of spermatozoa within sperm storage tubules of fowl and turkey hens. *Reproduction* **123** 79–86.

Kleven O, Fossøy F, Laskemoen T, Robertson RJ, Rudolfsen G and Lifjeld JT (2009) Comparative evidence for the evolution of sperm swimming speed by sperm competition and female sperm storage duration in passerine birds. *Evolution; International Journal of Organic Evolution* **63** 2466–2473.

Knief U, Forstmeier W, Pei Y, Ihle M, Wang D, Martin K, Opatová P, Albrechtová J, Wittig M, Franke A *et al.* (2017a) A sex-chromosome inversion causes strong overdominance for sperm traits that affect siring

success. *Nature Ecology & Evolution* **1** 1177–1184.

Knief U, Schielzeth H, Backström N, Hemmrich-Stanisak G, Wittig M, Franke A, Griffith SC, Ellegren H, Kempenaers B and Forstmeier W (2017b) Association mapping of morphological traits in wild and captive zebra finches: reliable within, but not between populations. *Molecular Ecology* **26** 1285–1305.

Köttgen M, Hofherr A, Li W, Chu K, Cook S, Montell C and Watnick T (2011) Drosophila sperm swim backwards in the female reproductive tract and are activated via TRPP2 ion channels. *PLoS ONE* **6** e20031.

Van Krey HP, Ogasawara FX and Pangborn J (1967) Light and Electron Microscopic Studies of Possible Sperm Gland Emptying Mechanisms. *Poultry Science* **46** 69–78.

Krisfalusi M, Miki K, Magyar PL and O'Brien DA (2006) Multiple glycolytic enzymes are tightly bound to the fibrous sheath of mouse spermatozoa. *Biology of Reproduction* **75** 270–278.

Kuznetsova A, Brockhoff PB and Christensen RHB (2016) lmerTest: Tests in Linear Mixed Effects Models.

Laissue PP, Alghamdi RA, Tomancak P, Reynaud EG and Shroff H (2017) Assessing phototoxicity in live fluorescence imaging. *Nature Methods* **14** 657–661.

Lakowicz JR (2006a) Introduction to Fluorescence. In *Principles of Fluorescence Spectroscopy*, pp 1–26. Boston, MA: Springer US.

Lakowicz JR (2006b) Fluorophores. In *Principles of Fluorescence Spectroscopy*, pp 63–95. Boston, MA: Springer US.

Larson AM (2010) Multiphoton microscopy. *Nature Photonics* **5**.

Lee MA, Trucco GS, Bechtol KB, Wummer N, Kopf GS, Blasco L and Storey BT (1987) Capacitation and acrosome reactions in human spermatozoa monitored by a chlortetracycline fluorescence assay. *Fertil Steril* **48** 649–658.

Leeuwenhoek A van (1678) Observationes D. Antonii Lewenhoeck, de Natis è semine genitali Animalculis. *Philosophical Transactions* **12** 1040–1043.

Leeuwenhoek A van (1989) *Alle de Brieven van Antoni van Leeuwenhoek*. CRC.

Legland D, Arganda-Carreras I and Andrey P (2016) MorphoLibJ: integrated library and plugins for mathematical morphology with ImageJ. *Bioinformatics (Oxford, England)* **32** 3532–3534.

Lemon WC, Pulver SR, Hockendorf B, McDole K, Branson K, Freeman J and Keller PJ (2015) Whole-central nervous system functional imaging in larval Drosophila. *Nat Commun* **6**.

Liberti J, Baer B and Boomsma JJ (2016) Queen reproductive tract secretions enhance sperm motility in ants. *Biology Letters* **12** 1–5.

Life Technologies Corporation (2010) Nucleic Acid Detection and Analysis. In *The Molecular Probes Handbook*, pp 302–360. Life Technologies Corporation.

Lindquist S and Craig EA (1988) the Heat -Shock Proteins. *Annual Review of Genetics* **22** 631–677.

Loew LM and Simpson LL (1981) Charge-shift probes of membrane potential: a probable electrochromic mechanism for p-aminostyrylpyridinium probes on a hemispherical lipid bilayer. *Biophysical Journal* **34** 353–365.

Longair MH, Baker DA and Armstrong JD (2011) Simple neurite tracer: Open source software for reconstruction, visualization and analysis of neuronal processes. *Bioinformatics* **27** 2453–2454.

Longo G, Musmeci R, Privitera R and Sottile L (1998) Ultrastructural organization of seminal receptacle and sperm storage in Porcellio laevis Latreille (Crustacea: Isopoda Oniscidea). *Tissue and Cell* **30** 464–474.

Løvlie H, Gillingham MAF, Worley K, Pizzari T and Richardson DS (2013) Cryptic female choice favours sperm from major histocompatibility complex-dissimilar males. *Proceedings. Biological Sciences* **280** 20131296.

Lüpold S, Calhim S, Immler S and Birkhead TR (2009) Sperm morphology and sperm velocity in passerine birds. *Proceedings. Biological Sciences* **276** 1175–1181.

Lymbery RA, Kennington WJ and Evans JP (2016) Fluorescent sperm offer a method for tracking the real-time success of ejaculates when they compete

to fertilise eggs. *Scientific Reports* **6** 1–8.

Mahou P, Vermot J, Beaurepaire E and Supatto W (2014) Multicolor two-photon light-sheet microscopy. *Nature Methods* **11** 600–601.

Malo AF, Gomendio M, Garde J, Lang-Lenton B, Soler AJ and Roldan ERS (2006) Sperm design and sperm function. *Biology Letters* **2** 246–249.

Manier MK, Belote JM, Berben KS, Novikov D, Stuart WT and Pitnick S (2010) Resolving Mechanisms of Competitive Fertilization Success in Drosophila melanogaster. *Science* **328** 354–357.

Mannella CA, Lederer WJ and Jafri MS (2013) The connection between inner membrane topology and mitochondrial function. *Journal of Molecular and Cellular Cardiology* **62** 51–57.

Marie-Orleach L, Janicke T, Vizoso DB, Eichmann M and Schärer L (2014) Fluorescent sperm in a transparent worm: validation of a GFP marker to study sexual selection. *BMC Evolutionary Biology* **14** 148.

Marie-Orleach L, Janicke T, Vizoso DB, David P and Schärer L (2016) Quantifying episodes of sexual selection: Insights from a transparent worm with fluorescent sperm. *Evolution* **70** 314–328.

Martín-Coello J, Benavent-Corai J, R S Roldan E and Gomendio M (2009) Sperm Competition Promotes Asymmetries in Reproductive Barriers between Closely Related Species. *Evolution* **63** 613–623.

Matsuzaki M, Mizushima S, Hiyama G, Hirohashi N, Shiba K, Inaba K, Suzuki T, Dohra H, Ohnishi T, Sato Y *et al.* (2015) Lactic acid is a sperm motility inactivation factor in the sperm storage tubules. *Scientific Reports* **5** 17643.

Mattei AL, Riccio ML, Avila FW and Wolfner MF (2015) Integrated 3D view of postmating responses by the Drosophila melanogaster female reproductive tract, obtained by micro-computed tomography scanning. *Proceedings of the National Academy of Sciences* **112** 8475–8480.

McDaniel CD, Bramwell RK and Howarth B (1997) Development of a novel fluorescence technique for quantifying the total number of spermatozoa

stored in the uterovaginal junction of hens. *Journal of Reproduction and Fertility* **109** 173–179.

McGrew MJ, Sherman A, Ellard FM, Lillico SG, Gilhooley HJ, Kingsman AJ, Mitrophanous KA and Sang H (2004) Efficient production of germline transgenic chickens using lentiviral vectors. *EMBO Reports* **5** 728–733.

McKechnie TS (1975) Speckle reduction. In *Laser Speckle and Related Phenomena*, pp 123–170. Berlin, Heidelberg: Springer Berlin Heidelberg.

Mero KN and Ogasawara FX (1970) Dimensions of uterovaginal sperm-storage tubules of the chicken and their possible significance in sperm release. *Poultry Science* **49** 1304–1308.

Miller GT and Pitnick S (2002) Sperm-female coevolution in Drosophila. *Science* **298** 1230–1233.

Moritz RFA, Kryger P, Koeniger G, Koeniger N, Estoup A and Tingek S (1995) High degree of polyandry in Apis dorsata queens detected by DNA microsatellite variability. *Behavioral Ecology and Sociobiology* **37** 357–363.

Morrow EH and Gage MJ (2000) The evolution of sperm length in moths. *Proceedings. Biological Sciences* **267** 307–313.

Mossman J, Slate J, Humphries S and Birkhead T (2009) Sperm morphology and velocity are genetically codetermined in the zebra finch. *Evolution* **63** 2730–2737.

Nakahara M and Tsubaki Y (2007) Function of multiple sperm-storage organs in female damselflies (Ischnura senegalensis): Difference in amount of ejaculate stored, sperm loss, and priority in fertilization. *Journal of Insect Physiology* **53** 1046–1054.

Nevo AC and Rikmenspoel R (1970) Diffusion of ATP in sperm flagella. *Journal of Theoretical Biology* **26** 11–18.

Newport Corporation (2006) NanoPZTM Ultra High Resolution Motion System User's Manual.

Nielsen J, Gejl KD, Hey-Mogensen M, Holmberg H-C, Suetta C, Krustrup P, Elemans CPH and Ørtenblad N (2017) Plasticity in mitochondrial cristae

density allows metabolic capacity modulation in human skeletal muscle. *The Journal of Physiology* **595** 2839–2847.

Nosrati R, Driouchi A, Yip CM and Sinton D (2015) Two-dimensional slither swimming of sperm within a micrometre of a surface. *Nature Communications* **6** 8703.

Owaribe K, Kodama R and Eguchi G (1981) Demonstration of contractility of circumferential actin bundles and its morphogenetic significance in pigmented epithelium in vitro and in vivo. *Journal of Cell Biology* **90** 507–514.

Pal D (1977) Histochemistry of the utero-vaginal junction with special reference to the sperm-host glands in the oviduct of the domestic duck. *Folia Histochemica et Cytochemica* **15** 235–242.

Pampaloni F, Ansari N and Stelzer EK (2013) High-resolution deep imaging of live cellular spheroids with light-sheet-based fluorescence microscopy. *Cell and Tissue Research* **352** 161–177.

Parker GA (1970) Sperm competition and its evolutionary consequences in the insects. *Biological Reviews* **45** 525–567.

Parker GA (1984) Sperm competition and the evolution of animal mating systems. In *Sperm Competition and the Evolution of Animal Mating Systems*, pp 2–55. Academic Press.

Parker GA (1998) Sperm Competition and the Evolution of Ejaculates: Towards a Theory Base. In *Sperm Competition and Sexual Selection*, pp 3–54. Elsevier.

Pawley J (1995) Fundamental limits in confocal microscopy. *Handbook of Biological Confocal Microscopy* 19–37.

Pinto-Teixeira F, Muzzopappa M, Swoger J, Mineo A, Sharpe J and Lopez-Schier H (2013) Intravital imaging of hair-cell development and regeneration in the zebrafish. *Frontiers in Neuroanatomy* **7**.

Pitnick S and Brown WD (2000) Criteria for demonstrating female sperm choice. *Evolution; International Journal of Organic Evolution* **54** 1052–1056.

Pitnick S, Markow T and Spicer GS (1999) Evolution of Multiple Kinds of Female Sperm-Storage Organs in Drosophila. *Evolution* **53** 1804.

Pitnick S, Hosken DJ and Birkhead TR (2009a) Sperm morphological diversity. *Sperm Biology* **3** 69–149.

Pitnick S, Wolfner MF and Suarez SS (2009b) Ejaculate-female and sperm-female interactions. *Sperm Biology: An Evolutionary Perspective* 247–304.

Pitrone PG, Schindelin J, Stuyvenberg L, Preibisch S, Weber M, Eliceiri KW, Huisken J and Tomancak P (2013) OpenSPIM: an open-access light-sheet microscopy platform. *Nature Methods* **10** 598–599.

Pizzari T and Birkhead TR (2000) Female feral fowl eject sperm of subdominant males. *Nature* **405** 787–789.

Power RM and Huisken J (2017) A guide to light-sheet fluorescence microscopy for multiscale imaging. *Nature Methods* **14** 360–373.

Preibisch S, Saalfeld S, Schindelin J and Tomancak P (2010) Software for bead-based registration of selective plane illumination microscopy data. *Nature Methods* **7** 418–419.

Pyle JL, Kavalali ET, Choi S and Tsien RW (1999) Visualization of Synaptic Activity in Hippocampal Slices with FM1-43 Enabled by Fluorescence Quenching. *Neuron* **24** 803–808.

Racey PA (1979) Prolonged storage and survival of spermatozoa in chiroptera. *Journal of Reproduction and Fertility* **56** 391–402.

R Development Core Team (2015) R: A Language and Environment for Statistical Computing.

Ramm SA, Parker GA and Stockley P (2005) Sperm competition and the evolution of male reproductive anatomy in rodents. *Proceedings. Biological Sciences* **272** 949–955.

Renden JA, May EB and Benoff FH (1981) Histochemistry of uterovaginal sperm-host glands in Japanese Quail (Coturnix coturnix japonica) with reference to the period of oviposition. *Poultry Science* **60** 2529–2535.

Reynaud EG, Krzic U, Greger K and Stelzer EHK (2008) Light sheet-based fluorescence microscopy: more dimensions, more photons, and less photodamage. *HFSP Journal* **2** 266–275.

Ritter JG, Veith R, Siebrasse J-P and Kubitscheck U (2008) High-contrast single-particle tracking by selective focal plane illumination microscopy. *Optics Express* **16** 7142–7152.

Ritter JG, Veith R, Veenendaal A, Siebrasse JP and Kubitscheck U (2010) Light Sheet Microscopy for Single Molecule Tracking in Living Tissue. *Plos One* **5** e11639.

Robinson A, Fang JM, Chou PT, Liao KW, Chu RM and Lee SJ (2005) Probing lectin and sperm with carbohydrate-modified quantum dots. *ChemBioChem* **6** 1899–1905.

Rosengrave P, Gemmell NJ, Metcalf V, McBride K and Montgomerie R (2008) A mechanism for cryptic female choice in chinook salmon. *Behavioral Ecology* **19** 1179–1185.

Rosengrave P, Montgomerie R and Gemmell NJ (2016) Cryptic female choice enhances fertilization success and embryo survival in chinook salmon. *Proceedings. Biological Sciences* **283** 20160001.

Rowe M, Laskemoen T, Johnsen A and Lifjeld JT (2013) Evolution of sperm structure and energetics in passerine birds. *Proceedings. Biological Sciences* **280** 20122616.

Rowe M, Albrecht T, Cramer ERA, Johnsen A, Laskemoen T, Weir JT and Lifjeld JT (2015) Postcopulatory sexual selection is associated with accelerated evolution of sperm morphology. *Evolution* **69** 1044–1052.

Rust MJ, Bates M and Zhuang X (2006) Sub-diffraction-limit imaging by stochastic optical reconstruction microscopy (STORM). *Nature Methods* **3** 793–796.

Saeki Y, Tanabe Y, Katsuragi T and Miyagi M (1963) Studies on the advance and distribution of cock sperm in the oviduct, with special reference to the tracing method with 32P-labelled sperm. *Bull, of Natl. Institute of Animal Industry* **3** 91–97.

Saleh BEA and Teich MC (1991) Beam Optics. In *Fundamentals of Photonics*, pp 80–107. New York, USA: John Wiley & Sons, Inc.

Sanchez AM, Flamini MI, Polak K, Palla G, Spina S, Mannella P, Genazzani AD and Simoncini T (2012) Actin cytoskeleton remodelling by sex steroids in neurones. In *Journal of Neuroendocrinology*, pp 195–201. Blackwell Publishing Ltd.

Santi PA, Johnson SB, Hillenbrand M, GrandPre PZ, Glass TJ and Leger JR (2009) Thin-sheet laser imaging microscopy for optical sectioning of thick tissues. *BioTechniques* **46** 287–294.

Scherf N and Huisken J (2015) The smart and gentle microscope. *Nat Biotech* **33** 815–818.

Schindelin J, Arganda-Carreras I, Frise E, Kaynig V, Longair M, Pietzsch T, Preibisch S, Rueden C, Saalfeld S, Schmid B *et al.* (2012) Fiji: an open-source platform for biological-image analysis. *Nature Methods* **9** 676–682.

Schmid B, Shah G, Scherf N, Weber M, Thierbach K, Campos CP, Roeder I, Aanstad P and Huisken J (2013) High-speed panoramic light-sheet microscopy reveals global endodermal cell dynamics. *Nature Communications* **4** 2207.

Schuppin GT, Van Krey HP, Denbow DM, Bakst MR and Meyer GB (1984) Ultrastructural analyses of uterovaginal sperm storage glands in fertile and infertile turkey breeder hens. *Poult Sci* **63** 1872–1882.

Scott BB and Lois C (2005) Generation of tissue-specific transgenic birds with lentiviral vectors. *Proceedings of the National Academy of Sciences* **102** 16443–16447.

Sebkova N, Ded L, Vesela K and Dvorakova-Hortova K (2014) Progress of sperm IZUMO1 relocation during spontaneous acrosome reaction. *Reproduction* **147** 231–240.

Sena G, Frentz Z, Birnbaum KD and Leibler S (2011) Quantitation of cellular dynamics in growing Arabidopsis roots with light sheet microscopy. *PloS One* **6** e21303.

Sexton TJ (1974) Oxidative and glycolytic activity of chicken and turkey spermatozoa. *Comparative Biochemistry and Physiology Part B: Comparative Biochemistry* **48** 59–65.

Shen C, Kuang Y, Liu J, Feng J, Chen X, Wu W, Chi J, Tang L, Wang Y, Fei J *et al.* (2013) Prss37 is required for male fertility in the mouse. *Biology of Reproduction* **88** 123, 1–11.

Shugart GW (1988) Uterovaginal Sperm-Storage Glands in Sixteen Species with Comments on Morphological Differences. *The Auk* **105** 379–384.

Siedentopf H and Zsigmondy R (1903) Über Sichtbarmachung und Groessenbestimmung ultramikroskopischer Teilchen, mit besonderer Anwendung auf Goldrubinglaesern. *Annalen Der Physik* **10** 1–39.

Siegman AE (1986) *Lasers*. University Science Books, Sausalito, CA.

Simmons LW (2001) *Sperm Competition and Its Evolutionary Consequences in the Insects*. Princeton University Press.

Siva-Jothy MT (1987) The structure and function of the female sperm-storage organs in libellulid dragonflins. *Journal of Insect Physiology* **33** 559–567.

Smith RW (1983) Holographic methods in microscopy. *Journal of Microscopy* **129** 29–47.

Snook RR (2005) Sperm in competition: not playing by the numbers. *Trends in Ecology & Evolution* **20** 46–53.

Spence MTZ and Johnson ID (2010a) Tracers for Membrane Labeling—Section 14.4. In *The Molecular Probes Handbook. A Guide to Fluorescent Probes and Labeling Technologies*, pp 618–629. Life Technologies Corporation.

Spence MTZ and Johnson ID (2010b) Probes for Lipids and Membranes—Section 13.4. In *The Molecular Probes Handbook. A Guide to Fluorescent Probes and Labeling Technologies*, pp 547–587. Life Technologies Corporation.

Steele MGG and Wishart GJJ (1996) The effect of removing surface-associated proteins from viable chicken spermatozoa on sperm function in vivo and in vitro. *Animal Reproduction Science* **45** 139–147.

Stockley P, Gage MJ, Parker GA and Møller AP (1997) Sperm competition in fishes: the evolution of testis size and ejaculate characteristics. *The American Naturalist* **149** 933–954.

Storey BT and Kayne FJ (1975) Energy Metabolism of Spermatozoa. V. The Embden-Myerhof Pathway of Glycolysis: Activities of Pathway Enzymes in Hypotonically Treated Rabbit Epididymal Spermatozoa*†*Supported by United States Public Health Service Grant HD-06274 and National Science Foun. *Fertility and Sterility* **26** 1257–1265.

Supatto W, Truong T V, Débarre D and Beaurepaire E (2011) Advances in multiphoton microscopy for imaging embryos. *Current Opinion in Genetics & Development* **21** 538–548.

Sutovsky P, Navara CS and Schatten G (1996) Fate of the sperm mitochondria, and the incorporation, conversion, and disassembly of the sperm tail structures during bovine fertilization. *Biol Reprod* **55** 1195–1205.

Takei GL, Miyashiro D, Mukai C and Okuno M (2014) Glycolysis plays an important role in energy transfer from the base to the distal end of the flagellum in mouse sperm. *Journal of Experimental Biology* **217** 1876–1886.

Tegelström H, Searle J, Brookfield J and Mercer S (1991) Multiple paternity in wild common shrews (Sorex araneus) is confirmed by DNA-fingerprinting. *Heredity* **66 (Pt 3)** 373–379.

Teng P (2011) Extract Slice from Volume.

Thompson JE (2012) Mixing for the truth: using heterospermic inseminations to examine sperm selection and the specificity of 'fertilising' sperm in the Zebra Finch Taeniopygia guttata. University of Sheffield.

Thompson MJ and Jiggins CD (2014) Supergenes and their role in evolution. *Heredity* **113** 1–8.

Thompson CM and Shure L (1995) Image processing toolbox [for use with Matlab].

Thornhill R (1983) Cryptic Female Choice and Its Implications in the Scorpionfly Harpobittacus nigriceps. *The American Naturalist* **122** 765–788.

Tourmente M, Gomendio M and Roldan ERS (2011) Sperm competition and the evolution of sperm design in mammals. *BMC Evolutionary Biology* **11** 12.

Tourmente M, Rowe M, González-Barroso MM, Rial E, Gomendio M and

Roldan ERS (2013) Postcopulatory sexual selection increases ATP content in rodent spermatozoa. *Evolution; International Journal of Organic Evolution* **67** 1838–1846.

Tourmente M, Villar-Moya P, Rial E and Roldan ERS (2015) Differences in ATP generation via glycolysis and oxidative phosphorylation and relationships with sperm motility in mouse species. *Journal of Biological Chemistry* **290** 20613–20626.

Uller T and Olsson M (2008) Multiple paternity in reptiles: Patterns and processes. *Molecular Ecology* **17** 2566–2580.

Urbach D, Folstad I and Rudolfsen G (2005) Effects of ovarian fluid on sperm velocity in Arctic charr (Salvelinus alpinus). *Behavioral Ecology and Sociobiology* **57** 438–444.

Varea-Sánchez M, Gómez Montoto L, Tourmente M, Roldan ERS and Arnqvist G (2014) Postcopulatory sexual selection results in spermatozoa with more uniform head and flagellum sizes in rodents. *PLoS ONE* **9** e108148.

Venables WN and Ripley BD (2002) *Modern Applied Statistics With S*. Springer, New York.

Vernon GG and Woolley DM (1999) Three-dimensional motion of avian spermatozoa. *Cell Motility and the Cytoskeleton* **42** 149–161.

Vettenburg T, Dalgarno HIC, Nylk J, Coll-Llado C, Ferrier DEK, Cizmar T, Gunn-Moore FJ and Dholakia K (2014) Light-sheet microscopy using an Airy beam. *Nat Meth* **11** 541–544.

Waage JK (1979) Dual function of the damselfly penis: sperm removal and transfer. *Science* **203** 916 LP-918.

Waggoner AS (1979) Dye indicators of membrane potential. *Annu. Rev. Biophys. Bioeng.* **8** 47–68.

Ward PI (1993) Females influence sperm storage and use in the yellow dung fly Scathophaga stercoraria (L.). *Behavioral Ecology and Sociobiology* **32**.

Washington NL and Ward S (2006) FER-1 regulates Ca2+ -mediated membrane fusion during C. elegans spermatogenesis. *Journal of Cell Science* **119** 2552–

2562.

Westhoff D and Kamp G (1997) Glyceraldehyde 3-phosphate dehydrogenase is bound to the fibrous sheath of mammalian spermatozoa. *Journal of Cell Science* **110 (Pt 1** 1821–1829.

Williams DB and Carter CB (1996) The Transmission Electron Microscope. In *Transmission Electron Microscopy*, pp 3–17. Boston, MA: Springer US.

Wishart GJ (1986) Predicting the reproductive potential of poultry. In *Proceedings 7th European Poultry Conference, Paris, World's Poultry Science Association*, pp 946–949.

Wlodkowic D, Skommer J and Darzynkiewicz Z (2008) SYTO probes in the cytometry of tumor cell death. *Cytometry Part A* **73** 496–507.

Wlodkowic D, Skommer J, Faley S, Darzynkiewicz Z and Cooper JM (2009) Dynamic analysis of apoptosis using cyanine SYTO probes: From classical to microfluidic cytometry. *Experimental Cell Research* **315** 1706–1714.

Wu Y, Wawrzusin P, Senseney J, Fischer RS, Christensen R, Santella A, York AG, Winter PW, Waterman CM, Bao Z *et al.* (2013) Spatially isotropic four-dimensional imaging with dual-view plane illumination microscopy. *Nature Biotechnology* **31** 1032–1038.

Xu J and Wang Q (2010) Mechanisms of last male precedence in a moth: Sperm displacement at ejaculation and storage sites. *Behavioral Ecology* **21** 714–721.

Yoshimura Y, Koike K and Okamoto T (2000) Immunolocalization of progesterone and estrogen receptors in the sperm storage tubules of laying and diethylstilbestrol-injected immature hens. *Poultry Science* **79** 94–98.

Zavaleta D and Ogasawara F (1973) A review of the mechanism of the release of spermatozoa from storage tubules in the fowl and turkey oviduct. *World's Poultry Science Journal* **43** 132–139.

Ziegler A, Kentenich H and Uchanska-Ziegler B (2005) Female choice and the MHC. *Trends in Immunology* **26** 496–502.

Zuylen J (1981) The microscopes of Antoni van Leeuwenhoek. *Journal of Microscopy* **121** 309–328.

Appendix

Chapter 2

'PSF.m'

MATLAB script for calculating point spread function (PSF) from experimental data

```
% ---- o ----
% PSF of SPIM system
% Tania Mendonca
% ---- o ----
% first load experimental data, then..
group = Lateral(:,1);  %define parts of the matrix
x = Lateral(:,2);
y = Lateral(:,3);
f = fit(x,y,'gauss1');    %best fit gaussian
gaussy = f(x);            %values from best fit guassian

%plot
scatter(lateral(:,2),lateral(:,3),'k.','DisplayName','Experimental Data');
legend show;
hold on
plot(f,'r--');

%fwhm [Rev 1.2, April 2006 (Patrick Egan)]
latpsf = fwhm(x,gaussy);
```

Chapter 4

'Volume.m'

MATLAB script for extracting volume from multi-view deconvolved images of zebra finch sperm

```
% ---- o ----
% "Morphometry"
% Tania Mendonca 2016
% ---- o ----

%Import data
Folder = uigetdir('Directory');                    %prompt to select folder

[upperPath, deepestFolder,ext] = fileparts(Folder);
BirdID = horzcat(deepestFolder,ext);        %get BirdID from folder name

%define generic file pattern
fileName = horzcat(BirdID,'_*-*_Deconv','.tif');
filePattern = fullfile(Folder,fileName);
dataFiles = dir(filePattern);


for k = 1:length(dataFiles)
   baseFileName = dataFiles(k).name;                %returns current
filename
   filedr = fullfile(Folder, baseFileName);
   temp=imfinfo(filedr);
   nimages=size(temp,1);

for I=1:nimages
   data(:,:,I)=imresize(double(imread(filedr,I)),1);   %import image into
matrix
```

```
end

%Max intensity projection
mip=max(data,[],3);
n=min(data(:));
m=quantile(data(:),0.99997);
clims=[n,m];                                %better scaling of intensities
imagesc(mip,clims);


% Define Mid-piece ROI
midp=roipoly;

% Set threshold
thresh=median(mip(midp))+2*iqr(mip(midp));

% Convert ROI into 3D volume
midp3D=repmat(midp,1,1,nimages);
mask=data.*midp3D;
sperm=logical(mask>thresh);
isosurface(sperm,0)

% Display thresholded mid-piece
midmip=mip.*midp;
sperm1=logical(midmip>thresh);
imagesc(sperm1);
hold on
b=imagesc(mip,clims);
alpha(b,0.5)

% Compute volume
stats=regionprops('table',sperm,'all');
pxl2micron= 0.234;
mpvolume=stats.Area*(pxl2micron)^3;
```

```
% Write to table
[pathstr,name,ext] = fileparts(fileName);
file=cellstr(name);
if exist('T','var');
  Tnew=table(file,mpvolume,d);
  T = [T;Tnew];
else
     T=table(file,mpvolume,d);
end


end

%write to excel sheet
xlname=strcat(name,'.xlsx');
T2=table2cell(T);
T3=vertcat(T.Properties.VariableNames,T2);
xlwrite(xlname,T3);
```

'TEM.m'

MATLAB script for extracting mitochondrial packing information

```
% ---- o ----
% "Morphometry TEM image analysis"
% Tania Mendonca 2016
% ---- o ----

% Import image data
data=double(imread('Filename'));
imagesc(data);

% Define mitochondria ROI
mitoROI = roipoly;
mask = data.*mitoROI;

% Threshold to isolate cristae
thresh=quantile(data(:),0.17); %45
m = (mask > 0) & (mask < thresh);
mask2 = mask.*m;

% Isolate whole mitochondria
m2 = imfill(m,'holes');
imagesc(m2);
mask2 = mask.*~m2;

% Plot
figure
subplot(1,3,1)
imagesc(data)
subplot(1,3,2)
imagesc(mask2)
```

```
% Compute area
stats1=regionprops('table',m,'all');          % occupied by cristae
pxl2nm= 1.652;                    % pixel to nm conversion (from image scale)
vol1=stats1.Area*(pxl2nm)^2;
matrix = sum(vol1);

stats2=regionprops('table',m2,'all');         % occupied by mitochondria
vol2=stats2.Area*(pxl2nm)^2;
mito = sum(vol2);


% Write to table
T=table(mito,matrix);
```

Chapter 5

'Dilate.ijm'
Fiji macro for pre-processing SST image stacks

```
// 05.08.2016 – by: Tania Mendonca – 'Image resize and save as .tiff'

input = "InputFileDirectory";
output = "OutputFileDirectory";

function imagesize(input, output, filename) {
	var filetoget = input + filename;
	run("Bio-Formats Importer", "open = filetoget");
	getDimensions(width, height, channels, slices, frames);
	Stack.setDimensions(1, frames, slices);
	run("Properties...", "unit=micron pixel_width = 0.234 pixel_height
= 0.234 voxel_depth = 0.75 frame = [0.75 sec] global");
	run("Subtract Background...", "rolling=100 stack");
	run("8-bit");
	saveAs("Tiff", output + filename);

	dotIndex = indexOf(filename, ".tif");
	title = substring(filename, 0, dotIndex);
	run("Morphological Filters (3D)", "operation=Dilation element =
Cube x-radius = 2 y-radius = 2 z-radius = 2");
	selectWindow(title + "-Dilation");
	run("Gaussian Blur...", "sigma = 10 stack");
```

```
        saveAs("Tiff", output + title+ "-Dilation.tif");
        close();
        selectWindow(filename);
        close();
        }

list = getFileList(input);
for (i = 0; i < list.length; i++)
        imagesize(input, output, list[i]);
```

‘ SST_shape.m’

MATLAB scripts for extracting SST shape information

4 scripts (0) Average traces, (1) Main Script, (2) Slice and (3) Measure

```
%  ~~~~~~~~~~  ~~~~~~~~~~
% "SST shape script"
% Tania Mendonca 2017
% ----------------------
%  (0) Average traces
% ----------------------

global p pt pscaled

% Import SST trace 1 data
[file1, path1] = uigetfile('*.csv','select file');
filedr = [path1, file1];

if(isempty(filedr))
   return
end

p1 = csvread(filedr);

% Interpolate the trace spline
lp1 = length(p1);
t1 = linspace(1,lp1,100);                    % 100 pt vector of spline
indices
t11 = (1:lp1);                               % spline indices
x1 = interp1(t11,p1(:,1),t1,'spline');       % interpolate each axes
separately using the interpolated spline indices
y1 = interp1(t11,p1(:,2),t1,'spline');
z1 = interp1(t11,p1(:,3),t1,'spline');
```

```
%-------

% Import SST trace 2 data
[file2,path2] = uigetfile('*.csv','select file');
filedr2 = [path2,file2];

if(isempty(file2))
   return
end

p2 = csvread(filedr2);

% Interpolate the trace spline
lp2 = length(p2);
t2 = linspace(1,lp2,100);
t22 = (1:lp2);
x2 = interp1(t22,p2(:,1),t2,'spline');
y2 = interp1(t22,p2(:,2),t2,'spline');
z2 = interp1(t22,p2(:,3),t2,'spline');

% Average spline trace through lumen
t3 = (1:2);
pscaled = zeros(100,3);
for K = 1:length(pscaled)
x4 = [x1(K), x2(K)];
y4 = [y1(K), y2(K)];
z4 = [z1(K), z2(K)];
mx = interp1(t3,x4,1.5,'spline');
my = interp1(t3,y4,1.5,'spline');
mz = interp1(t3,z4,1.5,'spline');
pscaled(K,:) = [mx, my, mz];
end
```

```
% Scale to match image data
p = [pscaled(:,1)/0.234,pscaled(:,2)/0.234,pscaled(:,3)/0.75];

% Display

figure;
plot3(x1,y1,z1,'b');
hold on
plot3(x2,y2,z2,'b');
hold on
plot3(pscaled(:,1),pscaled(:,2),pscaled(:,3),'r','LineWidth',2);

% Interpolate average trace spline
t = linspace(1,100,10);
t0 = (1:100);
x = interp1(t0,p(:,1),t,'spline');
y = interp1(t0,p(:,2),t,'spline');
z = interp1(t0,p(:,3),t,'spline');

x = x(:);
y = y(:);
z = z(:);

pt = [x,y,z];

% clearvars -except p pt;
```

```
%  ~~~~~~~~~~  ~~~~~~~~~~
% "SST shape script"
% Tania Mendonca 2017
% ----------------------
%  (1) Main script
% ----------------------

global data p pt pscaled

%% Import SST image data
[file2,path2] = uigetfile('*.tif','select file');
filedr2 = [path2,file2];

if(isempty(file2))
   return
end

% get number of images in the .tif stack
info = imfinfo([path2 file2]);
nimages = numel(info);

 for I = 1:nimages
 data(:,:,I) = imresize(double(imread(filedr2,I)),1);          % import
image into matrix
 end

%% Call slice script
SST_spline_slice
```

```
%  ~~~~~~~~~~  ~~~~~~~~~~
% "SST shape script"
% Tania Mendonca 2017
% ----------------------
%  (2) Slice
% ----------------------

global data p pt pscaled

 % Find nearest point to p(path) on pt(interpolated points)
idx = dsearchn(p,pt);
c = length(idx);

 % For every interpolated point, find neighbours on spline
for kk = 1:c
   a = idx(kk);
   p1 = p(a,:);

    if kk < 2;
        p0 = p(a,:);
        p2 = p(a+5,:);
    elseif kk > c-2;
        p0 = p(a-5,:);
        p2 = p(a,:);
    else
        p0 = p(a-5,:);
        p2 = p(a+5,:);
    end

  % Create a vector that originates from p0 and extends to p2
  n1 = p2-p1;

% extractSlice [Ver 1.5, 2011 (Teng P)]
```

```
 [slice1, sliceInd1,subX1, subY1, subZ1] =
extractSlice(data,p1(1),p1(2),p1(3),n1(1),n1(2),n1(3),500);

% here radius is set to match z dimension to avoid sampling outside the
matrix dimensions

 % distance of slice from opening
 pcurve = pscaled(1:a,:);              % Spline segment from opening to
slice

% arclength [Ver 1.0, 2012 (John D'Errico)]
 if kk == 1;
    l = 0;                          % distance at opening set to zero
 else
    l = arclength(pcurve(:,1),pcurve(:,2),pcurve(:,3));
 end

 % Write slice to file
 s = num2str(kk);
 filename = horzcat(s,'.mat');
 save(filename, 'kk', 'slice1', 'sliceInd1', 'subX1', 'subY1', 'subZ1', 'l');

end
```

```
%  ~~~~~~~~~~  ~~~~~~~~~~
% "SST shape script"
% Tania Mendonca 2017
% ----------------------
%  (3) Measure
% ----------------------

%Import data
Folder = uigetdir('Directory'); %prompt to select folder

[upperPath, deepestFolder,ext] = fileparts(Folder);

fileName = horzcat('*','.mat');                    %define generic file pattern
filePattern = fullfile(Folder,fileName);
dataFiles = dir(filePattern);

for k = 1:length(dataFiles)
   baseFileName = dataFiles(k).name;          %returns current filename
   filedr = fullfile(Folder, baseFileName);

   load(filedr);

   imagesc(slice);

% Rescale to match instrument pxl ratio [0.234 0.234 0.75]
X = subX * 0.234;
Y = subY * 0.234;
Z = subZ * 0.750;

slize = size(slice);

% select points along lumen
h = imgcf;
[x,y] = getpts(h);                    % select four points (double click on 4th)
```

```
i = sub2ind(slize,round(x),round(y));    % index of points

% coordinates of points from 3d image matrix
a1 = [X(i), Y(i), Z(i)];

% horizontal diameter
d1 = sqrt((a1(1)-a1(2))^2 + (a1(1,2)-a1(2,2))^2 + (a1(1,3)-
a1(2,3))^2);                                    % euclidian distance

% vertical diameter
d2 = sqrt((a1(3)-a1(4))^2 + (a1(3,2)-a1(4,2))^2 + (a1(3,3)-a1(4,3))^2);

% write to excel
if exist('T','var');
  Tnew=table(kk,d1,d2,l);
  T = [T;Tnew];
else
     T=table(kk,d1,d2,l);
end

end


xlname=strcat('measurements','.xlsx');
T2=table2cell(T);
T3=vertcat(T.Properties.VariableNames,T2);
xlwrite(xlname,T3);
```